ALMA MATER STUDIORUM
UNIVERSITÀ DI BOLOGNA

DOTTORATO DI RICERCA IN

INGEGNERIA ELETTRONICA, TELECOMUNICAZIONI E TECNOLOGIE DELL'INFORMAZIONE

Ciclo 37

Settore Concorsuale: 09/F2 - TELECOMUNICAZIONI

Settore Scientifico Disciplinare: ING-INF/03 - TELECOMUNICAZIONI

PERVASIVE 6G SYSTEMS: TOWARDS SUSTAINABLE JOINT SENSING AND COMMUNICATION SYSTEMS

Presentata da: Elisabetta Matricardi

Coordinatore Dottorato

Davide Dardari

Supervisore

Enrico Paolini

Co-Supervisore

Andrea Giorgetti

Esame finale anno 2025

Alma Mater Studiorum - Università di Bologna

DOTTORATO DI RICERCA IN
Ingegneria Elettronica, Telecomunicazioni e Tecnologie dell'Informazione

Ciclo 37

Settore Concorsuale: 09/F2 - Telecomunicazioni

Settore Scientifico Disciplinare: ING-INF/03 - Telecomunicazioni

PERVASIVE 6G SYSTEMS: TOWARDS SUSTAINABLE JOINT SENSING AND COMMUNICATION SYSTEMS

Presentata da:
ELISABETTA MATRICARDI

Supervisore:
Prof. Ing.
ENRICO PAOLINI

Coordinatore Dottorato:
Prof. Ing.
DAVIDE DARDARI

Co-supervisore:
Prof. Ing.
ANDREA GIORGETTI

Esame finale anno 2025

Borsa di dottorato del Programma Operativo Nazionale Ricerca e Innovazione 2014-2020 (CCI 2014IT16M2OP005), risorse FSE REACT-EU, Azione IV.4 "Dottorati e contratti di ricerca su tematiche dell'innovazione" e Azione IV.5 "Dottorati su tematiche Green." CUP J35F21003160006

Keywords

Signal Processing

Joint Sensing and Communication

Orthogonal Frequency-Division Multiplexing

5G & Beyond Systems

Multiple-Input Multiple-Output

Abstract

The integration of Joint Sensing and Communication (JSC) systems into next-generation mobile networks represents a transformative paradigm, facilitating advanced capabilities including cooperative target detection, precise localization, and resource-efficient sensing. This thesis explores the potential of JSC systems within the context of 5G networks, examining monostatic, bistatic, and multistatic configurations. By harnessing orthogonal frequency division multiplexing (OFDM)-based communication networks, this study addresses significant challenges and proposes innovative solutions to achieve high-accuracy sensing across diverse operational scenarios. The research provides key insights into the design and implementation of integrated sensing strategies, demonstrating how communication infrastructure can be repurposed to support robust and scalable environmental awareness.

In monostatic systems, a cooperative sensing framework was designed, incorporating range-angle radar maps fused across multiple base stations (BSs). This approach achieved good localization accuracy for various heterogeneous targets while maintaining high communication capacity, highlighting the dual functionality of JSC networks. The bistatic configuration demonstrated the adaptability of 5G NR waveforms for sensing applications, achieving robust localization performance despite limitations in direction of arrival (DoA) estimation and blind zones. Expanding to multistatic systems, the analysis introduced multiple-input single-output (MISO) and multiple-input multiple-output (MIMO) setups to further enhance sensing performance. A dual-mode operation—search and tracking—was developed to optimize spatial diversity, detection accuracy, and tracking precision. Techniques such as dynamic role rotation, beamforming, and selective data fusion were employed, achieving sub-meter localization accuracy and robust performance under high clutter

and noise conditions.

The thesis emphasizes the critical role of resource management, clustering algorithms, and reliability mapping in balancing sensing and communication performance. By addressing blind zones, clutter, and resource constraints, the study provides a comprehensive framework for integrating JSC capabilities into mobile networks. These findings establish a solid foundation for the development of future JSC technologies, contributing to applications such as autonomous systems, smart cities, and environmental monitoring.

Contents

Acronyms

AWGN additive white Gaussian noise

AoA angle of arrival

AoD angle of departure

AIC Akaike information criterion

BF beamformer

BS base station

CIR channel impulse response

CP cyclic prefix

DBSCAN density-based spatial clustering of applications with noise

DoA direction of arrival

DoD direction of departure

EIRP effective isotropic radiated power

ELP equivalent low-pass

FC fusion center

FD frequency-division

FAR false-alarm rate

FFT fast Fourier transform

FoV field-of-view

GOSPA generalized optimal subpattern assignment

ICI inter-carrier interference

IFFT inverse fast Fourier transform

ISI inter-symbol interference

i.i.d. independent, identically distributed

JSC joint sensing and communication

k-NN k-nearest neighbors

LOS line-of-sight

LS least square

MIMO multiple-input multiple-output

MISO multiple-input single-output

MUSIC multiple signal classification

mmWave millimeter-wave

NR new radio

OFDM orthogonal frequency division multiplexing

p.d.f. probability density function

PSK phase shift keying

PSD power spectral density

QPSK quadrature phase shift keying

QuaDRiGa QUAsi Deterministic RadIo channel GenerAtor

QAM quadrature amplitude modulation

RCS radar cross-section

RF radio frequency

RMSE root mean square error

Rx receiver

RoI region of interest

RRH remote radio head

r.v. random variable

SCM sample covariance matrix

SI self interference

SNR signal-to-noise ratio

TD time-division

TDoA time difference of arrival

ToA time of arrival

Tx transmitter

THz terahertz

UE user equipment

ULA uniform linear array

V2V vehicle-to-vehicle

V2X vehicle-to-everything

Chapter 1

Introduction

The increasing emphasis on safety in urban environments has positioned advanced sensing technologies as a critical area of research and development. This trend is driven by the potential of sensing to enable a diverse range of applications, such as enhanced traffic monitoring, autonomous driving, and environmental mapping [1, 2]. Of particular importance is the role of radio frequency (RF) signals in enhancing these applications, providing opportunities for improved performance and expanded capabilities. Furthermore, emerging technologies such as millimeter-wave (mmWave), terahertz (THz), and massive multiple-input multiple-output (MIMO) further enhance the feasibility of high-resolution sensing within cellular infrastructures [3–5]. Originally designed for high data rates and reduced latency, these technologies have been proved to provide high-accuracy sensing capabilities, such as precise range estimation and direction of arrival (DoA) detection [6,7]. These developments align closely with the vision of next-generation mobile networks, which aim to integrate novel capabilities and services, enabling seamless integration of sensing and communication, paving the way for robust frameworks that support a broad spectrum of applications [8, 9]. By leveraging shared infrastructure, joint sensing and communication (JSC) systems promise substantial gains in spectral efficiency, energy consumption, and hardware complexity, while reducing deployment costs [10, 11]. Additionally, cooperative sensing among base stations (BSs) facilitates monostatic, bistatic, and multistatic configurations, tailored to diverse scenarios. This has led to extensive

research in cellular JSC, addressing challenges in information theory, signal processing, waveform design, and resource management [12–14]. Although JSC offers undeniable advantages, designing such a system is inherently challenging due to the competing nature of the two functionalities, which compete for the same spectral resources. A diverse range of strategies exists in the literature for integrating sensing and communication functionalities. These strategies encompass sensing and communication coexistence, spectrum sharing through temporal, spectral, and spatial multiplexing, as well as a unified framework [15–17]:

- Coexistence with spectral overlap: Both radar and communication systems use active transmitters (Txs) within the same frequency band. The primary challenge is to mitigate or eliminate mutual interference while ensuring satisfactory performance for both functions. Some studies focus on optimizing radar performance, while others address radar-induced interference mitigation in communication.

- Coexistence via cognition: Jointly optimizing transmission strategies, often referred to as codesign, can offer significant advantages through cognitive approaches to predict channel conditions and minimize spectral overlap. Careful design and optimization of both waveforms are necessary to ensure satisfactory performance in sensing and communication.

- Functional coexistence: Achieving functional coexistence with minimal interference can be accomplished through various means. Information can be seamlessly embedded within the radar signal, or communication signals can be leveraged for sensing. Additionally, passive radar systems, which utilize signals of opportunity already present in the environment, fall under this category. Alternatively, dual-waveform systems designed to perform both tasks are another solution. All of these approaches fall under the umbrella of JSC.

In this thesis, we will focus on utilizing existing communication systems to perform sensing tasks, a paradigm often referred to as the communication-centric approach.

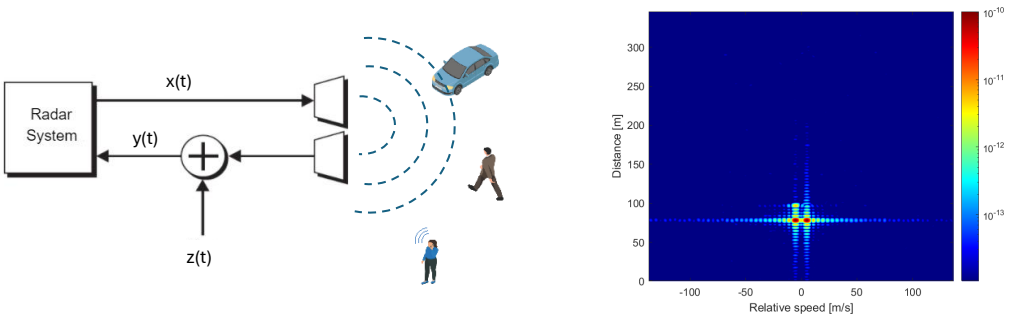

Figure 1.1: Schematic of a monostatic radar system.

1.1 Fundamentals of Radar Systems

We begin by examining a radar system that employs a single antenna for both transmitting and receiving signals. In this configuration, the system transmits a signal $x(t)$ into the environment. The received equivalent low-pass (ELP) signal $y(t)$ comprises echoes reflected from various objects, along with added noise from the receiver (Rx), as illustrated in Figure 1.1. By analyzing $y(t)$, the radar extracts information about the range and relative velocity of detected targets. The received signal, considering Q reflecting objects, is expressed as [18]:

$$y(t) = \sum_{q=0}^{Q-1} \alpha_q x(t - \tau_q) e^{j2\pi f_{\mathrm{D},q} t} e^{j\varphi_q} + z(t), \tag{1.1}$$

where α_q is the attenuation factor, dependent on the target's distance and radar cross-section (RCS), $\sigma_{\mathrm{RCS},q}$, φ_q is the phase offset, and $z(t)$ is additive white Gaussian noise (AWGN). Generally, in a basic monostatic radar system, the Tx and Rx are co-located, operating on the same device. In this case, the propagation delay is defined as the round-trip delay from the Tx to the target and back, and is calculated as $\tau_q = 2r_q/c$, where r_q is the distance of the qth target from the transceiver, while the Doppler frequency shift of the moving target due to radial velocity v_q is: $f_{\mathrm{D},q} = 2v_q f_\mathrm{c}/c$, where c is the speed of light, and f_c is the signal carrier frequency. In monostatic radars, the compact design simplifies deployment and analysis. However,

challenges arise due to self interference (SI), caused by the leakage of the transmitted signal into the receiver chain, and limited spatial diversity, as the co-located transmitter and receiver reduce the system's ability to capture diverse angular perspectives on the target. Bistatic radar systems address these limitations by separating Tx and Rx. This separation introduces geometric diversity, which can improve detection of stealth targets and mitigate interference. The received signal in a bistatic system accounts for the distances between the Tx and target, $r_{\mathrm{t},q}$, and between the target and Rx, $r_{\mathrm{r},q}$, defining the bistatic range $R_{\mathrm{bis},q} = r_{\mathrm{t},q} + r_{\mathrm{r},q}$. Consequently, the propagation delay is calculated as $\tau_q = R_{\mathrm{bis},q}/c$. While bistatic systems enhance coverage and detection capabilities, they require precise synchronization and complex calibration. Multistatic radar systems expand on bistatic principles by incorporating multiple Txs and Rxs that form bistatic pairs. This configuration significantly improves spatial diversity, enabling robust target detection and tracking in cluttered environments. Multistatic systems also provide resilience against single-point failures, making them well-suited for applications like air traffic control. However, these benefits come with increased system complexity and computational demands for data fusion and coordination.

The choice of radar configuration depends on application requirements such as coverage, target characteristics, and operational constraints. Monostatic systems are advantageous for simplicity, while bistatic and multistatic setups excel in addressing multipath effects and enhancing detection in diverse scenarios. These configurations represent trade-offs between complexity and performance, driving continued innovation in radar system design.

1.2 OFDM-based JSC systems

As discussed earlier, orthogonal frequency division multiplexing (OFDM)-based signals, widely used in systems like Wi-Fi, 4G, and 5G new radio (NR), are promising for JSC applications due to their inherent flexibility and extensive channel bandwidths [18–20]. In particular, 5G NR waveforms offer notable advantages, such as adaptable subcarrier spacing and resource allocation in time and frequency domains, which facilitate the seamless in-

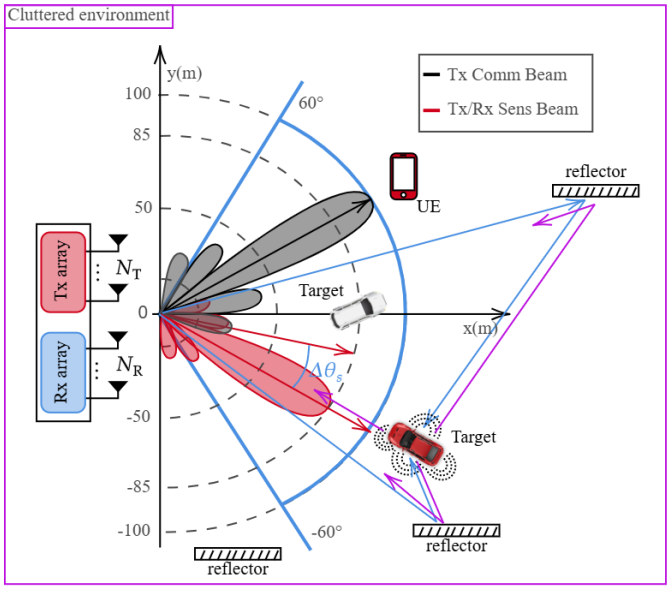

Figure 1.2: Illustration of the proposed JSC MIMO monostatic system with multi-beam capability. The system features a dedicated communication beam targeting a user equipment (UE) to ensure reliable data transmission, while a sensing beam actively scans the environment to detect non-cooperative objects. This dual-beam approach highlights the system's ability to seamlessly integrate communication and sensing functionalities.

tegration of sensing functionalities [20]. The inclusion of mmWave bands in 5G NR expands its potential, enabling channel bandwidths up to 400 MHz, which are well-suited for high-resolution sensing [21–23]. Wide bandwidths enhance range estimation accuracy, while shorter wavelengths support large antenna arrays, improving angular resolution and enabling DoA estimation through MIMO configurations. Furthermore, multibeam systems, as depicted in Fig. 1.2, allow simultaneous communication and sensing using distinct beams optimized for their respective tasks [22, 24].

In such systems, transmitted power is shared between communication and sensing, controlled by a parameter $\rho \in [0, 1]$ as shown in Eq. (1.2), where $\mathbf{w}_{\mathrm{T,s}}$ and $\mathbf{w}_{\mathrm{T,c}}$ denote the sensing and communication beamforming vectors, respectively [25, 26].

$$\mathbf{w}_{\mathrm{T}} = \sqrt{\rho}\,\mathbf{w}_{\mathrm{T,s}} + \sqrt{1-\rho}\,\mathbf{w}_{\mathrm{T,c}} \tag{1.2}$$

The integration of massive MIMO at mmWave frequencies has enabled significant advances in JSC systems, offering high data rates and precise localization capabilities [27]. Research efforts have addressed key challenges, including channel and target parameter estimation [28, 29], with a focus on improving scalability and managing extended targets. These innovations are expected to revolutionize applications like vehicular networks, where JSC can enhance beam tracking and target prediction for reliable communication and sensing [30, 31].
JSC systems can leverage various configurations for sensing and communication, including monostatic, bistatic, and multistatic setups. These configurations mirror those traditionally employed in radar systems, each offering distinct advantages depending on the application scenario. A visual representation of these configurations is shown in Fig. 1.3.

1.2.1 Cooperative Monostatic Networks

Extensive research has shown the feasibility of using OFDM-based waveforms for JSC systems, especially focusing on the monostatic configuration, i.e., with Tx and Rx co-located [9, 32]. For this type of configuration, a critical aspect is SI, as it requires the full-duplex capability for which technology is not yet at a mature stage [7, 20]. However, all these solutions introduce extra complexity to the BS and require very accurate hardware modeling. The sharp increase in the number of BSs opens the door to the development of precise and reliable localization systems, especially through cooperation of multiple monostatic sensors with the aid of a fusion center (FC). This, in turn, paves the way for enhanced safety measures in urban settings [33]. Additionally, the advent of massive MIMO technology at mmWave frequencies offers the opportunity not only to achieve remarkable data transmission rates but also to attain accurate object position estimation [27]. This noteworthy capability is anticipated to address emerging communication challenges effectively, embracing crucial aspects such as precise beam management [34], accurate estimation of target direction for beam tracking to maintain high-quality links [30], and the application of predictive beam tracking using JSC in vehicular scenarios [31]. In [28, 29], a unified channel and target parameter

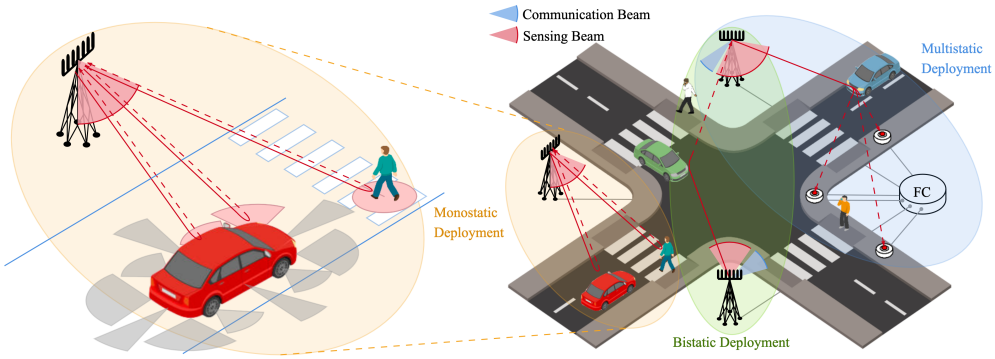

Figure 1.3: On the left, an extended vehicle target model with distributed scatterers and a pedestrian model with a point-like reflector, where reflections depend on the alignment of the visibility cone and the sensing beam. On the right, the three sensing configurations for JSC systems in urban environments: monostatic, bistatic, and multistatic. These configurations illustrate how separate beams can be used for communication and sensing, enabling dual functionality and adaptability to various deployment scenarios.

estimation method for MIMO-OFDM JSC systems is proposed, addressing a very important problem in the field. While the solution accurately estimates channel and point-like target parameters, it faces certain challenges as the number of targets increases and in managing extended targets.

1.2.2 Bistatic JSC Systems

A possible solution to avoid the SI problem is to resort to a bistatic configuration, where the Tx and Rx are not co-located. Bistatic radar setups are also interesting as they can extend the sensing area with a Rx that can be simple and mobile [35]. For this reason, bistatic JSC configuration is becoming of interest for future beyond 5G systems. For example, OFDM-based JSC in the bistatic arrangement has been proposed in vehicle-to-vehicle (V2V) scenarios, thanks to its potential ability to convey information between vehicles while sensing the presence of objects or cars nearby [36].

1.2.3 Multistatic JSC systems

In this configuration, sensing signals can be emitted and collected by multiple nodes, and both the BS and the UE may act as Txs and Rxs. Then,

the sensed information is collected by a FC for further processing, thereby yielding superior sensing performance than a monostatic configuration. Multistatic sensing may be divided into two groups based on the data sequence at the FC. In the first group, individual sensing is performed by each sensing node based on its own observations, such as signal strength, time of arrival (ToA), angle of arrival (AoA), or time difference of arrival (TDoA), with negligible impact on the network overhead [35, 37]. However, processing the acquired measurements (detection and estimation) at a single sensor level may lead to miss-detection events, especially for weak-target scenarios. In scenarios with multiple targets, this method also necessitates complex multi-target data association and localization [1, 38]. Furthermore, this approach requires at least three sensors to locate a target in 2D, so miss-detection events may occur even when a weak-target echo is picked up by only a fraction of the sensors belonging to the network. In contrast, in the second group, each sensor node processes the echo reflected from the target and sends such a signal (or a piece of soft information associated with it) to the FC, which then merges it with the information gathered by other nodes [39–41]. Here, data fusion offers a more comprehensive representation of the environment. Signal-level fusion is preferable in terms of performance since the approaches belonging to the first group may miss critical information due to in-sensor pre-processing at an early stage. However, it suffers from substantially higher processing and signaling overheads. More specifically, the multistatic radar configuration, supported by advanced wireless network architectures like Cloud-RAN, is particularly well-suited for JSC applications. It utilizes spatially distributed Txs and Rxs to enhance detection accuracy and coverage. The spatial diversity inherent in multistatic systems significantly improves the resolution and accuracy of target detection and parameter estimation, especially in cluttered urban environments [42]. In this configuration, both the BS and the UE can function as Txs and Rxs. Furthermore, the multistatic configuration circumvents the need for full-duplex technology, which is commonly required in monostatic radar systems [20].

1.3 Main Contributions

As we dive into the potential of 6G mobile radio networks and their applications, it is essential to examine the existing gaps in research. While significant strides have been made in integrating sensing and communication capabilities, certain aspects remain underexplored. In particular, the exploitation of mobile radio networks as an enabler for distributed and cooperative sensing is still under-investigated. Along these lines, the benefits of cooperation, as well as its impact on network overhead, have not been thoroughly addressed. Furthermore, the remarkable flexibility offered by mobile networks to allocate resources based on user needs has not been fully exploited for sensing, hindering adjustment of the sensing/communication trade-off to specific requirements [43–45]. The integration of cooperative sensing into the mobile network framework stands as an unexplored frontier, promising to enhance both the efficiency of sensing applications and the overall performance of the network. This thesis explores the feasibility of enabling sensing in MIMO-OFDM-based networks through the utilization of multi-sensor fusion techniques and resource management in Chapter 2. Specifically, we aim at exploiting range-angle radar maps derived from a collaborative set of BSs to detect and estimate heterogeneous targets in a surveillance area. The analysis then extends from a cooperative monostatic configuration to a bistatic JSC system in Chapter 3. Sensing performance is evaluated for a MIMO system, estimating both DoA and bistatic range for setups operating at sub-6 GHz and mmWave frequencies. In the second part of this thesis, a multistatic radar system is presented, with particular attention to the use of multiple-input single-output (MISO) and MIMO configurations. These systems are analyzed in terms of their performance in complex scenarios, where data from multiple base stations is fused to enhance detection capabilities. More specifically, Chapter 4 focuses on the fundamental aspects of the multistatic system, while Chapter 5 extends this analysis by examining the impact of different operation mode on system performance and robustness. In particular, a dual-mode operation—search and tracking—is introduced. In the search mode, range-angle maps from multiple BSs are fused for target detection, leveraging dynamic role rotation for enhanced spatial diversity and

accuracy. In the tracking mode, beam alignment optimizes power allocation and reduces clutter, refining localization and tracking precision.

1.4 Thesis Organization and Notation

The rest of the thesis is organized as follows.

Chapter 2: a set of monostatic MIMO-OFDM BSs based on 5G NR with multibeam capabilities is presented. In particular, at first we design the architecture of the cooperative sensing system, detailing the system components and the mathematical models used to describe the channel and targets. Specific attention is given to how these models enable accurate representation of the environment and target dynamics. Then, we introduce the data fusion strategy and clustering algorithm used for processing the collected measurements. The fusion approach is designed to enhance the accuracy of target state estimation, while the clustering algorithm ensures robust association of detections to individual targets. Next, we evaluate the performance of the proposed system through extensive simulations, analyzing metrics such as detection accuracy and estimation precision under various scenarios.

Chapter 3: we expand upon the performance analysis conducted previously, which focused on a cooperative monostatic configuration, to a bistatic JSC system. We first present the sensing performance of a bistatic JSC MIMO system consisting of a Tx and Rx, estimating both the DoA and bistatic range. More specifically, we compare two setups operating at sub-6 GHz and mmWave frequencies. Subsequently, we examine the root mean square error (RMSE) of position estimates within the monitored area through heatmaps, highlighting the impact of the blind zone on sensing. Finally, we investigate the sensing coverage limits of the bistatic system by varying the fraction of power allocated to sensing.

Chapter 4: we extend the analysis from Chapter 3 by exploring the performance of a multistatic MISO system based on 5G NR signals and its sensing capabilities. We investigate the impact of the fraction of power allocated to sensing and its effect on optimizing the sensing/communication trade-off. We also propose two data fusion approaches for position estimation, comparing a least square (LS) algorithm with a soft map generation technique.

Additionally, we analyze the RMSE of position estimates, emphasizing the advantages of a multistatic network over a bistatic configuration, particularly in addressing the issue of "blind zones".

Chapter 5: we further analyze a multistatic system based on OFDM signals, designed to operate in two distinct modes: search and tracking. In the search mode, thanks to the availability of multiple antennas at the Rx, the system scans the environment to detect new targets and provides a preliminary estimate of their positions, leveraging cooperation among BSs by fusing range-angle maps from each Rx in the multistatic network. Furthermore, we introduce selective data fusion to ensure that only reliable portions of the range-angle maps from each bistatic pair contribute to the cooperation process, leading to significant performance gains. The search capability is further improved through dynamic role rotation, allowing each BS to act as a Tx in succession, enabling multi-view perception of targets and enhancing spatial diversity, detection accuracy, and localization performance. In the tracking mode, we use the coarse target position estimates from the search phase to align the sensing beams of the transmitting BSs towards the detected targets. This alignment optimizes the transmit power and spatially filters clutter, further refining the tracking process. The performance of the proposed system is evaluated in both search and tracking modes, using the generalized optimal subpattern assignment (GOSPA) metric to assess the accuracy of position estimates in the presence of multiple targets.

The following notation is adopted: capital and lowercase boldface letters denote matrices and vectors, respectively; $\mathbf{I}_n$ is the $n \times n$ identity matrix; $\|\cdot\|_p$ stands for the p-norm; $\lfloor \cdot \rceil$ represents the round operator, while $\lfloor \cdot \rfloor$ and $\lceil \cdot \rceil$ are the flooring and ceiling functions, respectively; $\delta(\cdot)$ is the Dirac delta function; $(\cdot)^{\mathsf{c}}$ stands for the conjugate, $(\cdot)^{\dagger}$ is the Hermitian transpose, and $(\cdot)^{\mathsf{T}}$ represents the transpose operation. The notation $A \backslash B$ denotes the set A with the elements of B removed. $\mathbb{E}\{\cdot\}$ denotes statistical expectation. A zero-mean circularly symmetric complex Gaussian random vector with covariance $\boldsymbol{\Sigma}$ is denoted by $\mathbf{x} \sim \mathcal{CN}(\mathbf{0}, \boldsymbol{\Sigma})$, and $\mathbf{x} \sim \mathcal{N}(\boldsymbol{\mu}, \boldsymbol{\Sigma})$ denotes the real-valued Gaussian random vector with mean $\boldsymbol{\mu}$ and covariance $\boldsymbol{\Sigma}$. $[\mathbf{X}]_{a,b}$ represents the element at row a and column b of the matrix $\mathbf{X}$. The operator $|\cdot|$ denotes either the absolute value function or the cardinality of a set,

depending on the context. Finally, $\odot$ represents the element-wise product between two matrices.

Chapter 2

Monostatic Joint Sensing and Communication with OFDM

This chapter focuses on the description of the monostatic MIMO-OFDM JSC system based on 5G NR with multibeam capabilities for cooperative sensing. In particular, first, in Section 2.1, we present the architecture of the cooperative sensing system, detailing the system components and the mathematical models used to describe the channel and targets. Specific attention is given to how these models enable accurate representation of the environment and target dynamics. Then, in Section 2.2, we introduce the data fusion strategy and clustering algorithm used for processing the collected measurements. The fusion approach is designed to enhance the accuracy of target state estimation, while the clustering algorithm ensures robust association of detections to individual targets. Next, in Section 2.3, we evaluate the performance of the proposed system through extensive simulations, analyzing metrics such as detection accuracy, false alarm rate, and estimation precision under various scenarios. Finally, in Section 2.4, we summarize the key findings of this work and provide concluding remarks, outlining potential directions for future research.

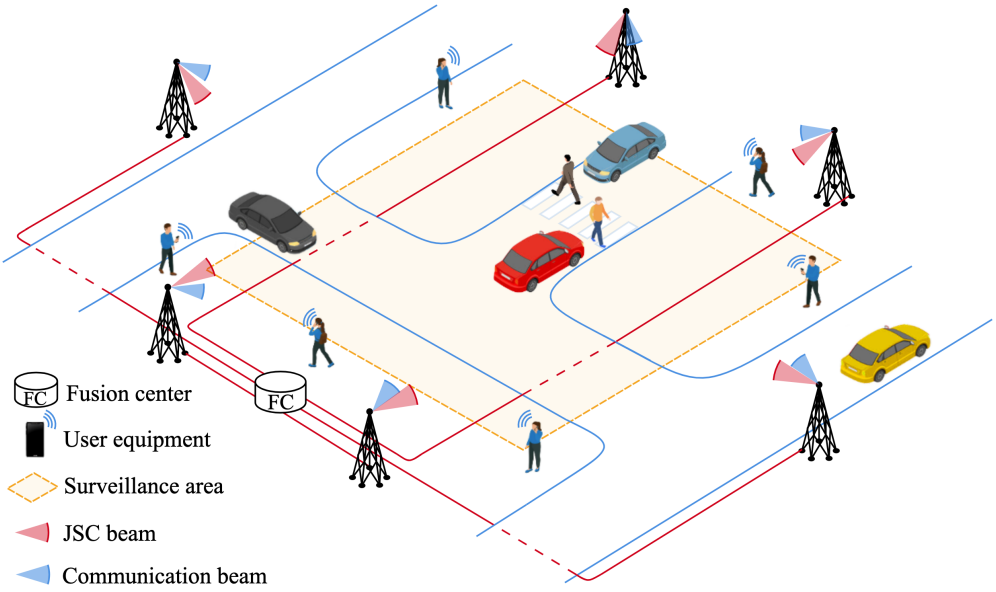

Figure 2.1: An urban scenario with six monostatic JSC BSs aiming at monitoring pedestrians (point-like targets) and vehicles (extended targets) in a surveilled area. BSs communicate with the associated UEs while simultaneously sensing the surrounding environment via dedicated JSC beams. The FC collects measurements from the BSs via the backhaul network, fuses them to create likelihood maps, and performs detection and multiple target tracking.

2.1 System Model

We consider a JSC network, illustrated in Fig. 2.1, which consists of multiple BSs operating at mmWave frequencies with monostatic sensing capability. Each BS transmits an OFDM waveform via multiple beams. In particular, while performing environment sensing through a dedicated beam and downlink signals, each BS simultaneously communicates with its UEs present in the scenario.[1] Through the backhaul network, the BSs cooperate with a FC to accomplish targets' detection and estimation via data fusion. To mitigate inter-cell interference, frequency-division (FD) and time-division (TD) are exploited among the BSs such that sensing beams do not interfere; this operation is usually performed also for communication.

[1]We consider the targets to be completely passive (i.e., they do not interact with the BS) and thus distinct from the UEs, though the framework can also accommodate scenarios where UEs are the targets to be localized.

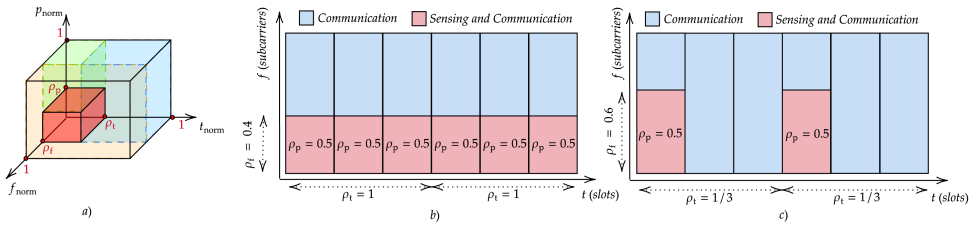

Figure 2.2: a) Graphical representation of the resource partition between communication and sensing at the BS. The red block represents the fraction of resources reserved for sensing, and the other blocks represent the remaining resources available for communication. b) Example of sensing and communication resource allocation in the time-frequency domain, with $\rho_{\text{p}} = 0.5$, $\rho_{\text{f}} = 0.4$, and $\rho_{\text{t}} = 1$. c) Another example with $\rho_{\text{p}} = 0.5$, $\rho_{\text{f}} = 0.6$, and $\rho_{\text{t}} = 1/3$.

To sense the surrounding environment, each BS uses a fraction of the available resources in the downlink. More precisely, the BS transmits multiple frames each consisting of M_{s} OFDM symbols with

$$\rho_{\text{f}} = K_{\text{s}}/K \tag{2.1}$$

the fraction of subcarriers for JSC among the total K active subcarriers available. The OFDM symbol duration T_{s} and the subcarrier spacing Δf are kept fixed. Multiple scans (measurements) of the surveillance area are performed to keep informed on the trajectory of the targets, with the time between two consecutive scans, T_{meas}, that can be varied to accommodate the communication/sensing trade-off. Hence, we indicate with

$$\rho_{\text{t}} = T_{\text{scan}}/T_{\text{meas}} \tag{2.2}$$

the fraction of time reserved for JSC. Consequently, the transmitted signal in JSC slots can be represented by a matrix $\mathbf{X} \in \mathbb{C}^{K_{\text{s}} \times M_{\text{s}}}$, where the elements $x_{k,m}$ correspond to complex modulation symbols with $\mathbb{E}\{|x_{k,m}|^2\} = 1$ [46].

Without loss of generality, each BS is equipped with two uniform linear arrays (ULAs) with half wavelength spacing, one with N_{T} antennas for transmission and the other with N_{R} antennas for reception (see Fig. 2.3). At the Tx, the beamforming vector at subcarrier k, $\mathbf{w}_{\text{T}}[k] \in \mathbb{C}^{N_{\text{T}} \times 1}$, is applied to

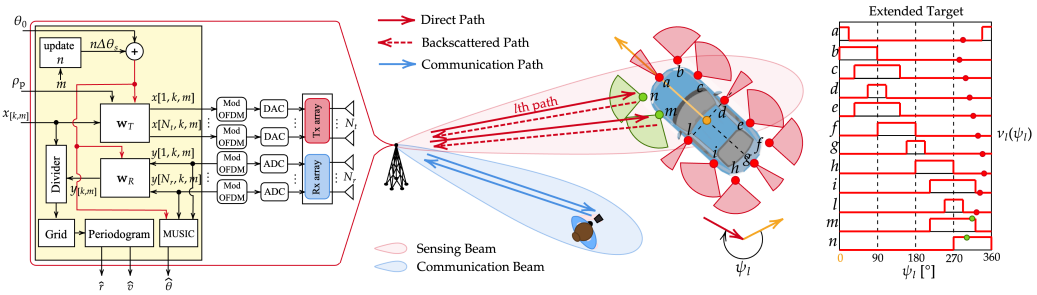

Figure 2.3: The MIMO-OFDM monostatic BS with multi-beam capability and a typical target vehicle. The vehicle is represented as an extended target made of distributed scatterers with specific visibility functions represented on the right.

data symbols at each antenna, resulting in $\mathbf{x}[k,m] = \mathbf{w}_{\mathrm{T}}[k]x_{k,m}$ [47].[2] Hence, the communication beam (directed towards the UE) and the sensing beam (steered to scan the area) [46, 48, 49] can be obtained by

$$\mathbf{w}_{\mathrm{T}}[k] = \sqrt{\rho_{\mathrm{p}}}\,\mathbf{w}_{\mathrm{s}}[k] + \sqrt{1-\rho_{\mathrm{p}}}\,\mathbf{w}_{\mathrm{c}}[k] \tag{2.3}$$

where $\rho_{\mathrm{p}} \in [0,1]$ represents the fraction of power reserved for sensing in JSC slots, thus determining the fraction of power apportioned to communication, i.e., $1-\rho_{\mathrm{p}}$, while $\mathbf{w}_{\mathrm{s}}[k]$ and $\mathbf{w}_{\mathrm{c}}[k]$ are the sensing and communication beamforming vectors, respectively. For ease of exposition, we consider the allocation of contiguous subcarriers to each UEs, akin to resource blocks in [50], and similarly, the JSC slots also use adjacent subcarriers. Hence, although ρ_{p} may vary between subcarriers, we consider $\rho_{\mathrm{p}} = 0$ for subcarriers dedicated to communication and consider the same ρ_{p} for those subcarriers belonging to the JSC slots. Nonetheless, solutions with non-contiguous resource allocation are also possible [51].

By considering a beam steering approach and performing a normalization to control the maximum effective isotropic radiated power (EIRP) $P_{\mathrm{T}}G_{\mathrm{T}}^{\mathrm{a}}$, the

[2] Without loss of generality, this thesis considers a single data stream at each OFDM time-frequency slot, used to serve one UE and perform sensing. This approach enables the same communication signal to be used for sensing while effectively mitigating potential interference between the two services. Multiple UEs are served simultaneously by allocating different resource blocks to each UE.

latter are[3]

$$\mathbf{w}_{\mathrm{s}}[k] = \frac{\sqrt{P_{\mathrm{T}} G_{\mathrm{T}}^{\mathrm{a}}}}{N_{\mathrm{T}}} \mathbf{a}_{\mathrm{T}}^{\mathsf{c}}\big(\theta_{\mathrm{s},k}\big), \quad \mathbf{w}_{\mathrm{c}}[k] = \frac{\sqrt{P_{\mathrm{T}} G_{\mathrm{T}}^{\mathrm{a}}}}{N_{\mathrm{T}}} \mathbf{a}_{\mathrm{T}}^{\mathsf{c}}\big(\theta_{\mathrm{c},k}\big) \tag{2.4}$$

where P_{T} is the transmit power, $G_{\mathrm{T}}^{\mathrm{a}}$ is the transmit array gain along the beam steering direction, and $\mathbf{a}_{\mathrm{T}}(\theta_{\mathrm{s},k}) \in \mathbb{C}^{N_{\mathrm{T}} \times 1}$ and $\mathbf{a}_{\mathrm{T}}(\theta_{\mathrm{c},k}) \in \mathbb{C}^{N_{\mathrm{T}} \times 1}$ are the steering vectors for sensing and communication directions, $\theta_{\mathrm{s},k}$ and $\theta_{\mathrm{c},k}$, respectively [46]. Note that this model accommodates multiple UEs and sensing beams using different beams on the subcarriers or groups thereof.

Fig. 2.2 provides a graphical representation of the resource allocation for communication and JSC sensing and an example of the evolution of these resources over time. It is noteworthy that within the time-frequency slots designated for JSC, two scenarios can unfold: a) the slot is solely dedicated to sensing ($\rho_{\mathrm{p}} = 1$); b) the slot accommodates one concurrent UE (i.e., one downlink communication beam), sharing resources with the sensing task according to (2.3).

At the sensing Rx, the symbols after OFDM demodulation are represented by[4]

$$\mathbf{y}[k,m] = \mathbf{H}[k,m]\mathbf{x}[k,m] + \mathbf{n}[k,m] \tag{2.5}$$

where $\mathbf{H}[k,m] \in \mathbb{C}^{N_{\mathrm{R}} \times N_{\mathrm{T}}}$ is the channel matrix for the mth symbol and the kth subcarrier, and $\mathbf{n}[k,m] \sim \mathcal{CN}(\mathbf{0}, \sigma_{\mathrm{N}}^2 \mathbf{I}_{N_{\mathrm{R}}})$ is the noise vector at the receiving antennas. In the considered sensing direction, defined by the angle $\theta_{\mathrm{s},k}$, spatial combining is performed using the receiving beamforming vector $\mathbf{w}_{\mathrm{R}}[k] = \mathbf{a}_{\mathrm{R}}^{\mathsf{c}}(\theta_{\mathrm{s},k})$. This process results in the formation of a grid of received symbols denoted as $\mathbf{Y} \in \mathbb{C}^{K_{\mathrm{s}} \times M_{\mathrm{s}}}$, where each element $y_{k,m}$ is obtained by

[3]The normalization applied here is aimed at regulating the maximum EIRP, a critical parameter that must adhere to spectrum regulations. However, when $\delta\theta = |\theta_{\mathrm{s},k} - \theta_{\mathrm{c},k}| \leq \mathrm{BW}/2$, i.e., when the sensing and communication beams are fully or partially aligned within the beamwidth $\mathrm{BW} \approx 2/N_{\mathrm{T}}$, an additional term of up to 3 dB may appear in the EIRP, depending on the values of ρ_{p} and $\delta\theta$. If needed, a scaling factor can be applied in such cases to ensure compliance with the EIRP constraint.

[4]Note that the monostatic radar configuration requires full-duplex architecture with analog/digital SI cancellation techniques (see, e.g., [20, 52]). However, modeling the SI resulting after cancellation and analyzing its effect on sensing performance at the sensing Rx is beyond the scope of this work. Therefore, following the approach discussed in [46], this work assumes good SI suppression, making it negligible with respect to Gaussian noise.

taking the inner product between the receiving beamforming vector $\mathbf{w}_{\mathrm{R}}[k]$ and the vector of the symbols received at each antenna $\mathbf{y}[k,m]$, i.e., $y_{k,m} = \mathbf{w}_{\mathrm{R}}^{\mathsf{T}}[k]\mathbf{y}[k,m]$. The collected symbols are subsequently used to generate range-angle maps as illustrated in Section 2.1.3.

The considered OFDM system operates over a wireless channel with a carrier frequency f_{c} and a maximum bandwidth $B = K\Delta f$, such that a narrowband assumption, i.e., $f_{\mathrm{c}} \gg B$, holds [53]. Under this hypothesis, the spatial steering vectors $\mathbf{a}_{\mathrm{T}}(\theta)$ and $\mathbf{a}_{\mathrm{R}}(\theta)$ for a ULA with half-wavelength inter-element spacing at a given AoA/angle of departure (AoD) θ is given by [54, Chapter 9], [47, Chapter 5]

$$\mathbf{a}_{\mathrm{T,R}}(\theta) = \left[1, e^{\imath\pi\sin(\theta)}, \ldots, e^{\imath\pi(N_{\mathrm{a}}-1)\sin(\theta)}\right]^{\mathsf{T}}$$

where N_{a} is the number of array antenna elements.

2.1.1 Multipath Channel Model

Let us begin by considering an anisotropic point-like scatterer labeled as l. This scatterer can either be a point-like target or a reflection point of a more complex object, referred to as an extended target. The channel model experienced during sensing is illustrated in Fig. 2.3. The signal emitted by the jth antenna propagates through the forward channel, from the BS to the scatterer, and is then reflected by the scatterer, propagating back to the ith antenna at the BS via the backscatter channel.

In the presence of the sole direct path in both forward and backscatter channels, the linear time-variant MIMO channel[5] is represented in the frequency domain by the channel matrix $\mathbf{H}[k,m]$ in (2.5), which takes the form [46, 55, 56]

$$\mathbf{H}_l[k,m] = \nu_l(\psi_l)\alpha_l e^{\imath\phi_l} e^{\imath 2\pi m T_{\mathrm{s}} f_{\mathrm{D},l}} e^{-\imath 2\pi k \Delta f \tau_l} \mathbf{a}_{\mathrm{R}}(\theta_l)\mathbf{a}_{\mathrm{T}}^{\mathsf{T}}(\theta_l)$$

where the function $\nu_l(\psi_l)$, dubbed visibility function, captures the scatterer anisotropy (i.e., it accounts for angular-dependent reflection properties) and ψ_l is the AoA at the target side for the BS-scatterer link; $\alpha_l \in \mathbb{R}$ is the gain

[5] The time-variant nature accounts for the Doppler effect due to target motion.

which accounts for the path-loss (described by the radar equation as this is the sensing channel) and the RCS of the scatterer, and ϕ_l is a uniformly distributed phase; τ_l, $f_{\mathrm{D},l}$, and θ_l are the round-trip delay, Doppler shift, and AoA/AoD of the ith (direct) Tx-scatterer-Rx path, respectively. Details will be provided in Section 2.1.2.

In the presence of multipath propagation represented by L_p paths between the BS and the scatterer, it can be shown that, due to linearity, the channel matrix in (2.5) becomes[6]

$$\begin{aligned}\mathbf{H}_l[k,m] = &\sum_{p=0}^{L_\mathrm{p}-1}\sum_{q=0}^{L_\mathrm{p}-1} \nu_l(\psi_l^p)\nu_l(\psi_l^q)\xi_l^p\xi_l^q e^{\imath(\phi_l^p+\phi_l^q)} \\ &\times e^{\imath 2\pi m T_\mathrm{s}(f_{\mathrm{D},l}^p+f_{\mathrm{D},l}^q)} e^{-\imath 2\pi k\Delta f(\tau_l^p+\tau_l^q)} \mathbf{a}_\mathrm{R}(\theta_l^p)\mathbf{a}_\mathrm{T}^\mathsf{T}(\theta_l^q)\end{aligned} \tag{2.6}$$

where ξ_l^r, ϕ_l^r, $f_{\mathrm{D},l}^r$, τ_l^r, and θ_l^r are the amplitude, phase, Doppler shift, delay, and AoA/AoD of the rth path (at the BS), respectively, while ψ_l^r are the angles at the scatterer side. The channel matrix (2.6) can be conveniently reformulated by separating the BS-scatterer-BS path (the one with $p=q=0$), with $(\xi_l^0)^2=\alpha_l$, from the diffuse component resulting into

$$\begin{aligned}\mathbf{H}_l[k,m] = &\underbrace{\nu_l(\psi_l)\alpha_l\, e^{\imath\phi_l} e^{\imath 2\pi m T_\mathrm{s} f_{\mathrm{D},l}} e^{-\imath 2\pi k\Delta f\tau_l} \mathbf{a}_\mathrm{R}(\theta_l)\mathbf{a}_\mathrm{T}^\mathsf{T}(\theta_l)}_{\text{direct path}} \\ &+ \underbrace{\sum_{(p,q)\in\mathcal{J}\setminus(0,0)}\sum \nu_l(\psi_l^p)\nu_l(\psi_l^q)\xi_l^p\xi_l^q e^{\imath(\phi_l^p+\phi_l^q)} \\ &\times e^{\imath 2\pi m T_\mathrm{s}(f_{\mathrm{D},l}^p+f_{\mathrm{D},l}^q)} e^{-\imath 2\pi k\Delta f(\tau_l^p+\tau_l^q)} \mathbf{a}_\mathrm{R}(\theta_l^p)\mathbf{a}_\mathrm{T}^\mathsf{T}(\theta_l^q)}_{\text{diffuse component}}\end{aligned} \tag{2.7}$$

where $\mathcal{J}=\{0,\ldots,L_\mathrm{p}-1\}\times\{0,\ldots,L_\mathrm{p}-1\}$ is the set containing all path indexes.

Note that the diffuse component in (2.7) vanishes in the absence of multipath. Typically, the diffuse part remains unknown to the sensing Rx; thus, it can act as a disturbance, causing target smearing in the range-angle maps,

[6] An interesting interpretation provided in [57, 58] is that the overall channel impulse response (CIR) can be represented as the convolution between two CIRs: one from the so-called forward channel and the other from the backscatter channel. These CIRs are scaled by a factor that accounts for the path-loss and RCS of the target.

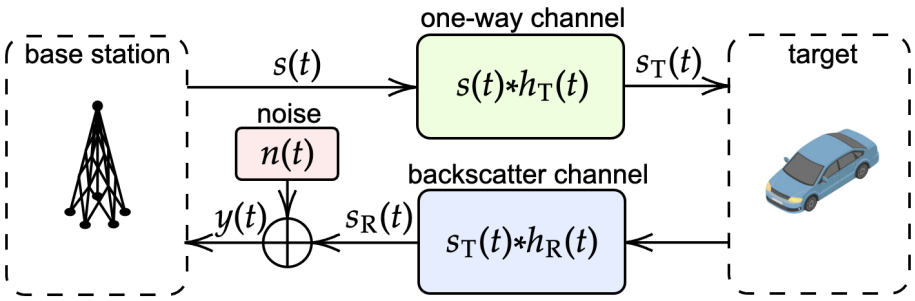

Figure 2.4: Signal model for multipath in the monostatic JSC system.

as it will be shown in Section 2.3. Due to multiple paths, even a single scatterer is sensed as a superposition of various components with distinct delays, Doppler shifts, and AoAs, spreading the target across all three domains.

In the presence of L_s point-like targets or a single extended target modeled as a collection of L_s scatterers, the channel matrix becomes

$$\mathbf{H}[k,m] = \sum_{l=1}^{L_\mathrm{s}} \mathbf{H}_l[k,m] \tag{2.8}$$

which contains L_s direct paths plus $L_\mathrm{s}(L_\mathrm{p}^2 - 1)$ diffuse paths.

By substituting (2.8) into (2.5), the vector of received symbols at each antenna can be rewritten as

$$\mathbf{y}[k,m] = \left(\sum_{l=1}^{L_\mathrm{s}} \mathbf{H}_l[k,m] \right) \mathbf{x}[k,m] + \mathbf{n}[k,m] \tag{2.9}$$

where $\mathbf{H}_l[k,m]$ is defined as in (2.7).

2.1.2 Target Model

In this work, we consider a scenario featuring cars represented by the extended target model depicted in Fig. 2.5 and pedestrians as point-like targets. The channel matrix outlined in (2.7) and (2.8) accounts for the reflections caused by each scatterer, resulting in the generation of one or more backscattered signals. For each scatterer, the gain α_l includes the attenuation along the BS-scatterer-BS path, which can be related to the radar equation, and

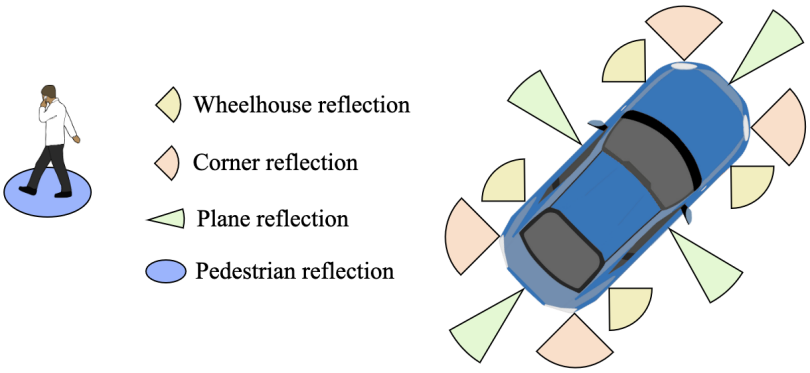

Figure 2.5: Extended target model adopted to represent the vehicle reflections and point-like model to represent pedestrian reflections. Different colors represent various types of reflections.

results in [54]

$$\alpha_l = \sqrt{\frac{G_{\mathrm{R}} c^2 \sigma_l}{(4\pi)^3 f_{\mathrm{c}}^2 d_l^4}} \tag{2.10}$$

where G_{R} is the gain of the single antenna element at the Rx, c represents the speed of light, σ_l is the lth reflection point RCS, and d_l is the distance between the lth reflection point and the considered BS. The scatterers adhere to the Swerling I model, i.e., with probability density function (p.d.f.) given by [59]

$$f(\sigma_l) = \frac{1}{\bar{\sigma}_l} \exp\left(-\frac{\sigma_l}{\bar{\sigma}_l}\right) \qquad \sigma_l \geq 0 \tag{2.11}$$

which is constant during the collection of a block of M_{s} symbols, and independent from block to block, with $\bar{\sigma}_l = \mathbb{E}\{\sigma_l\}$.

The pedestrian is modeled as a point-like target with $\bar{\sigma}_l = 0\,\mathrm{dBms}$. The car is an extended target consisting of $L_{\mathrm{s}} = 12$ reflection points, including 4 reflections attributed to the front, back, and sides, each with a large RCS ($\bar{\sigma}_l = 20\,\mathrm{dBms}$). Additionally, there are 4 reflections associated with the wheelhouses ($\bar{\sigma}_l = 0\,\mathrm{dBms}$) and 4 reflections originating from the corners ($\bar{\sigma}_l = 5\,\mathrm{dBms}$) [60,61]. Each scatterer is anisotropic, and its angle-dependent reflectivity is modeled through the visibility function $\nu_l(\psi_l)$, which characterizes the angular range where the scatterer exhibits an appreciable RCS; in contrast, the RCS is negligible outside that angular range. Recalling that ψ_l

is the AoA at the target side for the BS-scatter link, for the car, $\nu_l(\psi_l) = 1$ for $\psi_l \in [\Psi_{\min,l}, \Psi_{\max,l}]$ and 0 elsewhere, with $\Psi_{\min,l}$ and $\Psi_{\max,l}$ defined for the specific scatterer type (e.g., corner, wheelhouse, etc.) [60, 61]. The visibility functions adopted in this work are shown in Fig. 2.3. Note that the number of back-scattered signals varies over time because the number of reflections generated by the extended target depends on its position and orientation for the considered BS, according to the visibility function. Each scatterer, when visible, is associated with the RCS model in (2.11). Channels experienced by different scatterers are considered statistically independent; such an assumption is plausible because the scattering points of the extended target are spaced apart by several wavelengths at mmWave.

2.1.3 Range-Angle Map at the Base Station

To detect objects within the environment, each BS uses a combination of two beams specified by $\mathbf{w}_{\mathrm{T}}[k]$ in (2.3). The communication beam is aimed at a particular UE, while the sensing beam is periodically steered within the range $[-\Theta, \Theta]$ with a fixed angular increment $\Delta\Theta$. A group of M_{s} OFDM symbols is transmitted to produce a range-angle map for every sensing direction. The duration of a full scan, referred to as T_{scan}, is determined by the number of sensing orientations chosen and the duration of each OFDM symbol, T_{s}. After collecting all symbols in a given scan direction in the matrix $\mathbf{Y}$, the first stage is to perform reciprocal filtering, which consists of an element-wise division between the received and the transmitted grids, i.e., $\mathbf{Y}$ and $\mathbf{X}$, to remove the dependence on the transmitted symbols and obtain a new matrix $\mathbf{G}$ whose elements are [18, 46, 62]

$$g_{k,m} = \frac{y_{k,m}}{x_{k,m}} = \mathbf{w}_{\mathrm{R}}^{\mathsf{T}}[k]\mathbf{H}[k,m]\mathbf{w}_{\mathrm{T}}[k] + \frac{\mathbf{w}_{\mathrm{R}}^{\mathsf{T}}[k]\mathbf{n}[k,m]}{x_{k,m}}. \tag{2.12}$$

Then, a double-periodogram is computed on the rows and columns of $\mathbf{G}$ to obtain a range-Doppler map, following the approach outlined in [18, 20, 46]

$$\mathcal{P}(q,p) = \frac{1}{K_{\mathrm{s}}M_{\mathrm{s}}} \left| \sum_{k=0}^{K_{\mathrm{p}}-1} \left(\sum_{m=0}^{M_{\mathrm{p}}-1} g_{k,m} e^{-j2\pi \frac{mp}{M_{\mathrm{p}}}} \right) e^{j2\pi \frac{kq}{K_{\mathrm{p}}}} \right|^2 \tag{2.13}$$

Given the relatively narrow beamwidth, we assume that only one scatterer will likely be present in each sensing direction. Therefore, the range-angle map is calculated by selecting the column of the periodogram $\mathcal{P}(q,p)$ with the maximum value, thereby associating it uniquely with the corresponding sensing direction.[7]

As further illustrated in Section 2.3, the aforementioned approach, based on beam scanning at each BS, can handle dynamic scenarios, such as the one considered in this work, where the number of targets within the monitored area varies over time.

2.1.4 Network Capacity and Communication Overhead

The dual functional capability of the BS is ensured by considering frequency-division outlined in (2.1), time-division given in (2.2), and power-division reported in (2.3). According to (2.3), at the single-antenna UE the received OFDM symbol at the subcarrier k and time m is

$$r_{k,m} = \alpha_{\mathrm{c}} \mathbf{h}_{\mathrm{c}}^{\mathsf{T}}[k,m]\mathbf{w}_{\mathrm{T}}[k]x_{k,m} + \nu_{k,m} \tag{2.14}$$

where

$$\alpha_{\mathrm{c}} = \sqrt{\frac{G_{\mathrm{R}}c^2}{(4\pi)^2 f_{\mathrm{c}}^2 d_{\mathrm{c}}^{\beta}}} \tag{2.15}$$

with d_{c} the BS-UE distance and β the path-loss exponent. Moreover, $\mathbf{h}_{\mathrm{c}}[k,m] \in \mathbb{C}^{N_{\mathrm{T}}\times 1}$ is the channel vector for the mth symbol and the kth subcarrier, and $\nu_{k,m} \sim \mathcal{CN}(0,\sigma_{\mathrm{c}}^2)$ is the receiver noise at the UE. Without loss of generality, we consider the elements of $\mathbf{h}_{\mathrm{c}}[k,m]$ as independent, identically distributed (i.i.d.) Gaussian random variables (r.v.s) such that each element is Rice distributed in amplitude with Rice factor K_{rice}, $\mathbb{E}\{|h_{\mathrm{c},j}|^2\} = 1$ for $j = 1,\ldots,N_{\mathrm{T}}$; we consider a block-fading channel so we drop the index m.

Note that equation (2.14) accounts for both communication in the presence of sensing (red blocks in Fig. 2.2) but can model the received signal also in slots where sensing is not activated, i.e., $\rho_{\mathrm{p}} = 0$ (blue blocks in Fig. 2.2). However, in the former case, symbols $x_{k,m}$ belong to a quadrature phase shift

[7] This is a low-complexity solution that can be readily replaced with alternative approaches such as 2D-MUSIC [63].

keying (QPSK) constellation, while in the latter case, $x_{k,m}$ can belong to any constellation. Indeed, the use of QPSK in JSC slots ensures high sensing performance because of its constant modulus [64, 65].

Therefore, at the UE, the signal-to-noise ratio (SNR) per subcarrier conditioned on a given channel realization is

$$\mathrm{SNR}_k(\rho_\mathrm{p}) = \frac{\alpha_\mathrm{c}^2}{\sigma_\mathrm{c}^2} \left|\mathbf{h}_\mathrm{c}^\mathsf{T}[k]\mathbf{w}_\mathrm{T}[k]\right|^2 \tag{2.16}$$

where we have emphasized its dependence on the sensing power allocation parameter (2.3).

The assignment of resources to sensing inevitably influences communication performance. To assess this impact, we consider the ergodic capacity, defined as the average downlink sum rate of each BS, calculated as[8]

$$\begin{aligned} C_\mathrm{DL}\left(\rho_\mathrm{f}, \rho_\mathrm{t}, \rho_\mathrm{p}\right) = \rho_\mathrm{t}\, \Delta f \sum_{k=1}^{\lfloor \rho_\mathrm{f} K \rceil} \mathbb{E}\big\{ C_\mathrm{JSC}\big(\mathrm{SNR}_k(\rho_\mathrm{p})\big)\big\} \\ + \rho_\mathrm{t}\, \Delta f \sum_{k=\lfloor \rho_\mathrm{f} K+1 \rceil}^{K} \mathbb{E}\big\{ \log_2\left(1+\mathrm{SNR}_k(0)\right)\big\} \\ + (1-\rho_\mathrm{t}) \Delta f \sum_{k=1}^{K} \mathbb{E}\big\{ \log_2\left(1+\mathrm{SNR}_k(0)\right)\big\} \end{aligned} \tag{2.17}$$

where the expectation is taken with respect to the channel statistics [66], and $C_\mathrm{JSC}\left(\gamma\right)$ is the capacity of the JSC slots. Indeed, while slots allocated for communication may use any constellation and the sum rate for them is calculated via the usual Shannon capacity, the JSC slots utilize QPSK.[9]

[8] To streamline the scenario, we consider that each BS can use all the available resources.

[9] For QPSK signaling, a tight approximation of the capacity can be found in [67]:

$$C_\mathrm{JSC}(\gamma) = 2(1 - a_1 e^{-b_1\gamma} - a_2 e^{-b_2\gamma})$$

where γ is the SNR, $a_1 = 0.143281$, $a_2 = 0.856719$, $b_1 = 1.557531$, and $b_2 = 0.57239$.

Algorithm 1 Construction of the Range-Angle Map

Initialize empty matrix $\mathcal{M}$
for each beamforming direction j **do**
    Illuminate the scene with direction $\theta_{\mathrm{s},k,j}$
    Compute $\mathcal{P}(q,p)$
    Find the column $\hat{p}$ corresponding to the peak value in $\mathcal{P}(q,p)$
    Extract the vector $\mathcal{P}(:,\hat{p})$ (entire column at $\hat{p}$)
    Append $\mathcal{P}(:,\hat{p})$ as a new column in $\mathcal{M}$
end for
Linearly interpolate $\mathcal{M}$ onto a uniform grid $\mathbf{L}_{s,t}$
Output: Interpolated Range-Angle Map $\mathbf{L}_{s,t}$

2.2 Multi-Sensor Data Fusion and Estimation

2.2.1 Maps Fusion from Multiple Cooperating BS

The strategy implemented to process the range-angle maps obtained by the network of JSC BSs is depicted in Fig. 2.6 and described in Algorithm 1. At time t, each BS s performs a uniform resampling procedure with grid resolution Δ_{x} and Δ_{y} to ensure consistent map fusion, where each element of the new grid is described by indices (i_x, i_y). Target detection is performed on the range-angle maps using a binary hypothesis test with a threshold γ_{s}, which is applied to differentiate between noise and potential targets. The test can be expressed as:

$$\mathbf{L}_{s,t}(i_x, i_y) \underset{\mathcal{H}_0}{\overset{\mathcal{H}_1}{\gtrless}} \gamma_{\mathrm{s}}, \tag{2.18}$$

where $\mathcal{H}_0$ and $\mathcal{H}_1$ correspond to the hypotheses of noise-only and target presence, respectively. The threshold γ_{s} is selected to achieve a specific point-level false alarm probability $P_{\mathrm{FA,point}}$, which is linked to the overall false-alarm rate (FAR) in the search area of size $|\mathbf{L}_{s,t}|$ by the relationship $P_{\mathrm{FA,point}} = \mathrm{FAR}/|\mathbf{L}_{s,t}|$.

Under the assumption of noise-only conditions, the values of $\mathbf{L}_{s,t}$ follow an exponential distribution with a mean proportional to the noise power, σ^2_{N}. This enables us to determine the threshold γ_{s} as:

$$\gamma_{\mathrm{s}} = -\sigma_{\mathrm{N}}^2 \ln P_{\mathrm{FA,point}}. \tag{2.19}$$

This filtering process is applied independently to range-angle maps at each BS, ensuring that only the most significant points with sufficiently high SNR are retained and exchanged with the FC, thereby reducing network overhead. Although the maps are subjected to the same detection thresholding rule, the resulting contributions to fusion are inherently weighted by the local noise conditions: BSs experiencing high interference or low SNR retain fewer significant detections and hence contribute less to the fusion process. Conversely, BSs operating under favorable conditions preserve more map information and thus play a larger role in the cooperative fusion. Moreover, collaboration across multiple BSs enhances the detection reliability, as targets missed by one BS may still be identified by others. This cooperative approach strengthens overall system performance by leveraging the diversity of the distributed sensing network.

At the FC, the resampled and filtered range-angle maps $\mathbf{L}_{s,t}$ are processed to suppress the effects of multipath and enhance the reliability of detections. This is achieved through a double-weighting approach.

Initially, the coverage of each point in the resampled map is evaluated by counting the number of sensors that detect the same point, resulting in a coverage matrix $\mathbf{A}_t$ of the same dimensions as $\mathbf{L}_{s,t}$. A weighting factor is then computed based on this coverage. Specifically, the weight assigned to a point covered by $n_{\mathrm{s}} = 1, \ldots, N_{\mathrm{s}}$ sensors is given by

$$w = \min\left(1, w_{\max} \cdot n_{\mathrm{s}}^4\right), \tag{2.20}$$

where $w_{\max} = \frac{1}{N_{\mathrm{s}}^4}$ is the minimum weight for a point covered by only one BS, and N_{s} denotes the total number of BS. This weighting scheme ensures that points covered by only one sensor, which are more likely to result from noise or multipath effects, are assigned a lower weight, thereby mitigating their impact on the overall performance.

After computing the weights, a new weighted map is generated at each sensor. The weighted maps from all sensors are then combined using element-

wise summation to form the soft map

$$\mathbf{L}_t = \frac{1}{N_\mathrm{s}} \sum_{s=1}^{N_\mathrm{s}} \mathbf{L}_{s,t}, \tag{2.21}$$

where t is the time index. This process results in a fused map that leverages multi-sensor coverage to enhance target detection and suppress channel-specific multipath artifacts.

In [48], an alternative solution is proposed in which the target state (position coordinates and velocity components) is estimated at each BS and then refined at the FC through data fusion. However, this approach is less accurate than the one presented in this work due to the information loss associated with estimates based on local decisions.

2.2.2 Target Clustering

Clustering is employed to detect targets from the fused map. As an initial step, an excision filter is applied to the matrix $\mathbf{L}_t$ to filter out those elements of the map that are likely due to noise or clutter. Given the lack of prior knowledge regarding noise, clutter, number of targets, and their features, we adopt a scenario-dependent threshold. Specifically, we determine the threshold γ_d based on a fixed percentile of the map values. This approach ensures that only the top fraction of the map—corresponding to the most prominent elements—is considered for target estimation. The threshold γ_d is thus defined as:

$$\gamma_\mathrm{d} = \mathrm{Percentile}_\mathrm{d}\left(\mathrm{vec}\left(\mathbf{L}_t\right)\right), \tag{2.22}$$

where $\mathrm{Percentile}_\mathrm{d}(\cdot)$ represents the d-th percentile operation, and $\mathrm{vec}(\mathbf{L}_t)$ denotes the vectorized form of the matrix $\mathbf{L}_t$. This criterion ensures that only the top $1 - \mathrm{d}$ of the map values are used in the subsequent target estimation process.

Subsequently, a density-based spatial clustering of applications with noise (DBSCAN) algorithm is employed to perform clustering. This algorithm specifies a maximum distance ξ_d for points to be considered part of the same cluster, as well as a minimum number of points, denoted as N_d, required to

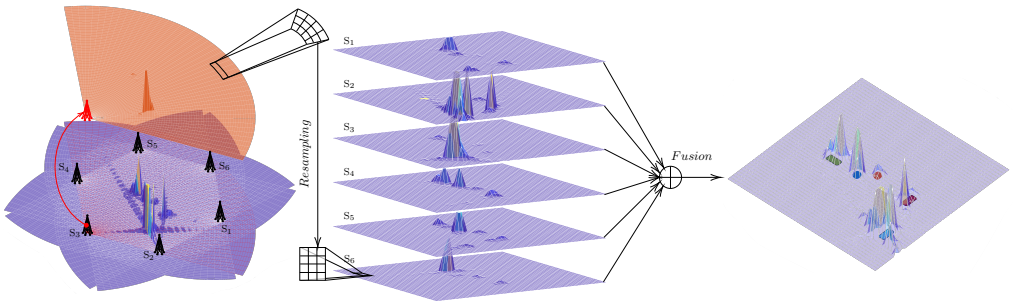

Figure 2.6: Soft map fusion strategy. The maps shown are obtained from the simulations reported in the numerical results considering the vehicle scenario described in Section 2.3.

form a cluster (as described in [68]). Lastly, each cluster centroid is stored in the matrix $\mathbf{Z}_t$, representing the target detections extracted from the soft maps.

2.3 Numerical Results

In this section, we present numerical results to explore the interplay between communication and sensing. We investigate the impact of the amount of power dedicated to sensing ρ_{p}, the fraction of subcarriers ρ_{f} and the fraction of time ρ_{t}.

2.3.1 Performance Metrics

The dual-function system is investigated under two perspectives: communication and sensing performance: The communication performance is evaluated through the sum rate in (2.17), which measures the downlink network capacity of each BS given a particular set of resources reserved for communication. The cost of sensing is estimated in terms of sum rate reduction Since a complex scenario with multiple point-like and extended targets and multipath propagation is considered, the GOSPA metric is used to evaluate the sensing performance of the network, also in terms of cooperation gain. This metric is widely used to evaluate the performance in multi-target (or multi-scatterer) scenarios, as it allows to combine localization and detection

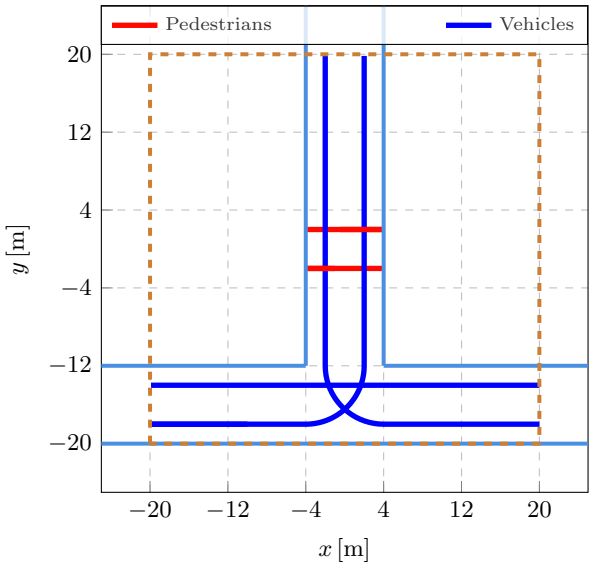

Figure 2.7: Targets behavior in the considered scenario. Orange dashed square represents the surveillance area, while light blue lines represent lanes.

performance into a single metric, taking into account false alarms and missed detections [69]. The p-order GOSPA metric is defined as [70, 71]

$$\text{GOSPA} = \left[\frac{1}{N_\text{c}} \left(\sum_{(i,j)\in\boldsymbol{\zeta}_\text{g}^*} \|\underline{\mathbf{z}}_{t,i} - \hat{\underline{\mathbf{z}}}_{t,j}\|_p^p + \frac{\xi_\text{g}^p}{2}(|\underline{\mathbf{Z}}_t| + |\hat{\underline{\mathbf{Z}}}_t| - 2|\boldsymbol{\zeta}_\text{g}^*|) \right) \right]^{\frac{1}{p}} \tag{2.23}$$

where $\hat{\underline{\mathbf{Z}}}_t$ represents the first two rows of $\hat{\mathbf{Z}}_t$ which is a matrix containing the estimated state vectors of all the detected targets at time t; hence $\hat{\mathbf{Z}}_t$ retains only the estimated target positions. Moreover, the parameter ξ_g represents the GOSPA gate: estimated positions that are farther than ξ_g from the actual target positions are considered as false alarms and, dually, real target positions that are not associated with any estimates (because not inside the gate) will be counted as missed detections. The vector $\boldsymbol{\zeta}_\text{g}^*$ represents the best assignment between the estimated set of objects $\hat{\underline{\mathbf{Z}}}_t$ and the true ones $\underline{\mathbf{Z}}_t$, while $|\hat{\underline{\mathbf{Z}}}_t|$, $|\underline{\mathbf{Z}}_t|$, and $|\boldsymbol{\zeta}_\text{g}^*|$ are the cardinalities of the considered set, namely, the number of objects in the estimated state vector, the ground truth cardinality, and the data association vector, respectively. Finally, N_c is the number of elements in the GOSPA metric given by $N_\text{c} = |\underline{\mathbf{Z}}_t| + |\hat{\underline{\mathbf{Z}}}_t| - |\boldsymbol{\zeta}_\text{g}^*|$.

Table 2.1: System parameters

Base station		
$\Delta_\mathrm{x}, \Delta_\mathrm{y}$	Resampling grid resolution [m]	0.1
N_s	Number of base stations	6
T_scan	Scan period [s]	0.05
ρ_p	Fraction of power reserved for sensing	
ρ_t	Fraction of time reserved for sensing	
ρ_f	Fraction of frequency reserved for sensing	
FAR	false alarm rate	10^{-3}
Clustering		
d	d-percentile	97
ξ_d	Gate DBSCAN [m]	2.5
N_d	Minimum number of points DBSCAN	50
GOSPA metric		
p	GOSPA order	2
ξ_g	GOSPA gate [m]	2 5 10

When $p = 2$, the first term in (2.23) can be interpreted as the mean square error between the estimated and actual target positions. Instead, the second term can be rewritten as

$$\frac{\xi_\mathrm{g}^p}{2}(|\underline{\mathbf{Z}}_t| - |\boldsymbol{\zeta}_\mathrm{g}^*|) + \frac{\xi_\mathrm{g}^p}{2}(|\hat{\underline{\mathbf{Z}}}_t| - |\boldsymbol{\zeta}_\mathrm{g}^*|)$$

such that the first term is proportional to the missed detection rate, while the second one is related to the false detection rate, which are defined as

$$R_\mathrm{D} = \frac{|\boldsymbol{\zeta}_\mathrm{g}^*|}{|\underline{\mathbf{Z}}_t|}, \quad R_\mathrm{FA} = \frac{|\hat{\underline{\mathbf{Z}}}_t| - |\boldsymbol{\zeta}_\mathrm{g}^*|}{|\hat{\underline{\mathbf{Z}}}_t|}, \quad R_\mathrm{MD} = 1 - R_\mathrm{D}.$$

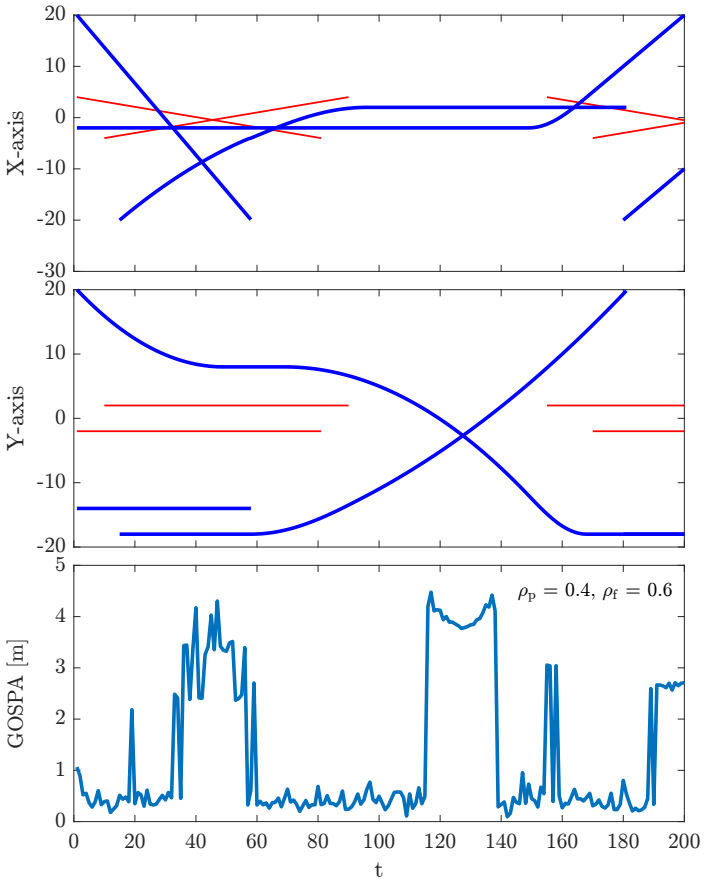

Figure 2.8: Temporal evolution of the scenario depicted in Fig. 2.7. The top and middle plots show the trajectory evolution over time in the x and y coordinates, respectively. The bottom plot illustrates the GOSPA error ($\xi_g = 5\,\text{m}$) as a function of time when $\rho_p = 0.4$ and $\rho_f = 0.6$.

2.3.2 System and Scenario Parameters

We considered a vehicular scenario with 6 BSs and a set of extended and point-like targets, whose behavior is depicted in Fig. 2.7. Pedestrians move with uniform linear motion, whereas vehicles' motion is modeled alternating static, accelerated/decelerated linear, uniform linear, and uniform circular motions. In the simulated scenario, vehicles reach a maximum speed of 14 m/s (50.4 km/h), while pedestrians are moving with a maximum speed of 2 m/s (7.6 km/h). The area monitored is a typical crossroad of $1600\,\text{m}^2$, with $x \in [-20,\, 20]\,\text{m}$ and $y \in [-20,\, 20]\,\text{m}$. The main parameters are summarized in Table 2.1.

The transmission parameters are: QPSK modulation, $f_c = 28\,\text{GHz}$, $\Delta f = 120\,\text{kHz}$, $K = 3168$ (i.e., about 400 MHz bandwidth), $M = 1120$, and $M_s = 112$. The EIRP is set to 30 dBm, and the one-sided noise power spectral density (PSD) is $N_0 = 4 \cdot 10^{-20}\,\text{W/Hz}$. The BSs are equipped with $N_T = N_R = 50$ antennas, and $G_R = 1$.

The multipath propagation is simulated using the 3GPP 38.901 urban micro-cell line-of-sight (LOS) scenario [50]. Parameters such as ξ_l^r, ϕ_l^r, τ_l^r, $f_{D,l}^r$, θ_l^r, and ψ_l^r are generated using the QUAsi Deterministic RadIo channel GenerAtor (QuaDRiGa) software [72] for each target and position along the trajectories. Specifically, for each scatterer, the model considers the direct path and the 5 strongest paths of the diffuse component, for a total of $L_p = 6$ paths. This results in a monostatic CIR with $L_p^2 = 36$ paths, as per (2.6). The six BSs are positioned along a circumference with a radius of 50 m, centered on the surveilled area. Their ULAs are tangent to the circumference (i.e., orthogonal to the radius), providing a scanning area of 120° with a maximum sensing distance of 85 m to prevent inter-symbol interference (ISI). Each BS performs a scan lasting $T_{scan} = 50\,\text{ms}$, and the overall scene is monitored for 10 s, resulting in the collection of $N_m = 200$ measurements (maps). The grid resolution is set to $\Delta_x = 0.1\,\text{m}$ and $\Delta_y = 0.1\,\text{m}$. The number of bits selected to represent each map point is set to $N_b = 16$. The sensing beam is periodically steered within the range $[-\Theta, \Theta]$, where $\Theta = 60\,°$, with a fixed angular increment of $\Delta\Theta = 2.4°$.

For the communication scenario, we considered the presence of 6 UEs in the same urban micro-cell LOS environment. Each UE is served by a different BS, the UE downlink ergodic capacity is evaluated varying the distance between UE and BS from 35 m to 85 m, with a step of 10 m, fixing $\theta_c = 70°$, from the associated BS. The links are characterized by a path-loss exponent $\beta = 2.1$ and Rice fading with $K_{rice} = 10$ [50]. Without loss of generality, we considered $\sigma_N^2 = \sigma_c^2 = N_0 K \Delta f$.

When the targets are spatially separated, the clustering algorithm accurately estimates both the correct number of targets and their respective positions. This behavior can be observed in the first two plots of Fig. 2.8, where the target trajectories evolve independently. However, when the targets overlap, the clustering algorithm struggles to correctly distinguish be-

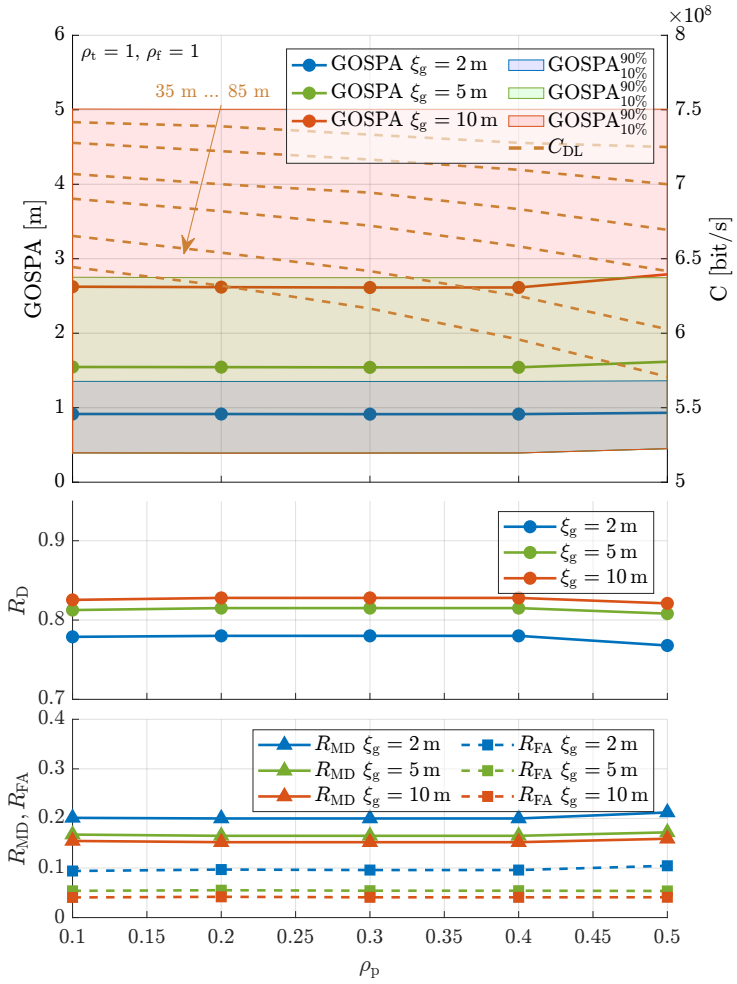

Figure 2.9: Communication and sensing performance varying the fraction of power reserved for JSC ρ_p. The downlink ergodic capacity is per BS.

tween them, resulting in errors in the estimated target count and positions. This limitation is reflected in the increased GOSPA error, as shown in the bottom plot. A potential solution to mitigate this issue is the application of a tracking algorithm, as demonstrated in [73], which can improve the ability to distinguish overlapping targets and reduce the GOSPA error.

2.3.3 Impact of the Fraction of Power ρ_p

In Fig. 2.9, the sensing and communication performance metrics are reported by varying the fraction of power dedicated to sensing, ρ_p, when $\rho_f = 1$ and

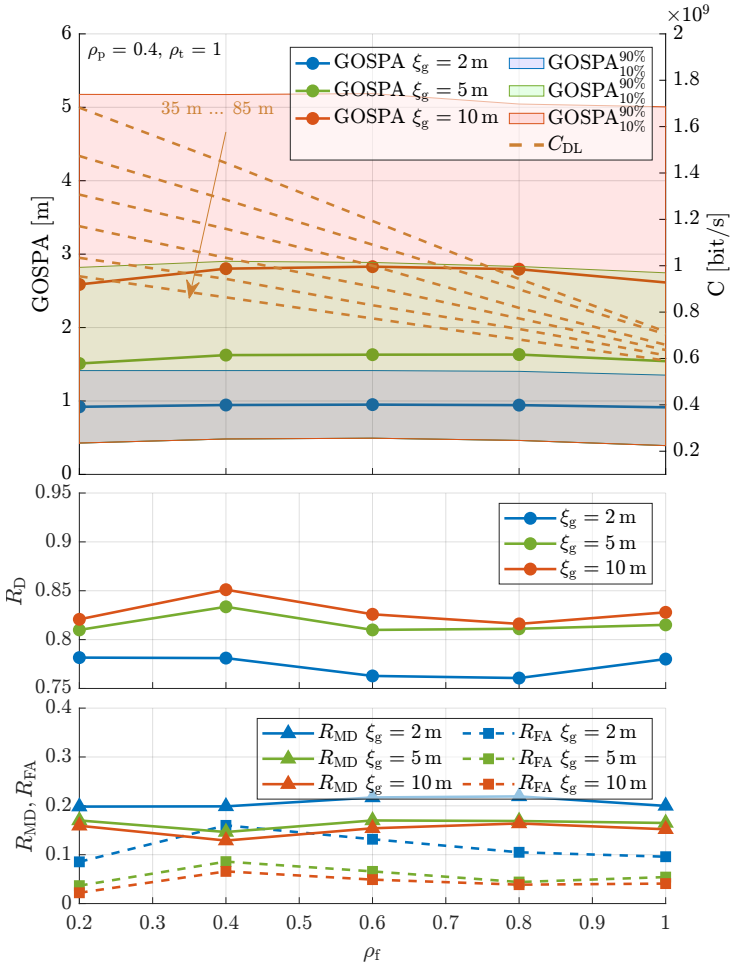

Figure 2.10: Communication and sensing performance varying the fraction of subcarriers reserved for JSC ρ_f. The downlink ergodic capacity is per BS.

$\rho_t = 1$.

At the top of each figure, the average GOSPA metric is shown for different gating thresholds, with the shaded area indicating the range between the 90th and 10th percentiles of the GOSPA distance. At the bottom, the detection rate, miss detection rate, and false detection rate are reported. This layout is consistent across all subsequent figures. It can be seen that, as the gating threshold increases, the average GOSPA also increases, while both the miss detection rate and the false detection rate decrease. This trend occurs because larger gates reduce the number of unassociated measurements, but penalize the remaining mismatches more heavily, assigning them an er-

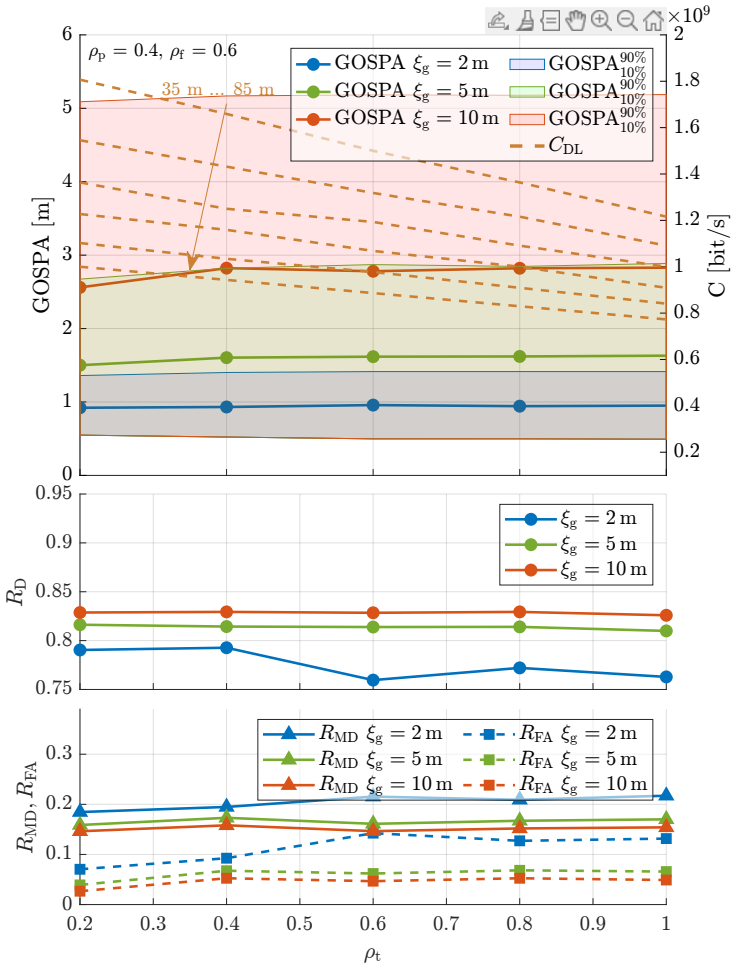

Figure 2.11: Communication and sensing performance varying the fraction of time reserved for JSC ρ_t. The downlink ergodic capacity is per BS.

ror equal to the gate value. Conversely, smaller gates lead to more missed and false detections due to stricter association criteria, but the penalty for these unassociated measurements is lower. Based on this trade-off, the discussion in the remainder of this work will focus on the results obtained with a GOSPA gate of 5 m, which provides a balanced compromise between association strictness and error magnitude. It is interesting to note that for large values of ρ_p (e.g., 0.5), the GOSPA distance experiences a subtle increase, due to decreased detection rate caused by multipath propagation, which becomes more relevant by increasing the sensing transmission power. From a communication perspective, in all numerical results, yellow dashed curves represent

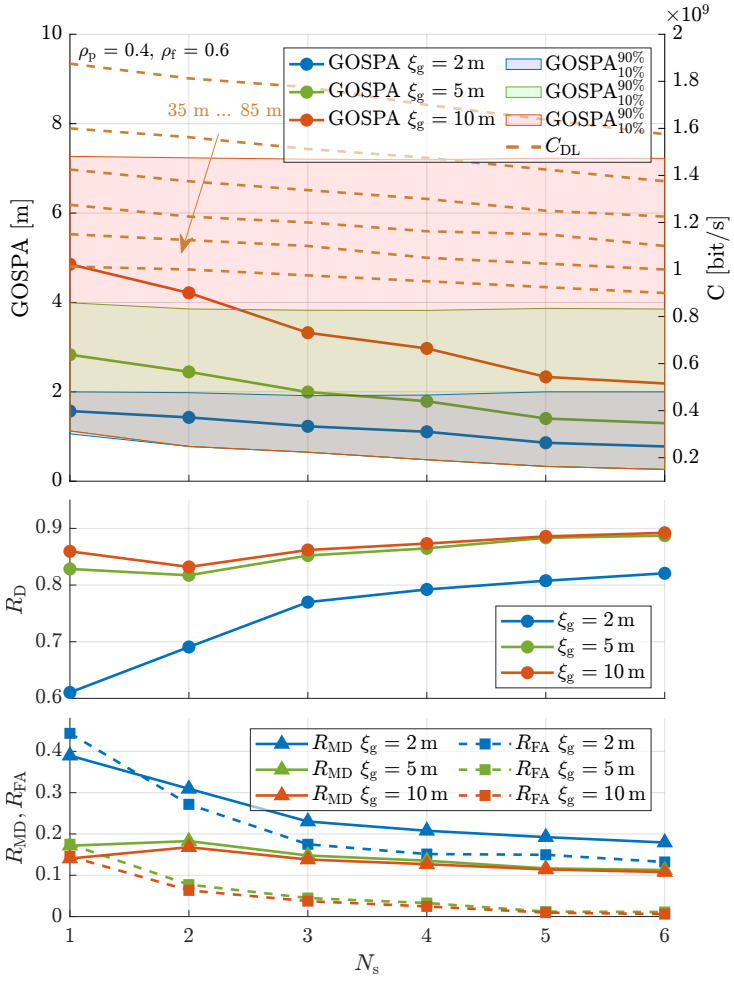

Figure 2.12: Communication and sensing performance varying the number of BSs adopted for sensing N_s. The downlink ergodic capacity is per BS.

the downlink ergodic capacity defined in (2.17), varying the distance between UE and associated BS, ranging from 35 m to 85 m with steps of 10 m. As expected, increasing ρ_p results in lower downlink capacity. In particular, for $\rho_p = 0.1$, the localization error is around 1.5 m, while the capacity for a UE at intermediate distance from its BS (55 m) is 0.71 Gbit/s. Increasing ρ_p to 0.4 slightly increases the GOSPA error to 1.54 m, while reducing the capacity to 0.68 Gbps, which represents a 4.2 % loss in communication performance.

2.3.4 Impact of the Fraction of Subcarriers ρ_f

Communication and sensing performance metrics, varying the frequency resources allocation between the two functions, are depicted in Fig. 2.10, considering $\rho_\mathrm{p} = 0.4$ and $\rho_\mathrm{t} = 1$.

From a sensing perspective, it is interesting to observe that as ρ_f decreases, the GOSPA increases due to a lower bandwidth, resulting in target smearing that can more likely generate false target spawns. However, a slight increase in localization error can be seen at higher ρ_f, along with a decrease in detection rate.

For communication, a decrease of ρ_f increases the fraction of subcarriers exclusively dedicated to communication, leading to a higher downlink capacity. A capacity of 1.3 Gbit/s is ensured by fixing $\rho_\mathrm{f} = 0.2$ for a user at distance 55 m from its BS, with a localization error around 1.7 m. Increasing ρ_f to 0.6, the localization error drops to 1.3 m, with a reduction in network capacity of 23 %, i.e., 1 Gbit/s.

2.3.5 Impact of the Fraction of Time ρ_t

In Fig. 2.11, communication and sensing performance metrics are presented, varying the fraction of time devoted to JSC, ρ_t, with $\rho_\mathrm{p} = 0.4$ and $\rho_\mathrm{f} = 0.6$.

Additionally, as the fraction of time allocated for JSC, ρ_t, increases, there is a decrease in the downlink capacity. This decrease results from a lower fraction of time in which all communication resources are available, limiting the overall network capacity. With ρ_t fixed at 0.5, the GOSPA metric is around 1.3 m, while the downlink capacity for a user at distance 55 m from the related BS, is 1.2 Gbit/s. Halving ρ_t, the capacity increases to 1.4 Gbit/s, with a gain of 14 %, while the localization performance decreases, with an GOSPA distance around 1.4 m.

2.3.6 Impact of Number of Sensors N_s

Communication and sensing performance metrics, varying the number of BSs dedicated to sensing, are presented in Fig. 2.12, considering $\rho_\mathrm{p} = 0.4$, $\rho_\mathrm{f} = 0.6$ and $\rho_\mathrm{t} = 0.5$. In these evaluations, BSs performing both communication and

sensing are randomly selected from the set of available BSs.

From a sensing perspective, it is important to note the increase in the GOSPA error as the number of sensors N_s decreases. Moreover, the minimum number of sensors required to guarantee a localization error lower than 2 m is 3, and for a lower number of sensors, the error rapidly increases.

From the communication point of view, decreasing N_s slightly increases the downlink capacity. This increase is due to an increment of the communication resources that arise from BSs not selected to perform sensing.

2.4 Conclusion

In this Chapter, we presented a JSC framework for OFDM systems, leveraging the infrastructure of mobile radio networks to enable cooperative sensing among BSs by fusing soft maps acquired from BSs at a FC.

The overall networked system was tested by varying the fraction of resources allocated for sensing, including power (ρ_p), frequency (ρ_f), and time (ρ_t). Localization performance was assessed through the GOSPA metric, as well as the detection and false detection rate, while communication performance was evaluated through BS downlink sum rate.

Numerical results have shown that through the cooperation between three BSs, the localization of both extended and point-like targets is possible with an error of less than 2 m, while ensuring a downlink capacity larger than 1.3 Gbit/s for a UE at a distance of 55 m from the associated BS, considering $\rho_\mathrm{p} = 0.4$, $\rho_\mathrm{f} = 0.6$, and $\rho_\mathrm{t} = 0.5$.

Chapter 3

Design and Implementation of Bistatic JSC Systems

3.1 Introduction

In this chapter, we expand upon the performance analysis conducted previously, which focused on a cooperative monostatic configuration, to incorporate a bistatic JSC system. As highlighted in Chapter 1, a bistatic radar setup offers a practical solution to the SI problem encountered in monostatic configurations, which necessitate full-duplex capabilities–still considered a significant challenge. Following the approach from the previous chapter, we first present the sensing performance of a bistatic JSC MIMO system consisting of a Tx and Rx in Section 3.2, estimating both the DoA and bistatic range in Section 3.3. We compare two setups operating at sub-6 GHz and mmWave frequencies. Subsequently, we examine the RMSE of position estimates within the monitored area through heatmaps in Section 3.4, highlighting the impact of the blind zone on sensing. Finally, we investigate the sensing coverage limits of the bistatic system by varying the fraction of power allocated to sensing.

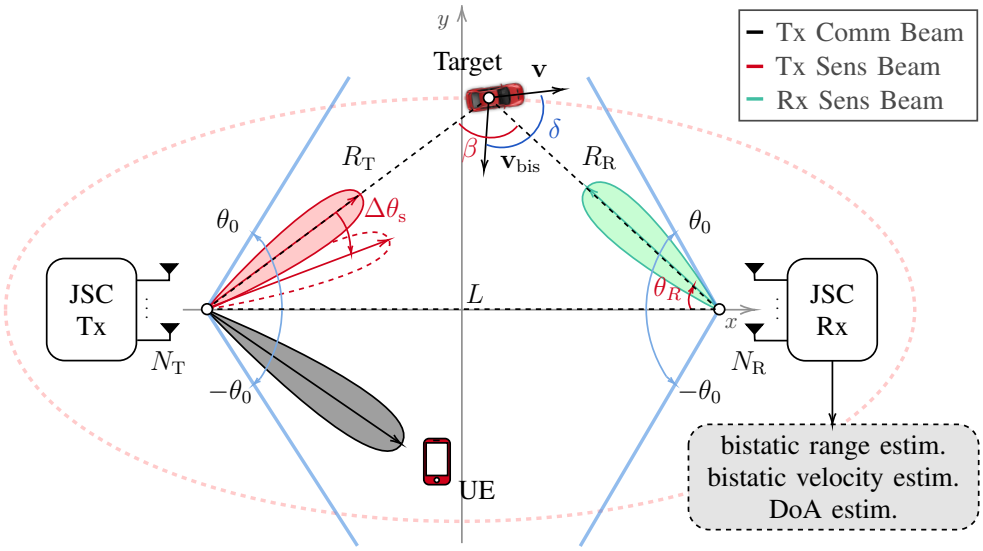

Figure 3.1: Illustration of the considered bistatic system for JSC. The Tx presents multi-beam capabilities to perform communication and sensing functionalities using the same time-frequency resources and sharing the transmitted power.

3.2 System Model

As depicted in Fig. 3.1, in this Chapter, a bistatic configuration for the JSC system is considered. In contrast with the monostatic setup studied in the previous Chapter, in which the Tx and the Rx are co-located, the bistatic one employs two nodes at different known locations, $\mathbf{p}_{\text{tx}} = (x_{\text{T}}, y_{\text{T}})$, and $\mathbf{p}_{\text{rx}} = (x_{\text{R}}, y_{\text{R}})$. In this way, it is possible to avoid the well-known self-interference problem affecting monostatic configurations [20].

Considering a bistatic sensing system based on downlink signals, the Tx can be a BS. Still, the Rx can be either another BS, a UE-like device, or a remote radio head (RRH) in a Cloud-RAN architecture. Alternatively, the system can deal with uplink signals as well. In this case, the signal transmitted by a UE is collected by a BS, after being reflected from targets [2, 74].

The JSC system proposed here consists of a Tx with N_{T} antenna elements and of a Rx with N_{R} antenna elements. The transmitted signal is used for both communication and sensing, exploiting the multibeam capabilities of the system, with a sensing beam that scans the environment while the communication beam points towards the UE [22, 75]. Without loss of generality, both the Tx and the Rx are equipped with ULAs, whose elements

are equally spaced of half-wavelength, i.e., $d = \lambda_c/2$ with $\lambda_c = c/f_c$, where f_c is the carrier frequency and c is the speed of light. The communication system transmits a 5G NR downlink signal with M OFDM symbols and K active subcarriers to a UE in the cell [47]. The baseband signal emitted by the nth antenna can be written as

$$s_n(t) = \sum_{m=0}^{M-1} \left(\sum_{k=0}^{K-1} \tilde{x}_{n,k}^{(m)} e^{j2\pi \frac{k}{T} t} \right) g(t - mT_s) \tag{3.1}$$

where $g(t)$ is the pulse shape, $\tilde{x}_{n,k}^{(m)}$ is the modulation symbol, belonging to a complex alphabet to be transmitted to the UE in the kth subcarrier and mth OFDM symbol, $\Delta f = 1/T$ is the subcarrier spacing, and T_s is the OFDM symbol duration including the cyclic prefix (CP).

3.2.1 Bistatic range and Doppler shift

In a bistatic configuration, the propagation time τ of the signal scattered by the target is related to the distance between the Tx and the target, R_T, and that between the target and the Rx, R_R, via the bistatic range $R_{bis} = R_T + R_R = \tau \cdot c$ [76]. After estimating R_{bis} via τ, the target can be located on an ellipse with a major axis equal to R_{bis} and foci at Tx and Rx positions, as depicted in Fig. 3.1. The Tx, Rx, and target form a triangle with base L (the distance between Tx and Rx) called the baseline; the angle β of the opposite vertex is named the bistatic angle.

If the DoA θ_R of the reflected echo at the Rx can be estimated, it is possible to determine the distance R_R as [76]

$$R_R = \frac{R_{bis}^2 - L^2}{2(R_{bis} + L \sin(\theta_R - \pi/2))} \tag{3.2}$$

and then, when considering a reference systems such as the one in Fig. 3.1, the target position can be found as $\mathbf{p}_{tg} = (x_R - R_R \cos\theta_R, y_R + R_R \sin\theta_R)$.

In addition to the target location, the bistatic velocity of the target can be inferred from the bistatic Doppler shift. The latter is proportional to the rate of change of R_{bis}. When Tx and Rx are stationary, and the target is

moving with velocity $\mathbf{v}$, the Doppler shift can be obtained as [76]

$$f_{\mathrm{D}} = \frac{1}{\lambda_{\mathrm{c}}} \frac{d}{dt} \left[R_{\mathrm{T}}(t) + R_{\mathrm{R}}(t) \right] = \frac{2v}{\lambda_{\mathrm{c}}} \cos\delta \cos\left(\beta/2\right) \tag{3.3}$$

where δ is the angle between the direction of the velocity and the bistatic bisector, and $v = |\mathbf{v}|$. While β can be easily determined by knowing L, R_{T}, R_{R}, and θ_{R}, the angle δ is unknown so only the bistatic velocity, $v_{\mathrm{bis}} = |\mathbf{v}_{\mathrm{bis}}| = v\cos\delta$, can be estimated by the system.

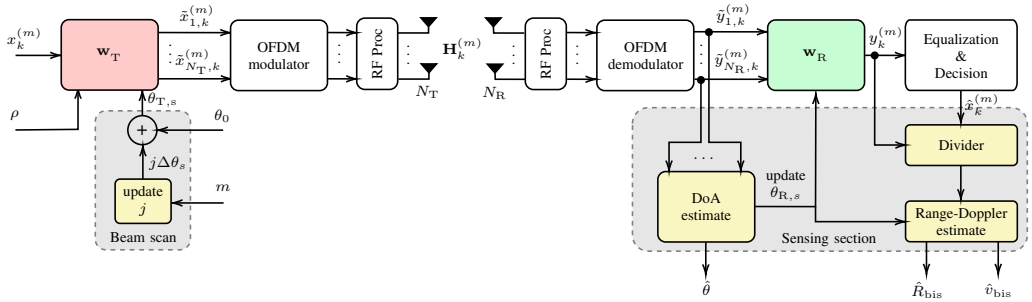

Figure 3.2: Block diagram of the bistatic 5G NR-based JSC system with multibeam capability.

3.2.2 Maximum Bistatic Range and Blind Zone

To avoid ISI and guarantee unambiguous range detection, the guard time t_{G} of the OFDM needs to be larger than the propagation delay of the scattered signal. In a bistatic configuration, this leads to a maximum detectable bistatic range $R_{\mathrm{bis}} \leq t_{\mathrm{G}}c + L$, which results in a maximum ellipse whose minor axis is $A_{\max} = \sqrt{(t_{\mathrm{G}}c + L)^2 - L^2}$.

A critical issue deserving attention in bistatic setups is the blind zone, i.e., a region enclosing the baseline where target detection becomes problematic [37]. A target sufficiently close to the baseline is hard to detect because of the time resolution, which compromises the separation of the direct Tx-Rx path from the Tx-target-Rx one. Given the resolution of the bistatic range estimate, $\Delta r = c/(K\Delta f)$, we define $L + \Delta r$ as the minimum bistatic range below which the Rx cannot resolve the reflected path from the direct one. So, we must have $R_{\mathrm{bis}} \geq L + \Delta r$. The ellipse with major axis $L + \Delta r$ is called the minimum ellipse, whose minor axis is $A_{\min} = \sqrt{(L + \Delta r)^2 - L^2}$.

3.2.3 Transmitted and Received Signal

Now, let us detail the whole system behavior by looking at the block diagram in Fig. 3.2. First, at the Tx, the complex modulation symbols $x_k^{(m)}$ are mapped at each antenna through a digital precoder $\mathbf{w}_\mathrm{T} \in \mathbb{C}^{N_\mathrm{T}\times 1}$, to obtain the transmitted vector $\tilde{\mathbf{x}}_k^{(m)} \in \mathbb{C}^{N_\mathrm{T}\times 1}$, defined as $\tilde{\mathbf{x}}_k^{(m)} = \mathbf{w}_\mathrm{T} x_k^{(m)}$. In particular, the idea is to split the available transmitted power of the OFDM signal between communication and sensing, using a beamformer (BF) vector [22,75]

$$\mathbf{w}_\mathrm{T} = \sqrt{\rho}\,\mathbf{w}_{\mathrm{T,s}} + \sqrt{1-\rho}\,\mathbf{w}_{\mathrm{T,c}} \tag{3.4}$$

where $\mathbf{w}_{\mathrm{T,c}}$ is the BF vector for communication, $\mathbf{w}_{\mathrm{T,s}}$ is the BF vector for sensing, with [47]

$$\mathbf{w}_{\mathrm{T,c}} = \sqrt{P_\mathrm{avg}}\tilde{\mathbf{w}}_\mathrm{T}(\theta_{\mathrm{T,c}}) \quad \mathbf{w}_{\mathrm{T,s}} = \sqrt{P_\mathrm{avg}}\tilde{\mathbf{w}}_\mathrm{T}(\theta_{\mathrm{T,s}}) \tag{3.5}$$

and $\rho \in [0,1]$ controls the partition of power between the two beams. In (3.5), beamforming is performed using the weight vectors $\tilde{\mathbf{w}}_\mathrm{T}(\theta_{\mathrm{T,c}}) = \mathbf{a}_\mathrm{T}^{\mathsf{c}}(\theta_{\mathrm{T,c}}) \odot \mathbf{c}/\sqrt{N_\mathrm{T}}$ and $\tilde{\mathbf{w}}_\mathrm{T}(\theta_{\mathrm{T,s}}) = \mathbf{a}_\mathrm{T}^{\mathsf{c}}(\theta_{\mathrm{T,s}}) \odot \mathbf{c}/\sqrt{N_\mathrm{T}}$, where $\mathbf{a}_\mathrm{T}(\theta_{\mathrm{T,c}}) \in \mathbb{C}^{N_\mathrm{T}\times 1}$ and $\mathbf{a}_\mathrm{T}(\theta_{\mathrm{T,s}}) \in \mathbb{C}^{N_\mathrm{T}\times 1}$ are the steering vectors for communication and sensing, respectively, and $P_\mathrm{avg} = P_\mathrm{T}/K$ is the average power allocated per subcarrier, being P_T the total transmit power [77]. Considering that beam steering often results in relatively high sidelobes, which are undesirable in sensing applications, we applied a windowing function by element-wise multiplying with the window weight vector $\mathbf{c}$ such that $\|\tilde{\mathbf{w}}_\mathrm{T}\|_2^2 = 1$.

For a ULA with N_a antennas with half-wavelength separation, the array response vector for a DoA or direction of departure (DoD) ϕ is given by $\mathbf{a}(\phi) = \left[e^{-j\pi\frac{N_\mathrm{a}-1}{2}\sin\phi}, \ldots, e^{j\pi\frac{N_\mathrm{a}-1}{2}\sin\phi}\right]^T$.

As it is shown in Fig. 3.2, in the considered JSC system, the sensing direction $\theta_{\mathrm{T,s}}$ is sequentially changed to illuminate the entire surrounding environment, according to

$$\theta_{\mathrm{T,s}} = \theta_0 + j\,\Delta\theta_\mathrm{s} \qquad j = 0, \ldots, N_\mathrm{dir} - 1 \tag{3.6}$$

where $\Delta\theta_\mathrm{s}$ is the angle step and N_dir is the number of directions to scan the

aperture $[-\theta_0, \theta_0]$. Given M OFDM symbols contained in a 5G NR frame (with a duration of $T_\mathrm{f} = 10\,\mathrm{ms}$), $M_\mathrm{s} < M$ symbols are acquired by the Rx in each sensing direction. Hence, the update of j depends on the symbol index m, and the number of frames and time required to complete a scan become $N_\mathrm{f} = \left\lceil \frac{M_\mathrm{s} N_\mathrm{dir}}{M} \right\rceil$ and $T_\mathrm{scan} = T_\mathrm{f} N_\mathrm{f}$.

For each $\theta_{\mathrm{T,s}}$, the vector $\tilde{\mathbf{y}}_k^{(m)} \in \mathbb{C}^{N_\mathrm{R} \times 1}$ of the received symbols at each antenna after OFDM demodulation, is given by

$$\tilde{\mathbf{y}}_k^{(m)} = \mathbf{H}_k^{(m)} \tilde{\mathbf{x}}_k^{(m)} + \tilde{\mathbf{n}}_k \tag{3.7}$$

where $\mathbf{H}_k^{(m)} \in \mathbb{C}^{N_\mathrm{R} \times N_\mathrm{T}}$ is the channel matrix, and $\tilde{\mathbf{n}}_k \sim \mathcal{CN}(\mathbf{0}, \sigma_\mathrm{N}^2 \mathbf{I}_{N_\mathrm{R}})$. When Q point targets are present in the monitored area, the channel matrix between the transmitting and receiving antennas can be represented as

$$\mathbf{H}_k^{(m)} = \sum_{q=1}^{Q} \underbrace{\alpha_q e^{j2\pi m T_\mathrm{s} f_{\mathrm{D},q}} e^{-j2\pi k \Delta f \tau_q}}_{\triangleq \beta_q} \mathbf{a}_\mathrm{R}(\theta_{\mathrm{r},q}) \mathbf{a}_\mathrm{T}^\mathsf{T}(\theta_{\mathrm{t},q}) \tag{3.8}$$

where $\boldsymbol{\theta}_\mathrm{R} = [\theta_{\mathrm{r},1}, \theta_{\mathrm{r},2}, \ldots, \theta_{\mathrm{r},Q}]$ are the DoAs, $\boldsymbol{\theta}_\mathrm{T} = [\theta_{\mathrm{t},1}, \theta_{\mathrm{t},2}, \ldots, \theta_{\mathrm{t},Q}]$ are the DoDs of the targets, and $\alpha_q = |\alpha_q| e^{j\phi_q}$ is the complex amplitude which includes phase shift and attenuation along the qth propagation path.

On the receiving side shown in Fig. 3.2, starting from (3.7), spatial combining is performed through the receiving BF vector $\mathbf{w}_\mathrm{R}$ to obtain the received symbol, $y_k^{(m)} = \mathbf{w}_\mathrm{R}^\mathsf{T} \tilde{\mathbf{y}}_k^{(m)}$. In particular, target detection and localization are performed in two steps: 1) the vector $\mathbf{w}_\mathrm{R}$ is initialized to have all elements equal to one to search for targets in the area through DoA estimation, $\widehat{\theta}_{\mathrm{r},q}$; 2) once DoAs are estimated, $\mathbf{w}_\mathrm{R}$ is updated to point the receiving beam in the direction where the target q is likely to be present, i.e., $\mathbf{w}_\mathrm{R} = \mathbf{a}_\mathrm{R}^c(\theta_{\mathrm{R},s}) \odot \mathbf{c}/\sqrt{N_\mathrm{R}}$, with $\theta_{\mathrm{R},s} = \widehat{\theta}_{\mathrm{r},q}$. Then, in each sensing direction, the Rx needs to perform channel equalization and decision for detecting the transmitted symbols, $\hat{x}_k^{(m)}$. As it will be explained in Section 3.3.2, to estimate bistatic range and Doppler shift, it is necessary to know and remove the transmitted symbol $x_k^{(m)}$ through the *divider* block.

3.2.4 Received Power and Cassini Ovals

In the bistatic radar configuration, the power reflected by a point target q with a RCS equal to $\sigma_{\mathrm{RCS},q}$, illuminated by the Tx sensing beam and collected at the Rx antenna element in free-space propagation conditions, is given by

$$P_{\mathrm{R},q}^{\mathrm{bis}} = \frac{\rho P_{\mathrm{avg}} G_{\mathrm{T}}^{\mathrm{a}} G_{\mathrm{R}} c^2 \sigma_{\mathrm{RCS},q}}{(4\pi)^3 f_{\mathrm{c}}^2 (R_{\mathrm{T},q} R_{\mathrm{R},q})^2} \tag{3.9}$$

where G_{R} is the receiving antenna gain of the single antenna element, while $R_{\mathrm{T},q}$ and $R_{\mathrm{R},q}$ are, respectively, the Tx-target and Rx-target distances for the qth target.

As it can be seen in (3.9), the received power scattered by the target is inversely proportional to $(R_{\mathrm{T}} R_{\mathrm{R}})^2$. The locus of points such that the product of their distances $R_{\mathrm{T}} R_{\mathrm{R}}$ from two foci is a constant is named Cassini oval [37, 76]. The shape of a Cassini oval depends on the ratio between $\sqrt{R_{\mathrm{T}} R_{\mathrm{R}}}$ and $L/2$. In particular, the curve consists of two loops around the foci when $\sqrt{R_{\mathrm{T}} R_{\mathrm{R}}} < L/2$, it assumes a lemniscate shape when $\sqrt{R_{\mathrm{T}} R_{\mathrm{R}}} = L/2$, and it is a single loop with an oval shape when $\sqrt{R_{\mathrm{T}} R_{\mathrm{R}}} > L/2$.

Starting from (3.9), the SNR at the single receiving antenna element related to the qth target can be defined as

$$\mathrm{SNR}_q = \frac{P_{\mathrm{R},q}^{\mathrm{bis}}}{N_0 K \Delta f} \tag{3.10}$$

where N_0 is the one-sided noise PSD at each antenna element. By normalizing the received symbols after the fast Fourier transform (FFT) in the OFDM Rx as $\mathbb{E}\{|\tilde{y}_{n,k}^{(m)}|^2\} = 1$, (3.10) reduces to $\mathrm{SNR}_q = 1/\sigma_{\mathrm{N}}^2$. Iso-SNR contours are thus Cassini ovals.

3.3 Estimation of Target Parameters and Detection

This section introduces the techniques used for estimating DoA, bistatic range, and bistatic velocity. In particular, for the DoA two different methods have been compared, i.e., multiple signal classification (MUSIC) and root-

MUSIC, while for bistatic range and speed estimation a periodogram-based frequency estimation approach has been used, as in [18, 75, 78].

3.3.1 Estimation of the Number of Targets and DoAs

DoAs estimation requires, at first, the evaluation of the number of targets or sources $\widehat{Q}$, which can be estimated by model order selection based on information-theoretic criteria [79, 80]. For the initial estimate, the covariance matrix of the received vector (3.7) is calculated as $\mathbf{R} = \mathbb{E}\{\tilde{\mathbf{y}}_k^{(m)}\tilde{\mathbf{y}}_k^{(m)\dagger}\} \in \mathbb{C}^{N_\mathrm{R}\times N_\mathrm{R}}$. In fact, since the noise is zero mean and independent of the target echoes, it follows that the $N_\mathrm{R} - Q$ smallest eigenvalues of $\mathbf{R}$ are all equal to the noise power σ_N^2 and the corresponding eigenvectors identify the noise subspace.[1] However, since the covariance matrix is not known a priori, the sample covariance matrix (SCM) can be used instead [7]. The SCM of the received symbols vector (3.7) is computed in each Tx sensing direction as follows [75]

$$\widehat{\mathbf{R}} = \frac{1}{KM_\mathrm{a}} \sum_{m=0}^{M_\mathrm{a}-1} \sum_{k=0}^{K-1} \tilde{\mathbf{y}}_k^{(m)}\tilde{\mathbf{y}}_k^{(m)\dagger} = \mathbf{U}\mathbf{\Lambda}\mathbf{U}^\dagger \tag{3.11}$$

where $M_\mathrm{a} \subset M_\mathrm{s}$ is the number of OFDM symbols employed in each sensing direction to estimate the DoAs, the columns of $\mathbf{U} \in \mathbb{C}^{N_\mathrm{R}\times N_\mathrm{R}}$ are the eigenvectors of $\widehat{\mathbf{R}}$ and $\mathbf{\Lambda} = \mathrm{diag}(\lambda_1, \ldots, \lambda_{N_\mathrm{R}})$ is a diagonal matrix with eigenvalues sorted in descending order, i.e., $\lambda_1 \geq \lambda_2 \geq \cdots \geq \lambda_{N_\mathrm{R}}$. Using the Akaike information criterion (AIC) criterion, the estimated number of targets (considering that we are illuminating only targets within the sensing beam in the jth direction) is

$$\widehat{L} = \underset{s\in\{0,\ldots,N_\mathrm{R}-1\}}{\arg\min} \{\mathrm{AIC}(s)\} \tag{3.12}$$

with

$$\begin{aligned}\mathrm{AIC}(s) = &-2\ln\left(\frac{\prod_{i=s+1}^{N_\mathrm{R}} \lambda_i^{1/(N_\mathrm{R}-s)}}{\frac{1}{N_\mathrm{R}-s}\sum_{i=s+1}^{N_\mathrm{R}}\lambda_i}\right)^{(N_\mathrm{R}-s)KM_\mathrm{s}} \\ &+ 2s(2N_\mathrm{R}-s).\end{aligned} \tag{3.13}$$

[1] As required by the super-resolution algorithms specified later, we consider $L < N_\mathrm{R}$, i.e., the number of targets is less than the number of sensing array elements.

Then, starting from the noise subspace, the vector of DoAs, $\widehat{\boldsymbol{\theta}}_{\mathrm{R}}$, is estimated, either through MUSIC or root-MUSIC algorithms. [81–83].

3.3.2 Range-Doppler Estimation and Localization

After estimating the DoA, denoted as $\widehat{\theta}_{\mathrm{r},q}$, beamforming is applied at the receiver as described in Section 3.2.3 to spatially filter the received signal. Subsequently, the remaining $M_{\mathrm{s}} - M_{\mathrm{a}}$ OFDM symbols are used to obtain the beamformed signal $y_m^{(m)}$, which is then processed to estimate the bistatic range and velocity of the target q through range-Doppler analysis, following the approach in [75]. Then, starting from the received symbols $y_k^{(m)}$, a division is performed to remove the unwanted data symbols, i.e., $g_k^{(m)} = y_k^{(m)}/x_k^{(m)}$ [18].[2] Next, as $g_k^{(m)}$ contains two complex sinusoids for each target, embedded in β_q of (3.8), whose frequencies are related to $f_{\mathrm{D},q}$ and τ_q, a periodogram can be computed, as [18, 20, 78]

$$\mathcal{P}(l,p) = \left| \sum_{k=0}^{K_{\mathrm{p}}-1} \left(\sum_{m=0}^{M_{\mathrm{p}}-1} g_k^{(m)} e^{-j2\pi \frac{mp}{M_{\mathrm{p}}}} \right) e^{j2\pi \frac{kl}{K_{\mathrm{p}}}} \right|^2 \tag{3.14}$$

with $l = 0, \ldots, K_{\mathrm{p}} - 1$ and $p = 0, \ldots, M_{\mathrm{p}} - 1$. In this thesis, $K_{\mathrm{p}} > K$ and $M_{\mathrm{p}} > (M_{\mathrm{s}} - M_{\mathrm{a}})$ are calculated as the next power of two of K and $F_{\mathrm{p}} \cdot (M_{\mathrm{s}} - M_{\mathrm{a}})$, respectively, where F_{p} is the zero-padding factor to improve speed estimation resolution. The periodogram (3.14) represents the range-Doppler map from which, after performing target detection by a hypothesis test as in [75], bistatic range and velocity of the target q can be extracted. In particular, at first, the location of the peak in the periodogram needs to be found, as $(\widehat{l}, \widehat{p}) = \arg\max_{(l,p)}\{\mathcal{P}(l,p)\}$. Then, the bistatic range can be evaluated as

$$\widehat{R}_{\mathrm{bis},q} = \frac{\hat{l}\, c}{\Delta f K_{\mathrm{p}}}. \tag{3.15}$$

[2] Note that, in this thesis, symbols $x_k^{(m)}$ are considered known at the Rx; this may happen, e.g., because of correct demodulation or because the sequence of symbols emitted during sensing is predefined. Moreover, perfect synchronization between Tx and Rx is assumed.

Table 3.1: JSC system parameters

5G specification →	NR 100	NR 400
f_c [GHz]	3.5	28
Δf [kHz]	30	120
Active subcarriers K	3276	3168
OFDM symbols per frame M	280	1120
Number of antennas N_T	10	10 50
Number of antennas N_R	10	10 50

Once $\widehat{R}_{\mathrm{bis},q}$ and $\widehat{\theta}_{\mathrm{r},q}$ have been estimated, it is possible to estimate the distance between the Rx and the target, $\widehat{R}_{\mathrm{R},q}$, according to (3.2). Then, position and bistatic velocity of the target q are determined as stated in Section 3.2.1. In particular, the magnitude of the bistatic velocity is given by

$$\widehat{v}_\mathrm{bis} = \frac{\widehat{p}c}{2f_\mathrm{c}T_\mathrm{s}M_\mathrm{p}\cos\left(\beta/2\right)}. \tag{3.16}$$

3.4 System Level Analysis

Numerical simulations were carried out to assess the performance of the bistatic JSC system presented. In particular, as the main purpose of this thesis is to study the system behavior in terms of RMSE of position, angle, and bistatic range estimation, a single target scenario is considered, i.e., $Q = 1$, with the sensing beam at the Tx aligned with the target, i.e., $\theta_{\mathrm{T,s}} = \theta_{\mathrm{t},1}$. The parameter θ_0 is set equal to 60° to have a total angular opening of 120°, both at the Tx and Rx. Table 3.1 shows the 5G NR parameters employed for the simulations. For each sensing direction at the Tx, K active subcarriers and $M_\mathrm{s} = 112$ OFDM symbols are considered. A QPSK modulation alphabet is considered for each subcarrier.

As already stated in Section 3.2.3, at the Rx, the initially performed operation is DoA estimation with the first $M_\mathrm{a} = 30$ OFDM symbols acquired. Then, the receiving BF vector, $\mathbf{w}_\mathrm{R}$, is updated accordingly and the periodogram is performed with the remaining $M_\mathrm{s} - M_\mathrm{a} = 82$ OFDM symbols, with $F_\mathrm{p} = 10$. For DoA estimation with MUSIC, the pseudo-spectrum function is computed only in the range $[-\theta_0, \theta_0]$, to reduce the processing

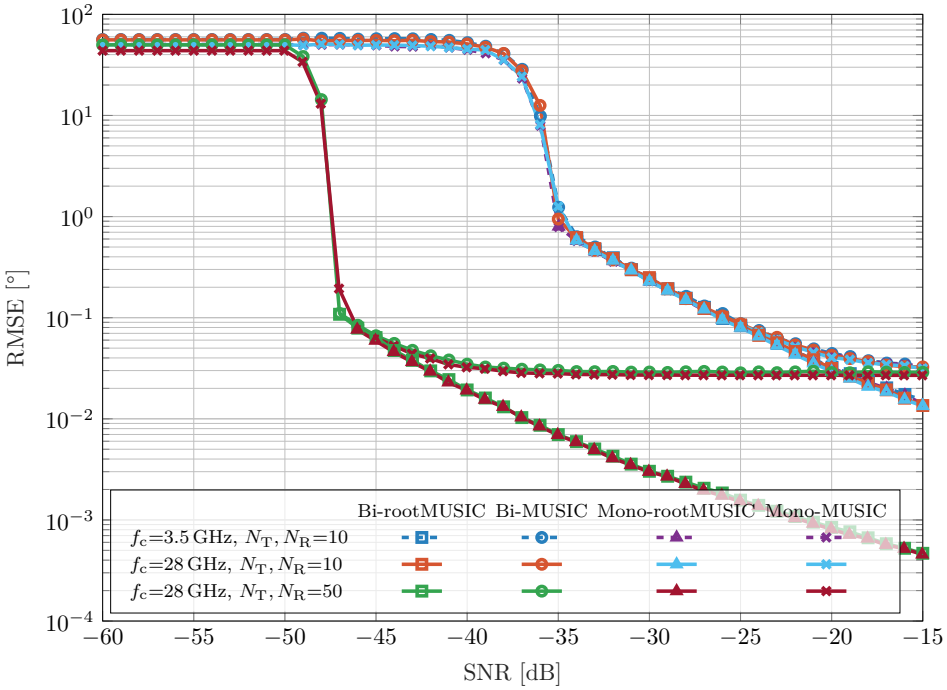

Figure 3.3: Sensing performance of the JSC system as a function of the SNR for DoA, comparing a different number of antennas and 5G numerologies, as well as DoA estimation techniques. Results are shown for both monostatic and bistatic configurations to highlight the performance similarities between the two setups.

burden.

Two types of simulations were performed: 1) RMSE of DoA and R_{bis} estimate as a function of the SNR. In this case, the received symbols were normalized to unit power and the noise variance is defined as $\sigma_{\text{N}}^2 = 1/\text{SNR}$, as mentioned in Section 3.2.4; 2) system coverage analysis performed computing the RMSE of the position estimate, with the SNR as a function of target position itself and of the portion of transmitted power reserved to sensing, according to (3.10). In this case, the following system parameters were considered: the EIRP is set to $P_{\text{T}} = 30\,\text{dBm}$; $G_{\text{R}} = 1$; the noise PSD is $N_0 = k_{\text{B}} T_0 F$ where $k_{\text{B}} = 1.38 \cdot 10^{-23}\,\text{JK}^{-1}$ is the Boltzmann constant, $T_0 = 290\,\text{K}$ is the reference temperature, and $F = 10\,\text{dB}$ is the receiver noise figure; the target RCS is $\sigma_{\text{RCS}} = 1\,\text{m}^2$.

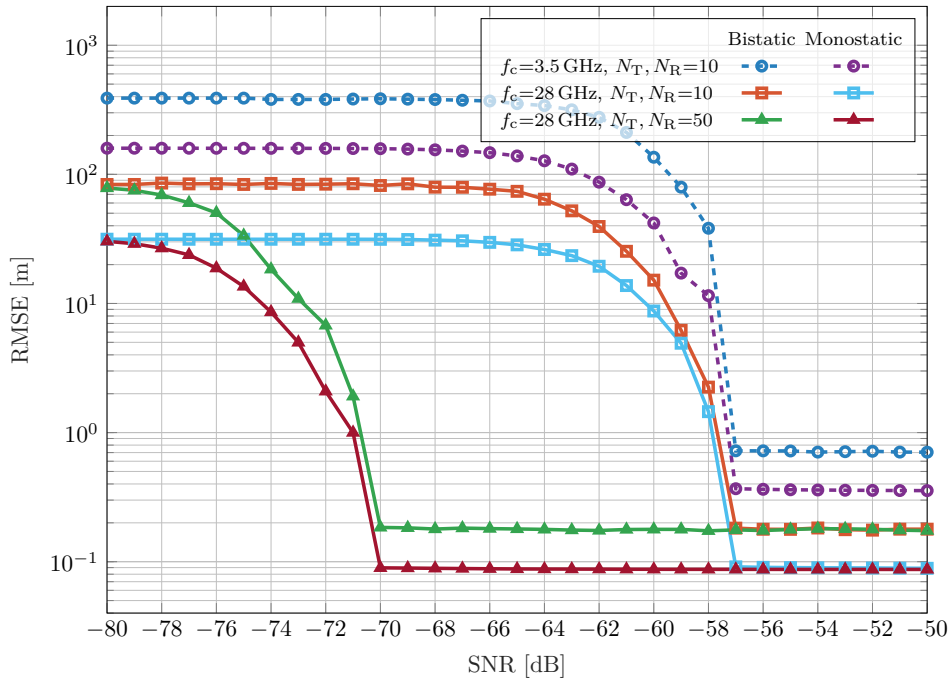

Figure 3.4: Sensing performance of the JSC system as a function of the SNR for range estimate, comparing a different number of antennas and 5G numerologies. Results are shown for both monostatic and bistatic configurations to highlight the performance similarities between the two setups.

3.4.1 RMSE vs SNR

In this set of simulations, the position of the target is varied randomly, from one realization to another, within a diamond-shaped area identified by θ_0, as illustrated in Fig. 3.1. As expected, inside the blind zone, target detection is problematic, and the error is affected primarily by the bistatic geometry configuration. For this reason, targets are not generated inside the minimum ellipse, as this zone is not considered a system operation zone. In each realization, the target velocity is varied randomly, with a uniform distribution from $-20\,\mathrm{m/s}$ to $20\,\mathrm{m/s}$.

Fig. 3.3 and Fig. 3.4 show the RMSE as a function of the SNR for DoA and bistatic range estimate. In the former, MUSIC and root-MUSIC are compared. Since the target parameters estimate strongly depends on the beamforming direction at the Rx, i.e., $\theta_{\mathrm{R,s}}$, to separately study the two errors, the curve in Fig. 3.4 is obtained using the true value of the target DoA

as $\theta_{\mathrm{R,s}}$ to update the receiving BF vector. As it can be noticed, RMSE of the DoA estimate increases for higher values of the SNR than those for which the estimate of R_{bis} degrades. This behavior can be explained considering that R_{bis} estimation process is subject to a double processing gain, one resulting from the periodogram calculation, equal to $10\log_{10}(K \cdot (M_{\mathrm{s}} - M_{\mathrm{a}}))\,\mathrm{dB}$ [18], and the other from the beamforming gain, equal to $10\log_{10}(N_{\mathrm{T}} \cdot N_{\mathrm{R}})\,\mathrm{dB}$. In contrast, the DoA estimation is not subject to any processing gain, and the RMSE of angle estimation starts to increase at much higher SNR values, depending on the number of antennas. Moreover, root-MUSIC strictly depends on the number of estimated targets, for which the AIC is used [79], as well as the noise subspace. At lower SNR, when the number of targets estimation becomes difficult, the DoA estimate process fails, and targets can be missed. This defines a lower bound, $\mathrm{SNR}_{\mathrm{min}}$, for angle estimation and position estimation, as a consequence. MUSIC is still able to detect targets for lower SNR as it depends solely on the noise subspace, but angle RMSE increases rapidly.

To enable a fair comparison between bistatic and monostatic configurations, a second set of simulations is conducted for the monostatic case. In this scenario, a single point-like target is randomly generated within a uniformly distributed range of $[20, 80]\,\mathrm{m}$ and an angular span of $[-60°, 60°]$. The same DoA and range estimation procedures are applied to evaluate the performance of both configurations. The results show that, in terms of DoA estimation, the monostatic and bistatic systems perform comparably. This is expected, as the estimation methods employed—MUSIC and root-MUSIC—rely on the structure of the noise subspace and not on the specific geometric configuration of the system. However, for range estimation, differences emerge. Although both systems exhibit similar asymptotic behavior in terms of the RMSE onset with increasing SNR, which converges to $\sqrt{\Delta r^2/12}$, the asymptotic RMSE floor differs between the two. Specifically, the monostatic configuration achieves a lower asymptotic RMSE. This is due to the different definitions of range resolution in the two cases. In the monostatic system, the range resolution is given by $\Delta r = c/(2K\Delta f)$, which reflects the round-trip propagation of the signal. Conversely, in the bistatic configuration, the range resolution is defined as $\Delta r = c/(K\Delta f)$,

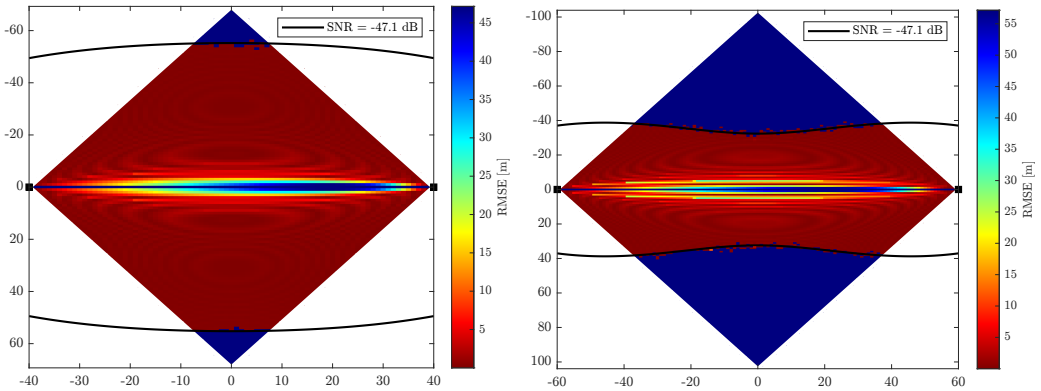

(a) *Baseline* $L = 80$ (b) *Baseline* $L = 120$

Figure 3.5: Sensing coverage area of the JSC bistatic system operating at $f_c = 28\,\text{GHz}$ with $N_T = N_R = 50$. In particular, in (a) and (b) the heatmaps of the position RMSE when $f_c = 28\,\text{GHz}$ and $\rho = 0.1$ are presented, with the Cassini Oval at SNR $= -47.1\,\text{dB}$.

since the total path length includes both Tx-to-target R_T and target-to-Rx R_R distances. As a result, the monostatic system exhibits inherently finer resolution, which translates into more accurate range estimates in high-SNR regimes.

3.4.2 Coverage Analysis

For the sensing coverage area analysis, the spatial region of interest is discretized into pixels of $1\,\text{m}^2$ area, and the error on the position estimate in each pixel is calculated. Also in this case, the speed of the target is varied randomly with uniform distribution from -20 to $20\,\text{m/s}$. A direct visualization of the behavior of the position RMSE in each point inside the considered area is represented through heatmaps, shown in Fig. 3.5, evaluated for two different values of L with a fraction of power for sensing given by $\rho = 0.1$. In particular, a 5G NR signal with $\Delta f = 120\,\text{kHz}$, $f_c = 28\,\text{GHz}$, and a number of antennas $N_T = N_R = 50$ are used. For DoA estimation root-MUSIC is applied. In the scenario of Fig. 3.5a, Tx and Rx are located at $(-40, 0)\,\text{m}$ and $(40, 0)\,\text{m}$, respectively, with $L = 80\,\text{m}$. In this case, $A_{\min} = 9.9\,\text{m}$ and $A_{\max} = 242.8\,\text{m}$. Likewise, in Fig. 3.5b a baseline $L = 120\,\text{m}$ is considered, with Tx and Rx located at $(-60, 0)\,\text{m}$ and $(60, 0)\,\text{m}$, having $A_{\min} = 12.1\,\text{m}$ and $A_{\max} = 270.2\,\text{m}$. These results highlight how the fraction of covered

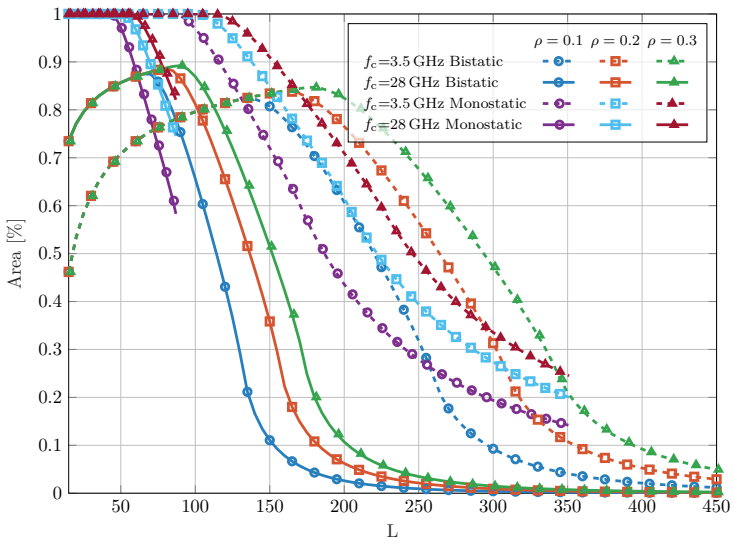

Figure 3.6: Sensing coverage area of the JSC system operating at $f_c = 28\,\text{GHz}$ with $N_T = N_R = 50$ and $f_c = 3.5\,\text{GHz}$ with $N_T = N_R = 10$. The fraction of area covered for different values of power reserved for sensing is shown as a function of the baseline L for the bistatic configuration. For the monostatic case, the x-axis represents the distance from the BS rather than an inter-node baseline.

area increases as the baseline decreases for fixed sensing power. However, the blind zone area does not decrease proportionally to the overall area when decreasing L, and thus, for shorter baselines, the fraction of the covered area diminishes. This behavior is better emphasized in Fig. 3.6, where the percentage of covered areas as a function of the baseline L, for different values of ρ, is shown.

In the bistatic configuration, the sensing area is defined as a diamond-shaped region, as previously illustrated in Fig. 3.1. The coverage percentage is computed as the portion of this region for which the system can estimate the target's position with acceptable accuracy. More precisely, the percentage of coverage area is calculated as the following. Recalling Fig. 3.3, the coverage area is calculated through the maximum Cassini oval, associated with the minimum SNR, SNR_{min}, for which the system can estimate the DoA with good accuracy. For example, for the parameters specified above and root-MUSIC estimation performance, $\text{SNR}_{\text{min}} = -47.1\,\text{dB}$ at $f_c = 28\,\text{GHz}$, whereas $\text{SNR}_{\text{min}} = -35.1\,\text{dB}$ at $f_c = 3.5\,\text{GHz}$. The blind zone region is not

considered in the sensing system covered area since in that zone, target detection becomes problematic with very large position RMSE, as shown in Fig. 3.5a and Fig. 3.5b. Hence, the coverage area is the area of the diamond-shaped region inside the Cassini oval, corresponding to $\mathrm{SNR}_{\min}$, minus the area of the blind zone; such area is then normalized to the diamond-shape area to provide a measure of coverage effectiveness of the sensing system.

In the monostatic case, the definition of the coverage area differs. Here, the sensing region is constrained by the field-of-view (FoV) of the BS, which is assumed to be 120°. The entire area within this FoV is divided into $1\,\mathrm{m}^2$ pixels, and coverage is again assessed based on whether the SNR in each pixel exceeds the corresponding $\mathrm{SNR}_{\min}$ threshold for root-MUSIC-based DoA estimation. Unlike the bistatic case, there is no blind zone at close distances in the monostatic setup, enabling full coverage at short ranges. Nevertheless, coverage is ultimately bounded by the unambiguous range limit imposed by the system parameters.

In both configurations, an additional constraint is enforced to avoid ISI and ensure range unambiguity. For the bistatic case, sensing is limited to pixels where the bistatic range satisfies $R_{\mathrm{bis}} \leq R_{\mathrm{bis,max}} = t_{\mathrm{G}}c + L$. For the monostatic system, the constraint simplifies to $R \leq R_{\max} = t_{\mathrm{G}}c$, due to the round-trip nature of the propagation. As a result, in the monostatic configuration, the coverage saturates at shorter ranges, beyond which sensing becomes unreliable and is thus excluded. Conversely, bistatic systems can extend $R_{\mathrm{bis,max}}$ by increasing the baseline L, thereby enabling coverage of more distant regions. This advantage is particularly significant at mmWave frequencies, where coverage gains due to extended bistatic baselines become more pronounced.

While sensing coverage improves with increasing ρ, the available power for communication decreases, leading to a corresponding reduction in communication SNR and theoretical channel capacity. Specifically, assuming that the communication SNR, $\mathrm{SNR}^{\mathrm{c}}$, scales proportionally with the available transmit power $(1-\rho)$, the theoretical channel capacity for each configuration can be approximated using Shannon's formula: $C = B\log_2(1 + (1-\rho)\,\mathrm{SNR}^{\mathrm{c}})$. As ρ increases to favor sensing, the communication capacity correspondingly decreases, revealing an intrinsic trade-off between sensing coverage and com-

munication performance. For instance, assuming a total communication SNR of 10 dB when $\rho = 0$, and a baseline of 100 m, the percentage of area covered increases from 0.65% with $\rho = 0.1$ to 0.87% with $\rho = 0.3$. Under these conditions, considering a bandwidth of B = 400 MHz at a carrier frequency $f_c = 28$ GHz with $N_T = N_R = 50$, the corresponding theoretical capacity decreases from approximately 1.26 Gbps to about 1.14 Gbps.

3.5 Conclusion

In this Chapter, the performance of a 5G NR system that acts as a bistatic sensor to estimate the position of a target via bistatic range and DoA has been studied. Analyzing the RMSE, we found that good accuracy can be achieved in LOS, both at mmWave and sub-6 GHz frequencies, and that: *i*) DoA estimation is the primary source of degradation of the system localization performance; *ii*) a fraction of coverage area greater or equal to 70% can be reached for a baseline $L \leq 100$ m, even at mmWave when ρ is equal to 0.3; *iii*) the blind zone may have a major impact on detection coverage, especially for narrow bandwidth numerologies. Furthermore, the proposed bistatic configuration has been compared against its monostatic counterpart, demonstrating an improved sensing coverage, thereby confirming the potential of bistatic setups to enhance spatial awareness in distributed JSC systems.

Chapter 4

Performance Analysis of a Multistatic MISO JSC System

4.1 Introduction

In this Chapter, we extend the analysis from Chapter 3 by exploring the performance of a multistatic MISO system based on 5G NR signals and its sensing capabilities. We investigate the impact of the fraction of power allocated to sensing and its effect on optimizing the sensing/communication trade-off. In Section 4.3 we also propose two data fusion approaches for position estimation, comparing a LS algorithm with a soft map generation technique. Additionally, we analyze the RMSE of position estimates, emphasizing the advantages of a multistatic network over a bistatic configuration, particularly in addressing the issue of "blind zones" in Section 4.4.

4.2 System Model

We consider a JSC system that acts as a multistatic radar network, as depicted in Fig. 4.1. Unlike the monostatic configuration studied in [46, 75], in which the Tx and the Rx are co-located, and the bistatic setup analyzed in [84], the multistatic system presented here consists of one Tx and multiple Rxs located at different known positions, which form several bistatic pairs. In the considered scenario, we perform sensing exploiting the downlink com-

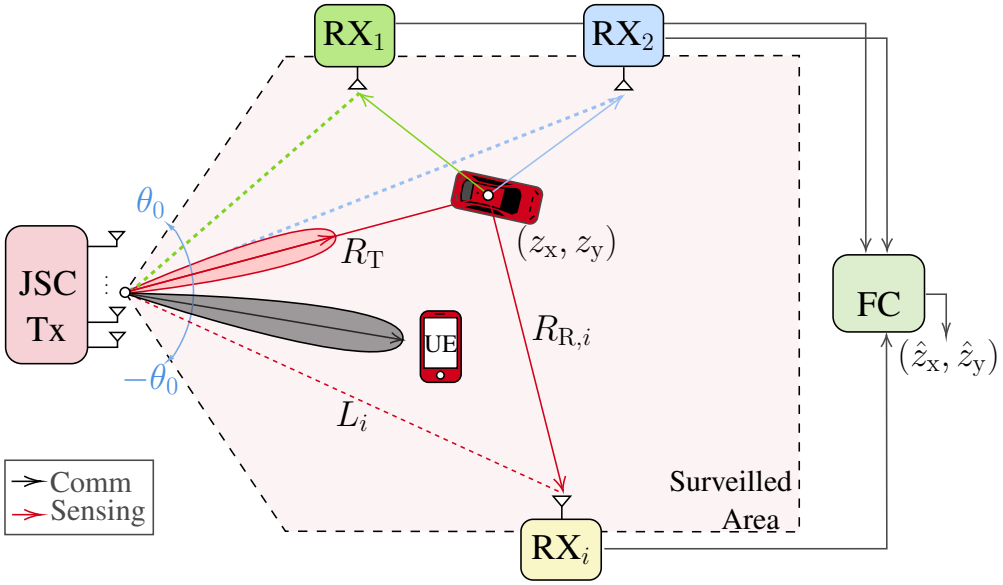

Figure 4.1: Considered multistatic JSC system with one multiple antenna transmitter and several single antenna receivers (or sensors). The FC at the edge collects and processes data incoming from each sensor in the network.

munication between the BS, which then acts as a Tx, and a UE. During this downlink transmission, the sensors collect the BS signal scattered by the target and, after processing, exchange information with a FC; the FC is at the edge of the network and may be part of a Cloud-RAN. More precisely, the network comprises one Tx located at $\mathbf{p}_{\mathrm{TX}} = (x_{\mathrm{t}}, y_{\mathrm{t}})$ with N_{T} antenna elements, and N_{RX} single antenna Rxs located at $\mathbf{p}_{\mathrm{RX},i} = (x_{\mathrm{r},i}, y_{\mathrm{r},i})$, $i \in \{1, \ldots, N_{\mathrm{RX}}\}$. This configuration helps avoid the well-known self-interference issue in monostatic radar systems [20].

As better highlighted in Section 4.2.1, the BS is equipped with a ULA with multibeam radiation pattern to transmit the signal in the direction of the UE through the communication beam while performing sensing through another beam [22, 46].

In a multistatic configuration, the waveforms obtained by each bistatic pair are jointly processed by an FC, which locates a target $\mathbf{z} = (z_{\mathrm{x}}, z_{\mathrm{y}})^{\mathsf{T}}$ on the ellipse whose foci are the positions of the Tx and Rx and whose major axis is equal to the bistatic range. The latter is defined as $R_{\mathrm{bis},i} = R_{\mathrm{T}} + R_{\mathrm{R},i} = c\,\tau_i$, where R_{T} and R_{R} are the Tx-target and target-Rx distances, respectively

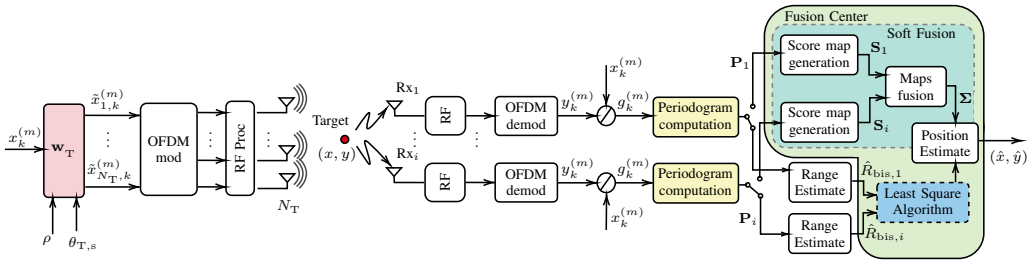

Figure 4.2: Block diagram of the considered multistatic JSC system. The signal transmitted by Tx and scattered by a generic target in the area is then collected by several Rxs that act as sensors. Every sensor independently computes a range map and sends it to the FC for the subsequent estimation process.

[76], and $\tau_i = (R_\mathrm{T} + R_{\mathrm{R},i})/c$ is the ToA of the signal at the ith receiver. The distance between the Tx and the ith Rx, L_i, is generally known as the ith baseline. The equation of the ellipse is therefore [37]

$$\sqrt{(z_\mathrm{x} - x_{\mathrm{r},i})^2 + (z_\mathrm{y} - y_{\mathrm{r},i})^2} + \sqrt{(z_\mathrm{x} - x_\mathrm{t})^2 + (z_\mathrm{y} - y_\mathrm{t})^2} = c\tau_i \,. \tag{4.1}$$

Hence, target localization may be viewed essentially as an ellipse intersection problem. For the system to work properly, the guard time t_G of the OFDM symbol must be larger than the excess delay of the scattered signal with respect to the direct one (i.e., the Tx-Rx propagation delay) to prevent ISI and provide unambiguous range detection. As a result, the maximum detectable bistatic range is related to t_G according to

$$R_{\mathrm{bis,max},i} \leq c\, t_\mathrm{G} + L_i \tag{4.2}$$

leading to a maximum ellipse with minor axis $A_{\mathrm{max},i} = \sqrt{(t_\mathrm{G} c + L_i)^2 - L_i^2}$.

4.2.1 Transmitted and Received Signals

The whole signal processing chain of the considered multistatic JSC system is depicted in Fig. 4.2. As previously mentioned, the transmitted signal is a 5G NR signal that consists of M OFDM symbols and K active subcarriers to form a $K \times M$ matrix of complex-valued modulation symbols $x_k^{(m)}$ [47]. At the Tx, the first performed operation is precoding through a beamforming

vector $\mathbf{w}_{\mathrm{T}}$, with the aim of creating a multibeam radiation pattern. This is done since the idea behind the system is to share the total available power between communication and sensing, thus employing the signals transmitted to the UEs for both tasks. To this purpose, $\mathbf{w}_{\mathrm{T}}$ is defined as

$$\mathbf{w}_{\mathrm{T}} = \sqrt{\rho}\,\mathbf{w}_{\mathrm{T,s}} + \sqrt{1-\rho}\,\mathbf{w}_{\mathrm{T,c}} \tag{4.3}$$

where $\rho \in [0,1]$ defines the trade-off between communication and sensing, while $\mathbf{w}_{\mathrm{T,s}}$ and $\mathbf{w}_{\mathrm{T,c}}$ are the beamforming vectors for the direction of sensing and communication, respectively. Since we are considering a ULA with N_{T} elements and half-wavelength separation between them, the array steering vector for a generic DoD θ is given by [54]

$$\mathbf{a}_{\mathrm{T}}(\theta) = [1, e^{j\pi\sin\theta}, \ldots, e^{j\pi(N_{\mathrm{T}}-1)\sin\theta}]^{\mathsf{T}}. \tag{4.4}$$

Using (4.4) and denoting by $\theta_{\mathrm{T,s}}$ and $\theta_{\mathrm{T,c}}$ the generic DoDs for sensing and communication, respectively, $\mathbf{w}_{\mathrm{T,c}}$ and $\mathbf{w}_{\mathrm{T,s}}$ are given by

$$\mathbf{w}_{\mathrm{T,c}} = \frac{\sqrt{P_{\mathrm{T}}G_{\mathrm{T}}^{\mathrm{a}}}}{N_{\mathrm{T}}}\mathbf{a}_{\mathrm{T}}^{\mathsf{c}}(\theta_{\mathrm{T,c}}) \quad \mathbf{w}_{\mathrm{T,s}} = \frac{\sqrt{P_{\mathrm{T}}G_{\mathrm{T}}^{\mathrm{a}}}}{N_{\mathrm{T}}}\mathbf{a}_{\mathrm{T}}^{\mathsf{c}}(\theta_{\mathrm{T,s}}) \tag{4.5}$$

where $\mathbf{a}_{\mathrm{T}}(\theta_{\mathrm{T,c}}) \in \mathbb{C}^{N_{\mathrm{T}}\times 1}$ and $\mathbf{a}_{\mathrm{T}}(\theta_{\mathrm{T,s}}) \in \mathbb{C}^{N_{\mathrm{T}}\times 1}$ are the steering vectors for communication and sensing, respectively, and $P_{\mathrm{T}}G_{\mathrm{T}}^{\mathrm{a}}$ is the EIRP, with $G_{\mathrm{T}}^{\mathrm{a}}$ the transmit array gain.

From (4.3), the vector of transmitted modulation symbols after beamforming is defined as $\tilde{\mathbf{x}}_k^{(m)} = \mathbf{w}_{\mathrm{T}}x_k^{(m)}$. After precoding, a new matrix of complex-valued symbols of elements $\tilde{x}_k^{(m)}$ is obtained for each antenna. Then, the signal is modulated through an OFDM modulator, upconverted, and sent by Tx through the wireless channel, where it is scattered by the objects in the surveilled area and the reflections are collected by multiple Rxs of the multistatic network. Since in this thesis we consider single antenna receivers, under the realistic assumption of negligible ISI and inter-carrier interference (ICI), the expression of the modulation symbol transmitted on the subcarrier k and OFDM symbol m and received by the ith Rx after downconversion and OFDM demodulation, can be written as

$$y_{i,k}^{(m)} = \mathbf{h}_{i,k}^{(m)} \tilde{\mathbf{x}}_k^{(m)} + n_{i,k}^{(m)} \tag{4.6}$$

where $n_{i,k}^{(m)}$ are i.i.d. noise samples having a complex Gaussian distribution with zero mean and variance σ_{N}^2 and $\mathbf{h}_{i,k}^{(m)} \in \mathbb{C}^{1\times N_{\mathrm{T}}}$ is the channel gain between Tx and the ith Rx for the mth OFDM symbol and kth subcarrier. In particular, considering a scenario with Q point-like targets and LOS propagation condition, the channel vector can be written as [85]

$$\mathbf{h}_{i,k}^{(m)} = \sum_{q=1}^{Q} \alpha_{i,q} e^{j2\pi m T_{\mathrm{s}} f_{\mathrm{D},i,q}} e^{-j2\pi k \Delta f \tau_{i,q}} \mathbf{a}_{\mathrm{T}}^{\mathsf{T}}(\theta_q) \tag{4.7}$$

where T_{s} is the total OFDM symbol duration, Δf is the subcarrier spacing, $f_{\mathrm{D},i,q}$, $\tau_{i,q}$, θ_q, and $\alpha_{i,q}$ are the Doppler shift, the propagation delay, the DoD, and the complex attenuation factor related to the qth back-scattered signal at the ith Rx, respectively.

4.2.2 Received Power and Cassini Ovals

In a multistatic radar network, for each bistatic pair the power received by a point target q with a RCS $\sigma_{\mathrm{rcs},q}$, that is illuminated by the Tx sensing beam and collected at the ith Rx under free-space propagation conditions, is given by[1]

$$P_{\mathrm{R},i,q}^{\mathrm{bis}} = \frac{\rho P_{\mathrm{T}} G_{\mathrm{T}} G_{\mathrm{R}} c^2 \sigma_{\mathrm{rcs},q}}{(4\pi)^3 f_{\mathrm{c}}^2 (R_{\mathrm{T},q} R_{\mathrm{R},i,q})^2} \tag{4.8}$$

where $R_{\mathrm{T},q}$ and $R_{\mathrm{R},i,q}$ are the Tx-target and ith Rx-target distances for target q, respectively, G_{R} is the Rx antenna gain, f_{c} is the carrier frequency, and c is the speed of light. Therefore, the SNR at each Rx for target q is

$$\mathrm{SNR}_{i,q} = \frac{P_{\mathrm{R},i,q}^{\mathrm{bis}}}{N_0 K \Delta f} \tag{4.9}$$

where N_0 is the one-sided noise PSD at the Rx. For each bistatic pair, it is helpful to identify the Cassini oval as the locus of points where the product of the distances $R_{\mathrm{T},q} R_{\mathrm{R},i,q}$ from two foci that correspond to the Tx and ith Rx, respectively, is constant [37, 76]. Therefore, Cassini ovals are iso-SNR

[1] Without loss of generality the beam is considered aligned with the target.

contours in the monitored area.

4.3 Estimation Techniques and Localization

This section introduces the approaches for bistatic range and target position estimation. For the bistatic range, a periodogram-based frequency estimation technique has been employed, leveraging the properties of OFDM. For the target position, two different methods have been compared, namely, LS and soft maps fusion. Without loss of generality, hereafter, we consider one point-like target, i.e., $Q = 1$, so the index q will be dropped. However, the whole discussion is generalizable to multiple targets if only one target is present in a given sensing direction; this is reasonable when the sensing beamwidth is relatively small.

4.3.1 Bistatic Range Estimation

As a first step, starting from the received symbols $y_{i,k}^{(m)}$, a division is performed to remove the dependency from the transmitted symbols, as $g_{i,k}^{(m)} = y_{i,k}^{(m)}/x_k^{(m)}$ [18].[2] Now $g_{i,k}^{(m)}$ contains two complex sinusoids for each target, whose frequencies are related to $f_{\mathrm{D},i}$ and τ_i. Given that the desired parameter to be estimated is the bistatic range, a one-direction periodogram along the subcarriers can be computed for each receiver, as opposed to [18, 20, 78], thus obtaining

$$\mathcal{P}_i(l) = \frac{1}{M_\mathrm{a}} \sum_{m=0}^{M_\mathrm{a}-1} \left| \sum_{k=0}^{K_\mathrm{p}-1} g_{i,k}^{(m)} e^{j2\pi \frac{kl}{K_\mathrm{p}}} \right|^2 \tag{4.10}$$

with $l = 0, \ldots, K_\mathrm{p} - 1$. In this thesis, $K_\mathrm{p} > K$ is obtained, via zero-padding, as the next power of two of K, while $M_\mathrm{a} \leq M$. The average with respect to the M_a OFDM symbols is performed to exploit a processing gain deriving from the non-coherent sum. Then, the location of the peak in the periodogram needs to be found, i.e., $\hat{l}_i = \arg\max_l \{\mathcal{P}_i(l)\}$, where, considering the assumption (4.2), we can limit the search range to $l = 0, \ldots, K'_{\mathrm{p},i} - 1$, with

[2] It is important to note that the transmitted symbols $x_k^{(m)}$ are known at the Rx, e.g., due to the correct demodulation of signals or the use of a predefined sequence for channel estimation.

$K'_{\mathrm{p},i} = \lfloor R_{\mathrm{bis,max},i} K_{\mathrm{p},i} \Delta f / c \rfloor$. Then, the bistatic range for the ith Rx can be evaluated as

$$\widehat{R}_{\mathrm{bis},i} = \frac{\hat{l}_i \, c}{\Delta f K_{\mathrm{p}}}. \tag{4.11}$$

4.3.2 Least Square Algorithm

In Section 4.3.1, we described a bistatic range estimation algorithm performed by each Rx node surveying the area. The next step consists of fusing together the hard-decision information generated by each Rx to estimate the target position. The estimation process starts from the evaluated bistatic ranges $\widehat{R}_{\mathrm{bis},i}$, $i \in \{1, 2, \ldots, N_{\mathrm{RX}}\}$, and from the knowledge of the positions of all Rxs and of the Tx in the area. The FC locates a target on the ellipse defined in (4.1), whose foci are the positions $(x_{\mathrm{t}}, y_{\mathrm{t}})$ and $(x_{\mathrm{r},i}, y_{\mathrm{r},i})$, and whose major axis is $\hat{d}_i = c\hat{\tau}_i = \widehat{R}_{\mathrm{bis},i}$. Squaring and reordering (4.1) yields

$$\begin{aligned} z_{\mathrm{x}}(x_{\mathrm{r},i} - x_{\mathrm{t}}) + z_{\mathrm{y}}(y_{\mathrm{r},i} - y_{\mathrm{t}}) - p_i \\ = \hat{d}_i \sqrt{(z_{\mathrm{x}} - x_{\mathrm{r},i})^2 + (z_{\mathrm{y}} - y_{\mathrm{r},i})^2} \end{aligned} \tag{4.12}$$

where $p_i = \frac{1}{2}(\hat{d}_i^2 - x_{\mathrm{r},i}^2 - y_{\mathrm{r},i}^2 + x_{\mathrm{t}}^2 + y_{\mathrm{t}}^2)$. When an LS approach is followed, the solution may be found by selecting n receivers, where $3 \leq n \leq N_{\mathrm{RX}}$. Then, denoting by $I \subseteq \{1, 2, \ldots, n\}$ the set of indexes of the selected receiver nodes, letting $j \in I$, for $i = j$ the expression (4.12) becomes

$$\begin{aligned} z_{\mathrm{x}}(x_{\mathrm{r},j} - x_{\mathrm{t}}) + z_{\mathrm{y}}(y_{\mathrm{r},j} - y_{\mathrm{t}}) - p_j \\ = \hat{d}_j \sqrt{(z_{\mathrm{x}} - x_{\mathrm{r},j})^2 + (z_{\mathrm{y}} - y_{\mathrm{r},j})^2}. \end{aligned} \tag{4.13}$$

For each $i \in I \setminus \{j\}$, the side-by-side difference between (4.12) multiplied by $\hat{d}_j$ and (4.13) multiplied by $\hat{d}_i$ is taken. This leads to $n - 1$ equations in the form

$$a_{i,j} z_{\mathrm{x}} + b_{i,j} z_{\mathrm{y}} = g_{i,j} \tag{4.14}$$

where

$$\begin{aligned} a_{i,j} =& \hat{d}_i(x_{\mathrm{r},j} - x_{\mathrm{t}}) - \hat{d}_j(x_{\mathrm{r},i} - x_{\mathrm{t}}) \\ b_{i,j} =& \hat{d}_i(y_{\mathrm{r},j} - y_{\mathrm{t}}) - \hat{d}_j(y_{\mathrm{r},i} - y_{\mathrm{t}}) \\ g_{i,j} =& \hat{d}_j p_i - \hat{d}_i p_j. \end{aligned} \tag{4.15}$$

Equation (4.14) can be recast in compact vector notation as $\mathbf{Az} = \mathbf{g}$, where $\mathbf{A}$ is a $(n-1) \times 2$ matrix whose ith row $i \in I \setminus \{j\}$ is given by $[a_{i,j}\ b_{i,j}]$ and $\mathbf{g}$ is a column vector with $n-1$ elements whose ith component $i \in I \setminus \{j\}$ is $g_{i,j}$. Finally, according to the LS algorithm, the target position may be estimated as

$$\hat{\mathbf{z}} = \arg\min_{\mathbf{z}} \|\mathbf{Az} - \mathbf{g}\| = (\mathbf{A}^{\mathsf{T}}\mathbf{A})^{-1}\mathbf{A}^{\mathsf{T}}\mathbf{g}. \tag{4.16}$$

4.3.3 Soft Maps Fusion

As mentioned above, each sensor performs a periodogram-based frequency estimation to determine bistatic range. The resulting "soft" vectors of dimension $K'_{\mathrm{p}} \times 1$, with elements $\mathcal{P}_i(l)$, can be delivered to the FC without any further in-sensor processing. Exploiting such a soft information, the FC generates a score map $\mathbf{S}$ of the surveillance area through a cell scoring (or *cell voting*) process. In order to do so, the area is divided into $N_{\mathrm{x}} \times N_{\mathrm{y}}$ grid cells, each of size $\Delta_{\mathrm{x}} \times \Delta_{\mathrm{y}}$ represented by indexes $(i_{\mathrm{x}}, i_{\mathrm{y}})$. Each element $\mathcal{P}_i(l)$ scores one or multiple grid cells, as follows. We denote by $\tau_i(l)$ the ToA corresponding to the element $\mathcal{P}_i(l)$. In a multistatic network, sample $\mathcal{P}_i(l)$ scores all cells that are crossed by an ellipse with equation (4.1) and major axis $c\tau_i(l) = R_{\mathrm{bis}_i}(l)$. The "amplitude" of the ellipse associated with the lth element $\mathcal{P}_i(l)$ is first evaluated as

$$V_i(l) = \frac{\mathcal{P}_i(l)^{\alpha}}{\frac{1}{K'_{\mathrm{p}}} \sum_{l=1}^{K'_{\mathrm{p}}} \mathcal{P}_i(l)^{\alpha}} \tag{4.17}$$

where $0 < \alpha < 1$ is used to mitigate strong clutter, thereby obtaining a total of K'_{p} ellipses from each sensor. Then, the scoring process is performed, where the score obtained by each of the $N_{\mathrm{x}} \times N_{\mathrm{y}}$ grid cells is defined as

$$S_i(i_{\mathrm{x}}, i_{\mathrm{y}}) = \max_{l=1,\ldots,K'_{\mathrm{p}}} V_i(l) I(l, i_{\mathrm{x}}, i_{\mathrm{y}}). \tag{4.18}$$

Table 4.1: JSC system parameters

5G specification →	NR 400
f_c [GHz]	28
Δf [kHz]	120
Active subcarriers K	3168
OFDM symbols per frame M	1120
Number of antennas N_T	50
Number of antennas N_R	1

In (4.18), the element $I(l, i_x, i_y)$ equals 1 if the lth ellipse passes through the grid cell (i_x, i_y), and 0 otherwise. Depending on the bistatic range resolution of the Rx node and on the dimension $\Delta_x \times \Delta_y$ of the grid cells, one cell may, in principle, be scored by several ellipses; in light of this, according to (4.18), only the largest received score by the grid cell is counted as its final score. Finally, one score map $\mathbf{S}_i$ is obtained for each Tx-Rx pair. The score maps produced from all receivers are then multiplied to construct an overall score map

$$\mathbf{\Sigma} = \prod_{i=1}^{N_{RX}} \mathbf{S}_i(i_x, i_y). \tag{4.19}$$

Finally, from the fusion of the soft bi-dimensional maps obtained for each Tx-Rx pair in the surveillance area, the location of the peak in (4.19) returns the estimated position of the target as

$$\hat{\mathbf{z}} = (\hat{z}_x, \hat{z}_y) = \underset{(i_x, i_y)}{\arg\max} \{[\mathbf{\Sigma}]_{i_x, i_y}\}. \tag{4.20}$$

4.4 System-Level Analysis

The performance of the multistatic JSC system is derived when it operates in track mode; hence, the BS is aware of a previous estimate of the DoD of the target so that the sensing beam can illuminate it. The 5G NR parameters considered in the simulations are shown in Table 4.1, where only a subset $M_a = 112$ of all OFDM symbols in the frame, modulated with a QPSK alphabet, are considered for position estimation. A square surveillance area of 100 m × 100 m, divided into square cells of 1 m^2, is monitored by the

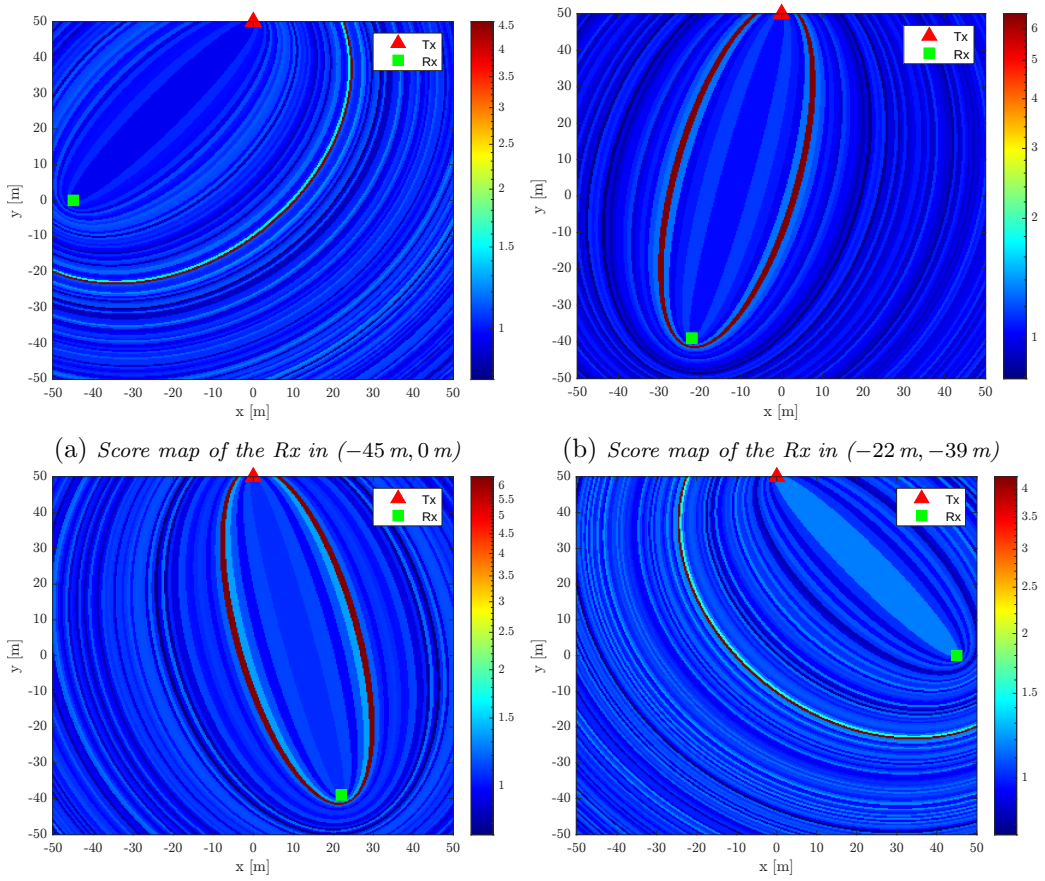

(a) *Score map of the Rx in* $(-45\,m, 0\,m)$

(b) *Score map of the Rx in* $(-22\,m, -39\,m)$

(c) *Score map of the Rx in* $(22\,m, -39\,m)$

(d) *Score map of the Rx in* $(45\,m, 0\,m)$

Figure 4.3: Score maps obtained for each Tx-Rx pair of the multistatic setup according to (4.18).

multistatic system with $N_{\mathrm{RX}} = 4$ sensors. The BS is located in $(0\,\mathrm{m}, 50\,\mathrm{m})$, while the four sensors lie on a circle of diameter equal to 90 m and center $(0\,\mathrm{m}, 0\,\mathrm{m})$, in positions $(-45\,\mathrm{m}, 0\,\mathrm{m})$, $(-22\,\mathrm{m}, -39\,\mathrm{m})$, $(22\,\mathrm{m}, -39\,\mathrm{m})$, and $(45\,\mathrm{m}, 0\,\mathrm{m})$, respectively. For each Tx-Rx pair present in the monitoring area, it is possible to observe an ellipse corresponding to the bistatic ranges of the targets in question, as can be seen in Fig. 4.3. An example of score map generated according to the metric (4.19) is given in Fig. 4.4, assuming that a target is moving inside the area in position $(0\,\mathrm{m}, -10\,\mathrm{m})$ and with velocity $(9, -5)$ [m/s]. Here, the soft maps generated by each sensor cover the entire surveillance area with $N_{\mathrm{x}} = N_{\mathrm{y}} = 100$ and $\Delta_{\mathrm{x}} = \Delta_{\mathrm{y}} = 0.3\,\mathrm{m}$. Unless otherwise specified, the fraction of power for the sensing beam is $\rho = 0.1$ (i.e.,

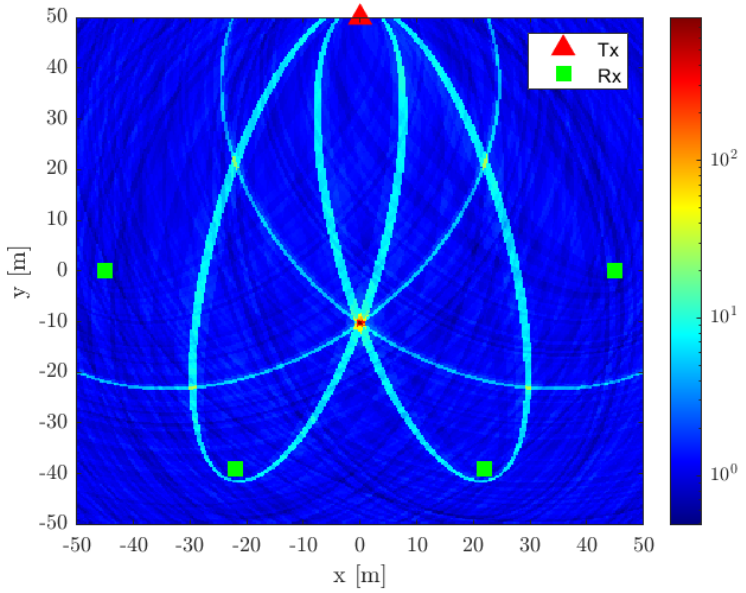

Figure 4.4: Example of soft maps fusion computed according to (4.19).

90% for the communication beam). Two types of analysis are then performed: 1) RMSE of the position estimate as a function of the fraction of power ρ dedicated to sensing; 2) system coverage analysis, performed by calculating the RMSE of the position estimate for a given ρ. In both cases, the following set of system parameters is considered: the clutter mitigation parameter is $\alpha = 1$; the target RCS is $\sigma_{\text{rcs}} = 1\,\text{m}^2$; the noise PSD is $N_0 = k_\text{B} T_0 F$ where $T_0 = 290\,\text{K}$ is the reference temperature, $F = 10\,\text{dB}$ is the receiver noise figure and $k_\text{B} = 1.38 \cdot 10^{-23}\,\text{JK}^{-1}$ is the Boltzmann constant; finally, the EIRP is set to $P_\text{T} G_\text{T} = 43\,\text{dBm}$, with $G_\text{R} = 1$. In the following, we assume that the ULA at the Tx is capable of steering the sensing beam within the range $[-\theta_0, +\theta_0]$ with $\theta_0 = 60\,^\circ$ (see Fig. 4.1).

4.4.1 RMSE vs ρ Analysis

The trade-off between communication and sensing varying ρ in (4.3) is analyzed through 5000 Monte Carlo iterations and shown in Fig. 4.5. For this type of analysis, several target locations inside the surveillance area have been considered, and the different results based on the two fusion approaches pre-

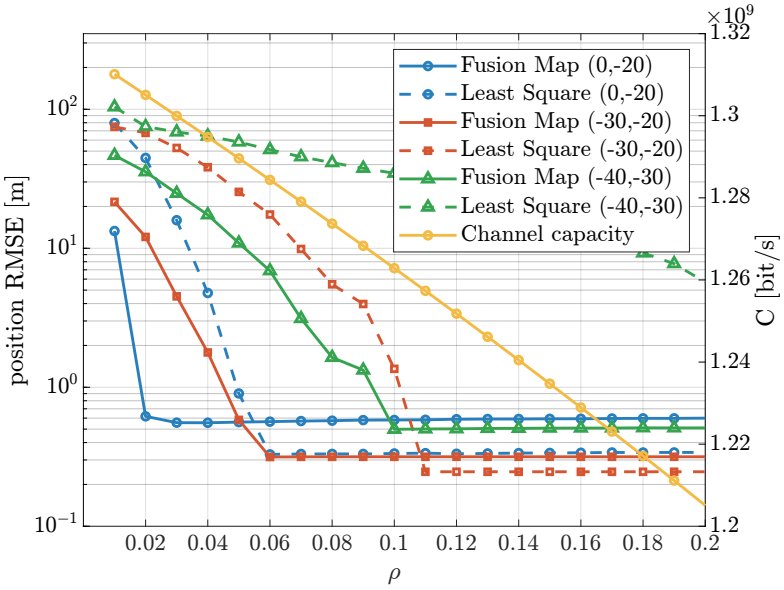

Figure 4.5: Sensing performance of the JSC system as a function of the parameter ρ for position RMSE calculated in three points inside the monitored area $(0\,\mathrm{m}, -20\,\mathrm{m})$, $(-30\,\mathrm{m}, -20\,\mathrm{m})$ and $(-40\,\mathrm{m}, -30\,\mathrm{m})$.

sented in this thesis are compared. It can be seen that depending on the position of the target, the RMSE exhibits a floor for increasing values of ρ (i.e., increasing the SNR for target position estimation); this depends on the geometry, that is, on how the ellipses combine (soft maps) or intersect (LS) and on the spatial discretization of the surveilled area. Furthermore, Fig. 4.5 shows that the fusion of soft maps, despite having a slightly higher RMSE floor, outperforms the LS algorithm in terms of power committed to sensing. This is because the latter approach heavily depends on the width of the Cassini oval and on the fact that the target must lie inside no less than three Cassini ovals to be detected: As the portion of the total power apportioned to sensing decreases, the Cassini ovals shrink in size, resulting in a higher position RMSE.

In terms of communication performance, let $C = K\Delta f \log_2(1 + (1 - \rho)\mathrm{SNR}^{\mathrm{c}})$ be the theoretical channel capacity, where $\mathrm{SNR}^{\mathrm{c}}$ is the communication SNR. Now, considering $\mathrm{SNR}^{\mathrm{c}} = 10\,\mathrm{dB}$ and the target at $(-30, -20)\,\mathrm{m}$, the fusion map approach requires $\rho = 6\%$ of the total power for sensing, leading to $C = 1.28\,\mathrm{Gbit/s}$, while the LS approach leads to $C = 1.26\,\mathrm{Gbit/s}$,

since the same RMSE now is achieved with $\rho = 11\%$. Therefore, compared to the communication-only case (i.e., $\rho = 0$), the communication capacity is reduced by 4.4% with LS and 2.3% with soft map fusion.

4.4.2 System Coverage Analysis

A direct representation of the position RMSE in each point of the surveillance area is portrayed through heatmaps, as in Fig. 4.6. In a bistatic configuration, the blind zone affecting a Tx-Rx pair close to the direct path may not be considered a system operation zone due to the corresponding high position error attributable to the inability of the radar component to discern between the direct Tx-Rx path and the Tx-target-Rx one [84]. In contrast, in the multistatic radar configuration investigated, the FC collects the information gathered by multiple Tx-Rx bistatic pairs (BS-sensor pairs in our scenario), therefore avoiding the blind zone issue by exploiting the bistatic range estimates obtained at the other sensors. In Fig. 4.6b, it can be seen how the performance of the LS approach in terms of position RMSE degrades for larger distances from the BS, as the sensing SNR decreases, whereas in Fig. 4.6a the fusion map approach is still able to achieve low position RMSE at low SNRs.

4.5 Conclusion

In this Chapter, we have investigated the performance of a multistatic sensor network based on 5G NR waveforms when using two different data fusion strategies. The first is based on bistatic range estimation at the sensor level followed by LS localization, and the other uses soft map fusion. The study concludes that: (i) soft map fusion outperforms the LS approach when a smaller fraction of power is devoted to sensing; (ii) a larger area is covered when soft map fusion is applied, as the LS algorithm is highly dependent on the width of the Cassini ovals; (iii) in the multistatic configuration, the FC is able to merge the sensing information of each sensor, thus allowing the system to avoid the well-known blind zone problem of bistatic configurations.

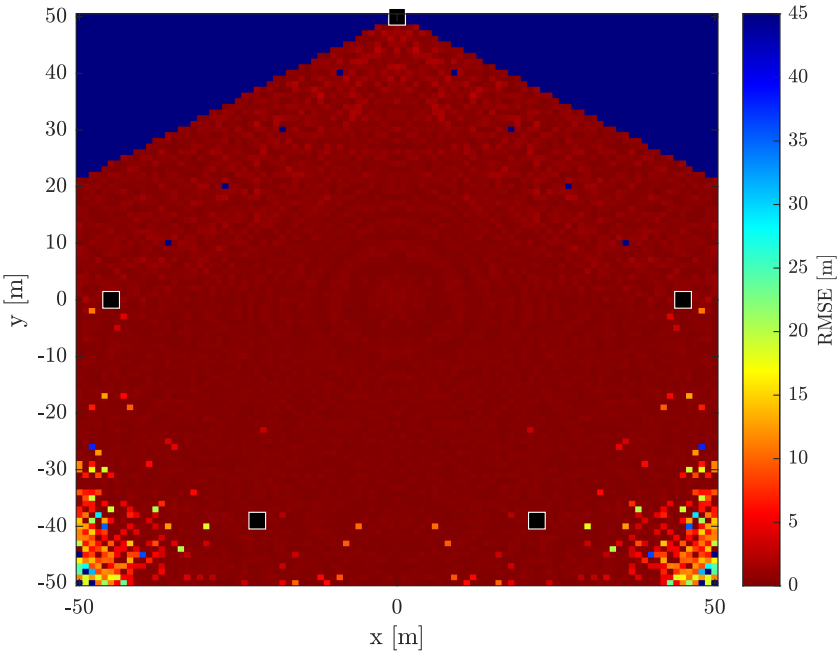

(a) *Soft maps fusion*

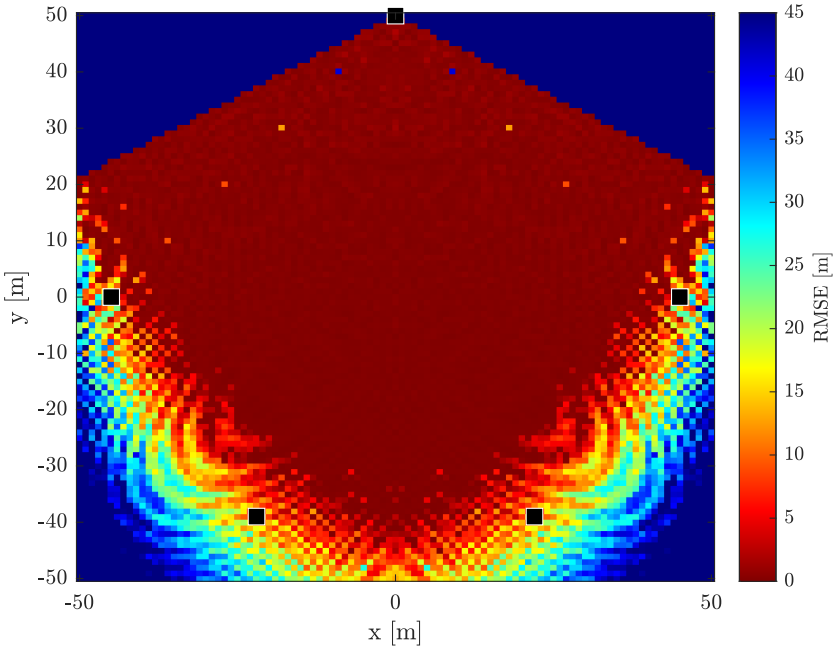

(b) *LS fusion*

Figure 4.6: Sensing area coverage of the JSC multistatic system with one Tx with $N_{\mathrm{T}} = 50$ and 4 single antenna Rx as a function of the position RMSE.

Chapter 5

Enhanced Data Fusion in Multistatic MIMO-OFDM JSC

5.1 Introduction

In this chapter, we further analyzed a multistatic system based on OFDM signals, designed to operate in two distinct modes: search and tracking. In the search mode described in Section 5.3, thanks to the availability of multiple antennas at the Rx, the system scans the environment to detect new targets and provides a preliminary estimate of their positions, leveraging cooperation among BSs by fusing range-angle maps from each receiver in the multistatic network. This approach enhances sensing capabilities and establishes a robust framework for real-time target detection and tracking. Simplified beam synchronization is achieved during the search phase by illuminating the entire scene, thereby reducing the complexity of coordinating transmitter and receiver beams across all sensors in the MIMO multistatic configuration. Furthermore, selective data fusion is introduced, ensuring that only reliable portions of the range-angle maps from each bistatic pair contribute to the cooperation process, leading to significant performance gains. The search capability is further improved through dynamic role rotation, allowing each BS to act as a transmitter in succession, enabling multi-view perception of targets and enhancing spatial diversity, detection accuracy, and localization performance. In the tracking mode described in Section 5.4, the

coarse target position estimates from the search phase are used to align the sensing beams of the transmitting BSs towards the detected targets. This alignment optimizes the transmit power and spatially filters clutter, further refining the tracking process. The performance of the proposed system is evaluated in both search and tracking modes, using the GOSPA metric to assess the accuracy of position estimates in the presence of multiple targets in Section 5.5. The results demonstrate the system's effectiveness in reducing localization errors and enhancing detection and tracking capabilities.

5.2 System Model

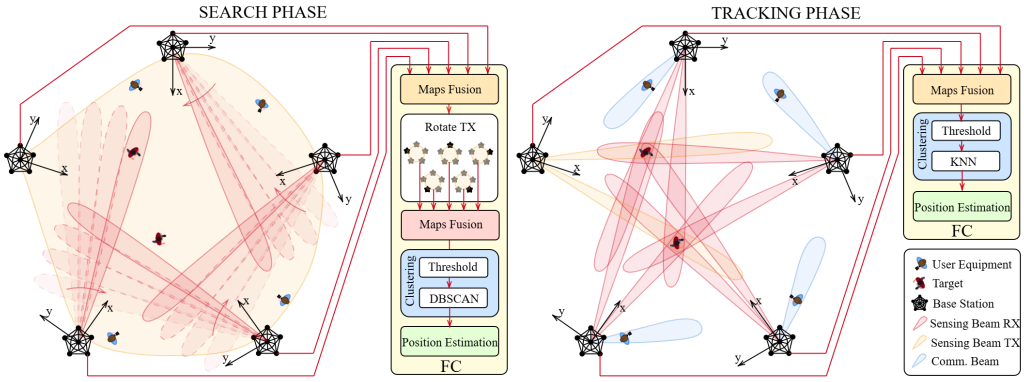

Figure 5.1: Beamforming patterns during the search and tracking phases. The left panel illustrates the search phase, where the Tx beam illuminates the area of interest, and the Rx beam sequentially scans with high sidelobe suppression to detect targets. The right panel represents the tracking phase, where multiple beams are formed at both Tx and Rx, each focused on a specific target. This configuration ensures continuous and accurate tracking of the detected targets.

We consider a JSC system configured as a multistatic radar network, as illustrated in Fig. 5.1, comprising several BSs operating at mmWave frequencies, each positioned at known locations. These BSs form multiple Tx-Rx (bistatic) pairs within the network. In this setup, sensing is performed during the downlink communication between a BS, serving as the Tx, and UEs, where the remaining BSs act as sensors in receiving mode. Let us define the set $\mathcal{S} = \{\mathbf{s}_1, \mathbf{s}_2, \ldots, \mathbf{s}_{|\mathcal{S}|}\}$, which contains the position $\mathbf{s}_i = [s_{\mathrm{x},i}, s_{\mathrm{y},i}]^\mathsf{T}$ of all the BSs, where $|\mathcal{S}|$ represents the total number of BSs. We write

$\mathcal{S}_t = \{\mathbf{s}_1, \mathbf{s}_2, \ldots, \mathbf{s}_t, \ldots, \mathbf{s}_{|\mathcal{S}|}\}$ to explicitly indicate that the tth BS acts as the Tx. Hence, for example, $\mathcal{S}_3$ represents a multistatic configuration in which the BS at position $\mathbf{s}_3$ acts as the Tx, while the remaining BSs operate in receiving mode. This configuration may change over time, as addressed later. Without loss of generality, the BSs are equipped with ULAs of N_{T} elements in transmission and N_{R} elements in reception, respectively, with a distance d between adjacent elements equal to half the wavelength, i.e., $d = \lambda/2$ with $\lambda = c/f_{\mathrm{c}}$, f_{c} being the carrier frequency and c the speed of light. During the downlink transmission, each receiving BS captures the signal reflected off a target, pre-process this signal locally (in-sensor processing), and exchange this processed data with an FC located at the network's edge; the FC may be part of a Cloud-RAN.

The network operation is divided into two phases: a search phase followed by a tracking phase.[1] Without prior knowledge of the target's number and initial location, the search phase aims to detect and coarsely estimate the positions of targets within the coverage area. During the subsequent tracking phase, the system utilizes the outcome of the search phase to track the targets continuously. As it will be better explained later, during this phase, similarly to the approach illustrated in [22, 46], the designated Tx employs a multibeam radiation pattern, where one or more communication beams are directed toward the UE(s), while other beams track previously detected targets leveraging the target state predictions provided by the tracking algorithms.

We consider the presence of Q targets within the monitored area whose actual positions are denoted as $\mathbf{z}_q = (z_{\mathrm{x},q}, z_{\mathrm{y},q})$ and collected in the set $\mathcal{Z} = \{\mathbf{z}_1, \mathbf{z}_2, \ldots, \mathbf{z}_Q\}$. Since a given multistatic network configuration $\mathcal{S}_t$ can be decomposed into $|\mathcal{S}|-1$ bistatic pairs that share the same Tx, each target lies on an ellipse identified by the foci that correspond to the Tx and Rx positions of that bistatic pair, with the major axis corresponding to the bistatic range. For each target q, the bistatic range related to a given Tx-Rx pair (t, i) is defined as $R_{t,q,i} = r_{t,q} + r_{q,i} = c\,\tau_{t,q,i}$. Here, $r_{t,q}$ and $r_{q,i}$ represent the distances from the Tx t to the qth target and from the qth target to the ith

[1] The two phases follow one another repeatedly to ensure continuous updates of the number of targets in the scene as it is generally time-varying.

Rx, respectively [76]. The corresponding ToA at the ith receiver of the signal transmitted by Tx t and scattered by the qth target is $\tau_{t,q,i} = (r_{t,q} + r_{q,i})/c$. The distance between the Tx t and the ith Rx, known as the baseline, is denoted as $L_{t,i}$. The equation of the ellipse for each target q for a given bistatic pair (t, i) is therefore given by [37]

$$\begin{aligned}&\sqrt{(z_{\mathrm{x},q} - s_{\mathrm{x},i})^2 + (z_{\mathrm{y},q} - s_{\mathrm{y},i})^2} \\ &+ \sqrt{(z_{\mathrm{x},q} - s_{\mathrm{x},t})^2 + (z_{\mathrm{y},q} - s_{\mathrm{y},t})^2} = c\,\tau_{i,q}\,. \end{aligned} \tag{5.1}$$

To ensure proper system functionality, i.e., to avoid ISI, the channel delay spread, calculated by considering the Tx-Rx LOS path component as the earliest significant multipath component, with a ToA equal to $\tau_{t,i} = L_{t,i}/c$, must be less than the guard time T_g between OFDM symbols. Consequently, the maximum detectable bistatic range for any target is related to T_g as follows

$$R_{\mathrm{bis},t,i}^{\max} \leq c\,T_\mathrm{g} + L_{t,i}\,. \tag{5.2}$$

This constraint limits the region observable by the bistatic pair (t, i), which is therefore bounded by a maximum ellipse with a minor axis of length $\sqrt{(T_\mathrm{g}c + L_{t,i})^2 - L_{t,i}^2}$.

5.2.1 Transmitted and Received Signals

The transmitted signal consists of a stream of M OFDM symbols with K active subcarriers, thus forming a $K \times M$ matrix of complex-valued modulation symbols $x_{k,m}$ with $\mathbb{E}\{|x_{k,m}|^2\} = 1$.[2] At the Tx, precoding is first applied to each modulation symbol to generate the vector of transmitted modulation symbols $\tilde{\mathbf{x}}[k, m] = \mathbf{w}_\mathrm{T} x_{k,m} \in \mathbb{C}^{N_\mathrm{T} \times 1}$ by using a beamforming vector $\mathbf{w}_\mathrm{T}$ such that $\|\mathbf{w}_\mathrm{T}\|_2^2 = P_\mathrm{avg}$. Here, $P_\mathrm{avg} = P_\mathrm{T}/K$ is the average power allocated per subcarrier, P_T being the total transmit power. The precoding vector choice depends on the operational phase of the network and will be discussed in detail in the following sections. The symbols are then OFDM modulated, upconverted, and transmitted through the wireless channel. The transmit-

[2]For the sake of simplicity, hereinafter, a generic Tx is considered and the index t is omitted. This is replaced by a generic T only when necessary.

ted signal is scattered by objects in the surveilled area, and the reflections are collected by multiple Rxs via the multistatic setup. Assuming negligible ISI and ICI, the vector of symbols received at the N_{R} antennas of the ith Rx for subcarrier k and time index m, after downconversion and OFDM demodulation, is expressed as

$$\tilde{\mathbf{y}}_i[k,m] = \mathbf{H}_i[k,m]\tilde{\mathbf{x}}[k,m] + \tilde{\mathbf{n}}_i[k,m] \tag{5.3}$$

where $\tilde{\mathbf{n}}_i[k,m] \in \mathbb{C}^{N_{\mathrm{R}}\times 1}$ is the noise samples vector with i.i.d. entries following a complex Gaussian distribution with zero mean and variance σ_{N}^2. Furthermore, $\mathbf{H}_i[k,m] \in \mathbb{C}^{N_{\mathrm{R}}\times N_{\mathrm{T}}}$ represents the frequency-domain channel matrix between the Tx and the ith Rx for the mth OFDM symbol and the kth subcarrier. Considering a scenario with Q point-like targets and $\mathcal{L}$ ground clutter points in LOS propagation conditions with respect to both Tx and Rx, the channel matrix can be expressed as [85]

$$\begin{aligned}\mathbf{H}_i[k,m] = &\sum_{q=1}^{Q} \alpha_{q,i} e^{j2\pi m T_{\mathrm{s}} f_{\mathrm{D},q,i}} e^{-j2\pi k \Delta f \tau_{q,i}} \mathbf{b}(\theta_{q,i})\mathbf{a}^{\mathsf{T}}(\phi_q) \\ &+ \sum_{\ell=1}^{\mathcal{L}} \beta_{\ell,i} e^{-j2\pi k \Delta f \tau_{\ell,i}} \mathbf{b}(\theta_{\ell,i})\mathbf{a}^{\mathsf{T}}(\phi_\ell).\end{aligned} \tag{5.4}$$

The first summation in (5.4) accounts for reflections from the targets, while the second one is related to the static ground clutter. In particular, in the first summation, $\alpha_{q,i}$, $\tau_{q,i}$, and $f_{\mathrm{D},q,i}$ are the complex channel gain, ToA, and bistatic Doppler shift, respectively, related to target q. Moreover, $\mathbf{a}(\phi_q)$ and $\mathbf{b}(\theta_{q,i})$ are the Tx and Rx array response vectors, respectively, related to target q, $\theta_{q,i}$ and ϕ_q being the qth DoA and DoD, respectively.[3] Furthermore, Δf is the subcarrier spacing while $T_{\mathrm{s}} = 1/\Delta f + T_{\mathrm{g}}$ is the total OFDM symbol duration including cyclic prefix duration (or guard interval) T_{g}. In the second summation, $\beta_{\ell,i}$, $\tau_{\ell,i}$, ϕ_ℓ, $\theta_{\ell,i}$, represent the complex attenuation gain,

[3]For a ULA with N_{a} elements spaced half a wavelength apart, as considered in this work, the steering vector for a generic direction θ is given by [54]

$$\mathbf{a}(\theta) = \left[e^{-j\pi\frac{N_{\mathrm{a}}-1}{2}\sin\theta}, \ldots, e^{j\pi\frac{N_{\mathrm{a}}-1}{2}\sin\theta}\right]^{\mathsf{T}}. \tag{5.5}$$

propagation delay, DoD, DoA of the ℓth static ground clutter component, respectively. Since, in this Chapter, the clutter is assumed to be static, its bistatic Doppler shift is assumed to be zero and the corresponding phase term (equal to 1) is omitted.

The complex channel gains $\alpha_{q,i}$ and $\beta_{\ell,i}$ take into account the attenuation and phase shift along the Tx-scatterer-Rx path. According to the radar equation, their amplitude results in [54]

$$|\alpha_{q,i}| = \sqrt{\frac{G_{\mathrm{R}} c^2 \sigma_{q,i}}{(4\pi)^3 f_c^2 (r_{\mathrm{T},q}\, r_{q,i})^2}} \qquad (5.6)$$
$$|\beta_{l,i}| = \sqrt{\frac{G_{\mathrm{R}} c^2 \sigma_{l,i}}{(4\pi)^3 f_c^2 (r_{\mathrm{T},l}\, r_{l,i})^2}}$$

where G_{R} is the gain of the single antenna element at the Rx, here assumed to be the same for each Rx, while $r_{\mathrm{T},q}, r_{q,i}$ ($r_{\mathrm{T},l}, r_{l,i}$) are the distances between the Tx and the qth (lth) reflection point, and the qth (lth) scatterer and the Rx, respectively. Furthermore, $\sigma_{q,i}$ ($\sigma_{l,i}$) represents the RCS of the qth (lth) reflection point. In this Chapter, scatterers, both targets and clutter, adhere to the Swerling I model, where the RCS σ follows an exponential distribution with p.d.f. [59]

$$f(\sigma) = \frac{1}{\bar{\sigma}} \exp\left(-\frac{\sigma}{\bar{\sigma}}\right) \qquad \sigma \geq 0 \qquad (5.7)$$

where $\bar{\sigma} = \mathbb{E}\{\sigma\}$ represents the mean RCS. The RCS is constant during the collection of a block of M symbols and varies independently from block to block. For the clutter, this model reflects realistic variability in ground reflections. It is worth noting that different Rxs, being well-separated in space, may observe varying scattering profiles of the target (i.e., different RCS values). This phenomenon, known as spatial diversity, is a geometric characteristic that can be leveraged to enhance target detection [86, 87].

By replacing (5.4) in (5.3) and expanding $\tilde{\mathbf{x}}[k, m]$, the received symbol

vector at subcarrier k and time m for the ith Rx can be rewritten as

$$\begin{aligned}
&\tilde{\mathbf{y}}_i[k,m] = \\
&= \sum_{q=1}^{Q} x_{k,m}\alpha_{q,i}e^{j2\pi m T_{\mathrm{s}} f_{\mathrm{D},q,i}} e^{-j2\pi k \Delta f \tau_{q,i}} \mathbf{b}(\theta_{q,i}) \underbrace{\mathbf{a}^{\mathsf{T}}(\phi_q)\mathbf{w}_{\mathrm{T}}}_{\triangleq \gamma(\phi_q)} \\
&\quad + \sum_{\ell=1}^{\mathcal{L}} x_{k,m}\beta_{\ell,i}e^{-j2\pi k \Delta f \tau_{\ell,i}} \mathbf{b}(\theta_{\ell,i}) \underbrace{\mathbf{a}^{\mathsf{T}}(\phi_\ell)\mathbf{w}_{\mathrm{T}}}_{\triangleq \gamma(\phi_l)} + \tilde{\mathbf{n}}_i[k,m]
\end{aligned} \tag{5.8}$$

where $|\gamma(\phi)|^2 = \rho_{\mathrm{p}} P_{\mathrm{avg}} G_{\mathrm{T}}^{\mathrm{a}}(\phi)$ represents the EIRP for a generic scatterer at DoD ϕ. This term incorporates the transmit power P_{avg} and the transmit antenna array gain (or beamforming gain) $G_{\mathrm{T}}^{\mathrm{a}}(\phi)$, which depends on the selected beamforming weight vector $\mathbf{w}_{\mathrm{T}}$ and the specific DoD. The factor ρ_{p} controls the fraction of the total available power allocated for sensing. In particular, during the tracking phase, as described in Section 5.4, sensing spatial multiplexing is performed at the transmit array using a multibeam radiation pattern. In this setup, a fraction ρ_{p} of the total available power is allocated for sensing, while the remaining $1 - \rho_{\mathrm{p}}$ is reserved for communication purposes.

Starting from the vector in (5.3), which contains the complex symbols received at each antenna of the ith sensing Rx, digital beamforming is performed using the receiving beamforming weight vector $\mathbf{w}_{\mathrm{R},i} \in \mathbb{C}^{N_{\mathrm{R}} \times 1}$. Similar to the beamforming vector at the Tx, $\mathbf{w}_{\mathrm{R},i}$ is designed differently depending on the system's operating mode. Specifically, during the search phase, it is designed to scan the entire monitored area considering a given number of sensing directions, while in the tracking phase, it simultaneously points to multiple sensing directions corresponding to the detected targets. More details about the beamforming design are provided in the next sections. After beamforming, the combined received symbol at subcarrier k and time m for the ith Rx is given by $y_{i,k,m} = \mathbf{w}_{\mathrm{R},i}^{\mathsf{T}} \tilde{\mathbf{y}}_i[k,m]$.

5.2.2 Sensing Received Power and SNR

The power received at a given array element n of the ith Rx, which collects the signal after it has been reflected by a point target q illuminated by the Tx sensing beam under free-space propagation conditions, can be expressed as

$$P_{\mathrm{R},i,q} = \mathbb{E}\{|y_{i,k,m}^{(n,q)}|^2\} \tag{5.9}$$

where $y_{i,k,m}^{(n,q)}$ represents the nth element of the received symbol vector in (5.8) considering the sole component related to scatterer q. By plugging (5.6) in (5.8) and considering also the term $|\gamma(\phi_q)|^2$ previously introduced, (5.9) can be rewritten as

$$P_{\mathrm{R},i,q} = \frac{\rho_p P_{\mathrm{avg}} G_{\mathrm{T}}^{\mathrm{a}} G_{\mathrm{R}} c^2 \sigma_{q,i}}{(4\pi)^3 f_{\mathrm{c}}^2 (r_{\mathrm{T},q}\, r_{q,i})^2}. \tag{5.10}$$

The corresponding SNR at the ith Rx for target q can therefore be expressed as

$$\mathrm{SNR}_{i,q} = \frac{P_{\mathrm{R},i,q}}{\sigma_{\mathrm{N}}^2} = \frac{c^2 \sigma_{q,i}}{(4\pi)^3 f_{\mathrm{c}}^2 (r_{\mathrm{T},q}\, r_{q,i})^2} \cdot \frac{\rho_p P_{\mathrm{T}} G_{\mathrm{T}}^{\mathrm{a}} G_{\mathrm{R}}}{N_0 K \Delta f} \tag{5.11}$$

where $N_0 = k_{\mathrm{B}} F T_0$ is the one-sided noise PSD at the Rx, k_{B} being the Boltzmann constant, F the noise figure and T_0 the reference temperature.

5.2.3 Bistatic Range-Doppler Maps

Leveraging the inherent properties of OFDM, target parameters are estimated using periodogram-based frequency estimation [18]. The process starts by applying reciprocal filtering, which removes the influence of the transmitted symbols from the beamformed received symbols by calculating the ratio $g_{i,k,m} = y_{i,k,m}/x_{k,m}$ [18, 88].[4]

The resulting complex element $g_{i,k,m}$ includes two complex sinusoids for each target q, whose frequencies correspond to the bistatic Doppler shift $f_{\mathrm{D},q,i}$ and the propagation delay $\tau_{q,i}$. For this reason, the sensing parameter es-

[4] In this work, we assume that the transmitted symbols $x_{k,m}$ are known at the Rx, either through accurate demodulation of the received signals or by using a known pilot sequence such as for channel estimation purposes.
It is worth noting that the division here performed does not alter the noise statistics when constant-envelope modulations, such as phase shift keying (PSK) or 4-quadrature amplitude modulation (QAM), are employed [65].

timation problem can be reduced to a frequency estimation and a bistatic range-Doppler map can be computed for each Rx belonging to a given multistatic configuration $\mathcal{S}_{\mathrm{T}}$ [18, 20], as

$$\mathcal{P}_i(l,p) = \frac{1}{KM}\left|\sum_{k=0}^{K_{\mathrm{p}}-1}\left(\sum_{m=0}^{M_{\mathrm{p}}-1} g_{i,k,m} w_{\mathrm{K},m} e^{-j2\pi\frac{mp}{M_{\mathrm{p}}}}\right) e^{j2\pi\frac{kl}{K_{\mathrm{p}}}}\right|^2 \tag{5.12}$$

where $w_{\mathrm{K},m}$ is the mth sample of an $[M\times 1]$ Kaiser window $\mathbf{w}_{\mathrm{K}}$ with parameter $\beta = 3$, which is used to reduce sidelobe effects along the Doppler dimension. This is normalized as $w_{\mathrm{K},m} = w_{\mathrm{K},m}/\sqrt{\frac{1}{M}\sum_{m=0}^{M-1} w_{\mathrm{K},m}^2}$ to preserve the noise statistics. Moreover, $l = 0,\ldots,K_{\mathrm{p}}-1$ and $p = 0,\ldots,M_{\mathrm{p}}-1$, where $K_{\mathrm{p}} \geq K$ and $M_{\mathrm{p}} \geq M$ correspond to zero-padding before FFT and inverse fast Fourier transform (IFFT) calculation.[5] Given the constraint in (5.2), the range in which we search for targets can be restricted to $l = 0,\ldots,K_{\mathrm{p},i}-1$, where $K_{\mathrm{p},i} = \lfloor R_{\mathrm{bis},t,i}^{\max} K_{\mathrm{p}} \Delta f/c \rfloor$. For each l and p index in (5.12) it is possible to compute the corresponding bistatic range and bistatic Doppler shift values as

$$R_{\mathrm{bis},l} = \frac{lc}{K_{\mathrm{p}}\Delta f}, \qquad f_{\mathrm{D},p'} = \frac{p'}{M_{\mathrm{p}} T_{\mathrm{s}}} \tag{5.13}$$

where $p' = \left[\left(p + \frac{M_{\mathrm{p}}}{2}\right) \bmod M_{\mathrm{p}}\right] - \frac{M_{\mathrm{p}}}{2}$ accounts for negative bistatic Doppler shifts. In (5.13), the Rx index i is omitted, as the relations depend only on system parameters, which are assumed to be the same for all BSs in this work.

It is clear from (5.13) that the periodogram described in (5.12) provides a bistatic range-Doppler map. This map is then used to derive the range-angle maps during the search phase and the soft maps during the tracking phase, which will be described in the following sections. Moreover, the range-Doppler map can be used for clutter mitigation. As mentioned in Section 5.2.1, the considered scenario includes static clutter with a null Doppler shift. For this reason, Doppler frequencies within the range $[-p_0/(T_{\mathrm{s}}M_{\mathrm{p}}), p_0/(T_{\mathrm{s}}M_{\mathrm{p}})]$ are removed after each periodogram calculation to suppress the contribution of clutter, where p_0 defines the extent of the

[5] Zero-padding can be used to ensure, if necessary, that M_{p} and K_{p} are a power of two but also to perform spectral interpolation which may result in smoother bistatic range-Doppler maps [19].

Doppler region to be filtered.

5.3 Search Phase

The search mode described in this section is designed to detect and locate targets during the network's startup phase, when no prior information is available. Additionally, it regularly detects and updates the number of targets as they fluctuate over time [43, 73], and provides a coarse estimation of their positions. This process ensures an accurate and up-to-date representation of the environment. During this mode, each BS alternates between transmitting and receiving, enabling comprehensive coverage and enhancing spatial diversity across the monitored area. The system remains in search mode until every BS has completed its function as a transmitter.

5.3.1 Scanning of the Area with Beamforming

As mentioned in Section 5.2.1, the choice of precoding vector $\mathbf{w}_\mathrm{T}$ at the Tx depends on the chosen operational mode. During the search phase, $\mathbf{w}_\mathrm{T}$ is properly designed to generate a radiation pattern with nearly uniform gain on a given angular sector [77, 87], such that $\|\mathbf{w}_\mathrm{T}\|_2^2 = P_\mathrm{avg}$, as shown by the blue curve in Fig. 5.2. This large, uniform beam is crucial during the system's search mode, where the objective is to illuminate simultaneously all potential targets within the monitored area, with no need for beam alignment between Tx and Rxs. This approach diverges notably from traditional methods, such as those used in monostatic systems, where synchronization signals guide scanning at the Tx [89]. While the Tx illuminates simultaneously the whole area of interest, each Rx collects echoes generated from potential targets and produces a radar range-angle map by scanning the surrounding environment through digital beamforming. Below, the considered beamforming approach and scanning procedure are introduced, while more details on range-angle map computation are provided in Section 5.3.2.

Let N_dir be the total number of sensing directions to perform a complete scan, and $\boldsymbol{\theta}_{\mathrm{s},i} = [\theta_{1,i}, \theta_{2,i}, \ldots, \theta_{N_\mathrm{dir},i}]$ be the set of sensing directions for the

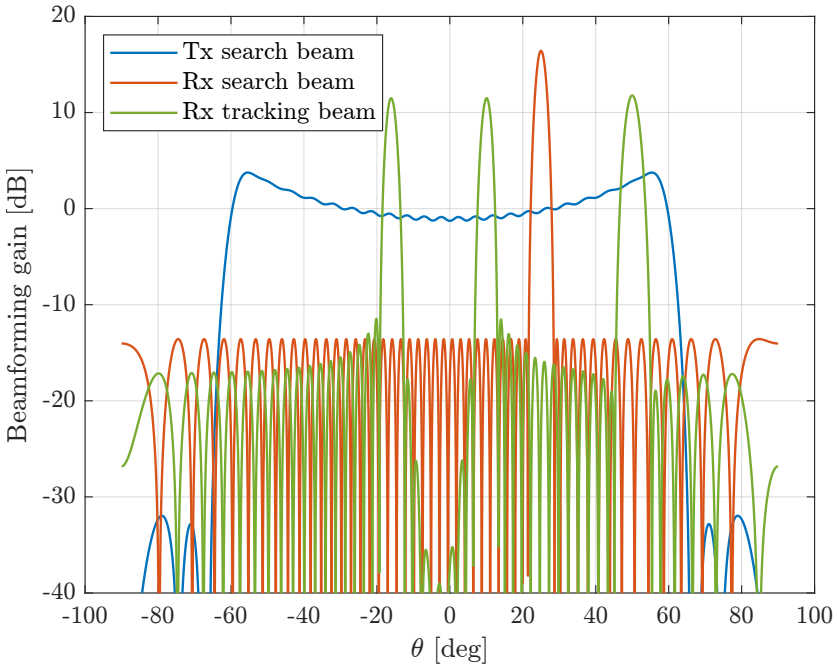

Figure 5.2: Beampattern in the search and tracking phases. During the search phase, the transmit beam illuminates the area of interest, while the pencil-like beam at the Rx sequentially scans the area. In the tracking phase, both Tx and Rx form multiple beams, one for each target being tracked. The transmit beampattern is shown here for $P_{\text{avg}} = 1$ to account only for the beamforming gain.

ith Rx. The jth direction is given by

$$\theta_{j,i} = \theta_{0,i} + j\Delta\theta_{\text{s}} \qquad j = 0, \ldots, N_{\text{dir}} - 1 \tag{5.14}$$

where, $\theta_{0,i}$ is the starting scan direction for the ith Rx with respect to its own reference system, and $\Delta\theta_{\text{s}}$ is the scan angle step.

In each sensing direction $\theta_{j,i}$, beamforming is performed using the weight vector $\mathbf{w}_{\text{R}}$. A common approach involves conjugating the array response vector at the receiver, i.e., $\tilde{\mathbf{w}}_{\text{R}} = \mathbf{b}^{\text{c}}(\theta_{j,i})/\|\mathbf{b}^{\text{c}}(\theta_{j,i})\|_2$, to maximize power in the desired direction $\theta_{j,i}$. However, this approach often results in relatively high sidelobes, which are undesirable in sensing applications as they can cause interference between targets. To address this, the array aperture can be windowed by element-wise multiplying $\tilde{\mathbf{w}}_{\text{R}}$ with the window weight vector

$\mathbf{c}$ [77]. The final beamforming vector is then given by

$$\mathbf{w}_{\mathrm{R}} = \tilde{\mathbf{w}}_{\mathrm{R}} \odot \mathbf{c} \tag{5.15}$$

where $\mathbf{c}$ is normalized such that $\|\mathbf{w}_{\mathrm{R}}\|_2^2 = 1$. In this Chapter, a Dolph-Chebyshev window with a 30 dB peak-to-sidelobe ratio is employed. An example of the resulting radiation pattern for a given sensing direction $\theta_{j,i}$, using this window, is shown by the red curve in Fig. 5.2.

Since the Tx illuminates the entire area with a broad radiation pattern, digital beamforming at each Rx can be used for spatial filtering, by processing all sensing directions with the same received signal. In particular, the ith Rx applies beamforming sequentially on the received signal $\tilde{\mathbf{y}}_i[k, m]$ for each sensing direction j, using the weight vector $\mathbf{w}_{\mathrm{R}}$ related to that direction. For each sensing direction, after beamforming, the Rx computes the periodogram as in (5.12) and constructs the corresponding bistatic range-Doppler map.

For the reason mentioned above, the duration of a full scan at each Rx, denoted as T_{scan}, is determined by the total OFDM signal duration, i.e., $T_{\mathrm{scan}} = M \cdot T_{\mathrm{s}}$. Once all sensing directions have been processed and each BS has operated as a Tx, the search mode is complete. The total scanning time is therefore $T_{\mathrm{search}} = T_{\mathrm{scan}} \cdot |\mathcal{S}|$.[6]

It is worth noting that the broad sensing beam used at the Tx during the search phase does not support spatial multiplexing between sensing and communication, meaning that it cannot simultaneously scan the environment and serve UEs in the area (see, e.g., [22, 46]), therefore $\rho_{\mathrm{p}} = 1$. Consequently, this work assumes that all available frequency resources are exclusively allocated to sensing during this short-term phase. However, an alternative approach could allocate only a fraction of the subcarriers to sensing, sufficient for a coarse estimation of the target's position, while reserving the remaining subcarriers for downlink communication with the UEs.

[6] This duration does not include potential overheads such as beamforming reconfiguration or processing latency.

5.3.2 Range-Angle Map Calculation

Before we explain how range-angle maps are generated, it is worth noting that a critical issue in bistatic radar configurations is the blind zone, a region near the baseline where target detection becomes challenging. This difficulty arises because limitations in time resolution may impede the separation between the direct Tx-Rx path and the indirect Tx-target-Rx path [90]. Given the resolution of the bistatic range estimate, $\Delta R_{\text{bis}} = \frac{c}{K_{\text{p}}\Delta f}$, targets within a bistatic range less than $L_i + \Delta R_{\text{bis}}$ cannot be reliably resolved. Therefore, to ensure reliable target detection, the bistatic range must satisfy $R_{\text{bis}} \geq L_i + \Delta R_{\text{bis}}$; this is often referred to as the minimum ellipse. Consequently, during the search phase, the bistatic range periodogram bins of the ith Rx can be further restricted to $l' = K'_{\text{p},i}, \ldots, K_{\text{p},i} - 1$ where $K'_{\text{p},i} = \lceil L_i K_{\text{p}} \Delta f / c \rceil$. This approach ensures that the periodogram bins evaluate the bistatic range of the targets at discrete values according to $R_{\text{bis},l'} = \frac{l'c}{\Delta f K_{\text{p}}}$. Now, at the ith Rx, a range-angle map can be obtained by computing first the bistatic range-Doppler map, introduced in Section 5.2.3, after applying beamforming for each sensing direction j. As already mentioned, the range-Doppler map contains information on the bistatic range R_{bis} and the bistatic Doppler shift f_{D}. To accurately interpret the bistatic range data, it is necessary to convert the bistatic range value $R_{\text{bis},l}$ in (5.13), into the target-to-Rx range $R_{\text{R},l'}$ value. This conversion is performed for each $l' = K'_{\text{p},i}, \ldots, K_{\text{p},i} - 1$, using the relationship [76]

$$R_{\text{R},l'} = \frac{R_{\text{bis},l'}^2 - L_i^2}{2(R_{\text{bis},l'} + L_i \sin(\theta_{j,i} - \pi/2))} \,. \tag{5.16}$$

Then, for a given target-Rx distance $R_{\text{R},l'}$ and sensing direction $\theta_{j,i}$, the Cartesian coordinates of the corresponding point in the surveilled area—represented by the range-angle map—are $(x, y) = (R_{\text{R},l'} \cos\theta_{j,i}, R_{\text{R},l'} \sin\theta_{j,i})$. Finally, assuming a relatively small beamwidth of the receiving beamforming vector, it is likely that only one target is present in any given sensing direction. Therefore, for each direction j we extract the column of the periodogram obtained in (5.12) corresponding to the peak value to obtain a

vector $\mathbf{r}_{j,i} = (P_{j,i}(1), \ldots, P_{j,i}(K_{\mathrm{p},i} - K'_{\mathrm{p},i}))^{\mathsf{T}}$, with

$$P_{j,i}(l') = \mathcal{P}_{j,i}(l', p)|_{p=\hat{p}} \quad \text{for} \quad j = 1, \ldots, N_{\mathrm{dir}} \tag{5.17}$$

which represents the range profile in the jth direction. The index $\hat{p}$ identifies the column where the peak in the periodogram is located

$$\hat{p} = \arg\max_{p} \{\mathcal{P}_{j,i}(l', p)\}\,. \tag{5.18}$$

By repeating this extraction process for all N_{dir} directions, as specified in (5.14), we arrange these vectors into a new matrix $\mathbf{R}_i \in \mathbb{R}^{(K_{\mathrm{p},i} - K'_{\mathrm{p},i}) \times N_{\mathrm{dir}}}$

$$\mathbf{R}_i = \left[\mathbf{r}_i^{(1)} \mathbf{r}_i^{(2)} \ldots \mathbf{r}_i^{(N_{\mathrm{dir}})}\right] \quad \in \mathbb{R}^{(K_{\mathrm{p},i} - K'_{\mathrm{p},i}) \times N_{\mathrm{dir}}} \tag{5.19}$$

which represents the intensity of the range angle map of the ith Rx.

Then, target detection is performed using a binary hypothesis test with threshold η is applied to the range-angle maps to distinguish noise from the useful signal, as

$$\mathbf{R}_i(l', j) \underset{\mathcal{H}_0}{\overset{\mathcal{H}_1}{\gtrless}} \eta, \tag{5.20}$$

where $\mathcal{H}_0$ and $\mathcal{H}_1$ represent the hypotheses corresponding to the absence of a target (i.e., noise only) and the presence of a target, respectively.

The detection threshold η is chosen to achieve a desired false-alarm probability $P_{\mathrm{FA,point}}$, which is related to the total FAR in the search space of size $|\mathbf{R}_i|$ as $P_{\mathrm{FA,point}} = \mathrm{FAR}/|\mathbf{R}_i|$. It is straightforward to show that if there is only noise at the receiver, the values of $\mathbf{R}_i(l', j)$ are exponentially distributed with a mean proportional to the noise power σ_{N}^2. Thus, the threshold η can be expressed as [91]

$$\eta = -\sigma_{\mathrm{N}}^2 \ln P_{\mathrm{FA,point}}. \tag{5.21}$$

This threshold-based approach is applied to the range-angle maps at each individual BS, enabling collaborative detection across multiple BSs. Such collaboration enhances the system's robustness and reliability, as targets missed by one BS can still be detected by others, improving the overall detection

performance.

5.3.3 Reliability Maps for Selective Data Fusion

The Tx-Rx bistatic pair, which represents the building block of the multistatic network, presents a unique characteristic of the target position resolution, which varies with the target position and, in some portions of the area suffers from notable distortion, especially when targets fall near the baseline. Indeed, when constructing a range-angle map in a bistatic system from (5.16), finite angular resolution leads to a variable spacing between consecutive points on the ellipse, depending on their distance with respect to the baseline. For instance, near the baseline, the spacing between consecutive $(R_{\text{bis},l'},\theta_{j,i})$ points increases dramatically, resulting in large uncertainty areas (low spatial resolution) when these points are converted to Cartesian coordinates. This enlargement causes even point-like targets to appear extended, complicating the differentiation between point-like and extended targets. To counteract this geometric distortion, we introduce reliability maps, denoted as $\mathbf{M}_i \in \mathbb{R}^{(K_{\text{p},i}-K'_{\text{p},i})\times N_{\text{dir}}}$, that depend exclusively on the geometric configuration of the multistatic network and serve to quantify such geometrical distortions to select which portions of the range-angle maps at Rx i can be included in data fusion and which should not.[7] At first, for a generic $R_{\text{bis},l'}$ and DoA $\theta_{j,i}$, we identify four adjacent points

$$\begin{aligned}&(x_{\text{A}}, y_{\text{A}}) = R_{\text{R}}^{\text{A}} \cdot \big(\cos\big(\theta_{j,i} + \delta\theta/2\big), \sin\big(\theta_{j,i} + \delta\theta/2\big)\big) \text{ with}\\ &R_{\text{R}}^{\text{A}} = \frac{(R_{\text{bis},l'} - \frac{\Delta R_{\text{bis}}}{2})^2 - L_i^2}{2(R_{\text{bis},l'} - \frac{\Delta R_{\text{bis}}}{2} + L_i \sin\left(\theta_{j,i} + \frac{\delta\theta}{2} - \pi/2\right))}\end{aligned} \tag{5.22}$$

$$\begin{aligned}&(x_{\text{B}}, y_{\text{B}}) = R_{\text{R}}^{\text{B}} \cdot \big(\cos\big(\theta_{j,i} + \delta\theta/2\big), \sin\big(\theta_{j,i} + \delta\theta/2\big)\big) \text{ with}\\ &R_{\text{R}}^{\text{B}} = \frac{(R_{\text{bis},l'} + \frac{\Delta R_{\text{bis}}}{2})^2 - L_i^2}{2(R_{\text{bis},l'} + \frac{\Delta R_{\text{bis}}}{2} + L_i \sin\left(\theta_{j,i} + \frac{\delta\theta}{2} - \pi/2\right))}\end{aligned} \tag{5.23}$$

[7] Note that the reliability maps are precomputed once for each possible bistatic pair at each Rx, given that all potential Tx-Rx configurations are known a priori.

$$(x_{\mathrm{C}}, y_{\mathrm{C}}) = R_{\mathrm{R}}^{\mathrm{C}} \cdot \big(\cos\big(\theta_{j,i} - \delta\theta/2\big), \sin\big(\theta_{j,i} - \delta\theta/2\big)\big) \text{ with}$$
$$R_{\mathrm{R}}^{\mathrm{C}} = \frac{(R_{\mathrm{bis},l'} + \frac{\Delta R_{\mathrm{bis}}}{2})^2 - L_i^2}{2(R_{\mathrm{bis},l'} + \frac{\Delta R_{\mathrm{bis}}}{2} + L_i \sin(\theta_{j,i} - \frac{\delta\theta}{2} - \pi/2))} \tag{5.24}$$

$$(x_{\mathrm{D}}, y_{\mathrm{D}}) = R_{\mathrm{R}}^{\mathrm{D}} \cdot \big(\cos\big(\theta_{j,i} - \delta\theta/2\big), \sin\big(\theta_{j,i} - \delta\theta/2\big)\big) \text{ with}$$
$$R_{\mathrm{R}}^{\mathrm{D}} = \frac{(R_{\mathrm{bis},l'} - \frac{\Delta R_{\mathrm{bis}}}{2})^2 - L_i^2}{2(R_{\mathrm{bis},l'} - \frac{\Delta R_{\mathrm{bis}}}{2} + L_i \sin(\theta_{j,i} - \frac{\delta\theta}{2} - \pi/2))} \tag{5.25}$$

where $\delta\theta$ is the beamwidth at the Rx beamformer.[8] These four points form a polygon in the Cartesian coordinate system whose area can be calculated as

$$A_{\mathrm{res}} = \frac{1}{2}\big|x_{\mathrm{A}}y_{\mathrm{B}} + x_{\mathrm{B}}y_{\mathrm{C}} + x_{\mathrm{C}}y_{\mathrm{D}} + x_{\mathrm{D}}y_{\mathrm{A}} + - (y_{\mathrm{A}}x_{\mathrm{B}} + y_{\mathrm{B}}x_{\mathrm{C}} + y_{\mathrm{C}}x_{\mathrm{D}} + y_{\mathrm{D}}x_{\mathrm{A}})\big| . \tag{5.26}$$

Such an area can be interpreted as an uncertainty area associated with the spatial resolution of the bistatic pair. A threshold γ_{res} can then be defined so that when the uncertainty area exceeds this threshold, the corresponding (x, y) point in the range-angle map $\mathbf{R}_i$ is marked as unreliable, i.e., non-informative of the target presence and position. More precisely

$$[\mathbf{M}_i]_{l',j} = \begin{cases} 1 & \text{if } A_{\mathrm{res}} < \gamma_{\mathrm{res}} \\ 0 & \text{otherwise.} \end{cases} \tag{5.27}$$

Finally, the reliability map, depicted in Fig. 5.3, is applied to the range-angle map of each Rx to mask points deemed uninformative

$$\overline{\mathbf{R}}_i = \mathbf{R}_i \odot \mathbf{M}_i \quad i = 1, \ldots, |\mathcal{S}| - 1. \tag{5.28}$$

Area threshold selection is crucial: a low threshold can lead to the excessive removal of large regions in the range-angle maps, potentially causing the loss of targets. Conversely, a high threshold may preserve targets but dimin-

[8] We consider the beamwidth at $-3\,\mathrm{dB}$ of the array response as the angular resolution of target position estimation.

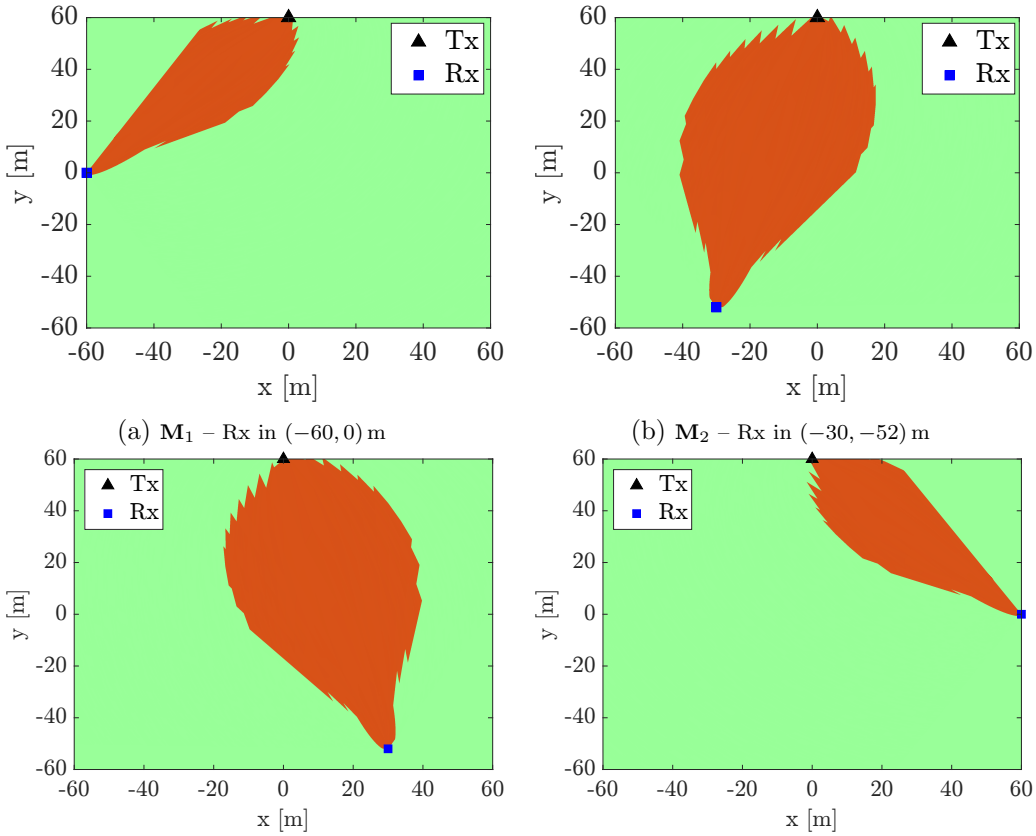

(a) $\mathbf{M}_1$ – Rx in $(-60, 0)$ m

(b) $\mathbf{M}_2$ – Rx in $(-30, -52)$ m

(c) $\mathbf{M}_3$ – Rx in $(30, -52)$ m

(d) $\mathbf{M}_4$ – Rx in $(60, 0)$ m

Figure 5.3: Example of reliability maps $\mathbf{M}_i$ for $i = 1, \ldots, 4$ with Tx located in $(0, 60)$ m obtained with $\gamma_{\text{res}} = 5\,\text{m}^2$. Orange pixels correspond to 0 and green ones to 1.

ish the advantage of fusing only the most informative regions of the likelihood maps that lead to better performance, as explained in the following section and corroborated in the numerical results.

5.3.4 Dynamic Role Rotation for Multi-View Perception

Upon completion of a scan in a given network configuration $\mathcal{S}_t$ with the tth BS as Tx, the system transitions to maintain an uninterrupted scanning process. The Tx role cycles through all BSs in a round robin fashion, ensuring that each BS periodically transmits, following the sequence $\mathcal{S}_1 \rightarrow \mathcal{S}_2 \rightarrow \cdots \rightarrow \mathcal{S}_{|\mathcal{S}|} \rightarrow \mathcal{S}_1 \ldots$. This strategy leverages the network's cooperative capabilities

and exploits spatial diversity to enhance target perception from multiple viewpoints. This is particularly advantageous for detecting and estimating multiple extended targets, as occluded sections may become visible from different perspectives.

It is worth noting that, as the Tx role rotates, the bistatic Tx-Rx pair configurations are updated. Thus, each Rx must select the proper reliability map, taking into account the updated Tx position and bistatic configuration. Furthermore, while dynamic role switching among BSs is key to enriching bistatic sensing diversity during the search phase, care must be taken to prevent disruption of communication services. Rapid beam reconfiguration and tight synchronization are required to avoid service degradation, especially when the transmitting BS is also handling user traffic. Techniques such as partial role rotation, scheduling sensing in low-traffic periods, and limiting the sensing duration can mitigate these effects.

5.3.5 Fusion of Range-Angle Maps

Each receiver operates within its own reference system, where the origin $\mathbf{O}$ is located at the position of the Rx itself $\mathbf{s}_i = [s_{\mathrm{x},i}, s_{\mathrm{y},i}]^{\mathsf{T}}$. To fuse the range-angle maps from all Rxs into a common global coordinate system, we must at first transform each map from the local coordinates of the Rx to global coordinates. Let (x, y) represent the coordinates of a point in the range-angle map in the local reference frame of the receiver. The corresponding coordinates (x', y') in the global coordinate system, with origin $\mathbf{O}'$ in the center of the area of interest, are given by $[x'\,, y']^{\mathsf{T}} = \mathbf{R}_\alpha\,[x\,, y]^{\mathsf{T}} + \mathbf{s}_i$, where $\mathbf{R}_\alpha$ is the rotation matrix that aligns the local reference frame with the global one and α is the counterclockwise rotation angle of the ith local reference system with respect to the global one. Then, the area of interest is divided into $R_\mathrm{x} \times R_\mathrm{y}$ grid cells, each of size $\delta\mathrm{x} \times \delta\mathrm{y}$, represented by the indices $(g_\mathrm{x}, g_\mathrm{y})$.

Each local map is resampled using a linear interpolation method, ensuring that all data aligns correctly for accurate fusion. The interpolation is performed only within the regions of the map that passed the threshold test in (5.20) and that are not masked by the reliability map, while the remaining areas are obscured to prevent erroneous interpolation in regions without

data. We indicate such resampled maps as $\mathbf{\Pi}_i \in \mathbb{R}^{R_\mathrm{x} \times R_\mathrm{y}}$ and, with a slight abuse of terminology, we continue to refer to these matrices as range-angle maps. Now that each weighted (masked) range-angle map is in the global coordinate system, we can perform the fusion of the maps obtained at each Rx.[9] Precisely, the FC collects the $|\mathcal{S}| - 1$ range-angle maps in a given multistatic configuration $\mathcal{S}_t$ and fuses them to create a "soft map"

$$\mathbf{\Psi}_t = \sum_{i=1}^{|\mathcal{S}|-1} \mathbf{\Pi}_i. \tag{5.29}$$

Finally, to get a more comprehensive view of the surveilled area, we illuminate the scenario from $|\mathcal{S}|$ viewpoints, as each BS in the network must act as a Tx once in a scan cycle. Once all $|\mathcal{S}|$ soft maps are collected, the FC proceeds to integrate all the information into an aggregated map

$$\overline{\mathbf{\Psi}} = \sum_{t=1}^{|\mathcal{S}|} \mathbf{\Psi}_t \,. \tag{5.30}$$

This aggregated map can now be processed by clustering to perform multiple target detection and estimation. It is worth noting that, while decentralized fusion can reduce overhead by processing data locally at each base station, our system requires centralized collection of range-angle maps at the FC to maintain a global view of the scene and accurately associate measurements across bistatic pairs. The selective data fusion strategy and in-sensor thresholding described in previous sections are also applied to mitigate the raw data volume, achieving a trade-off between information retention and overhead reduction. Nevertheless, for accurate multi-target fusion, centralized processing remains essential.

[9] Note that, because the range-angle maps are formed via periodogram estimation, the performed fusion operation is non-coherent. This approach has the enormous benefit of not requiring tight or phase-level synchronization between BSs. However, when complexity is not an issue, coherent processing may also be performed [92].

5.3.6 DBSCAN Clustering for Detection and Estimation

In the search operating mode, clustering is employed to detect targets from the aggregated map. As an initial step, an excision filter is applied to the matrix $\overline{\mathbf{\Psi}}$ to filter out those elements of the map that are likely due to noise or clutter. Given the lack of prior knowledge regarding noise, number of targets and their feature, we adopt a scenario-dependent threshold. Precisely, we first determine the peak value of the current aggregated map and use a fixed percentage of this peak value to establish the threshold γ. The threshold γ is thus defined as

$$\gamma = \gamma_{\mathrm{d}} \cdot \max_{(g_x, g_y)} \left\{ [\overline{\mathbf{\Psi}}]_{g_x, g_y} \right\} \tag{5.31}$$

where γ_{d} represents the fixed percentage with respect to the peak value. Thresholding corresponds to ignoring the entries of the aggregated map below the threshold γ. After thresholding, the remaining points are weighted based on their intensity. Specifically, the aggregated map amplitude is quantized into discrete levels, defined as

$$\ell(g_x, g_y) = \left\lfloor \frac{[\overline{\mathbf{\Psi}}]_{g_x, g_y} - \min(\overline{\mathbf{\Psi}})}{\max(\overline{\mathbf{\Psi}}) - \min(\overline{\mathbf{\Psi}})} \cdot L_{\max} \right\rfloor, \tag{5.32}$$

where $\ell(g_x, g_y)$ represents the level assigned to the point at coordinates (g_x, g_y), $L_{\max}$ is the maximum number of quantization levels, and $[\overline{\mathbf{\Psi}}]_{g_x, g_y}$ is the amplitude of the aggregated map at the corresponding point. Points are then replicated as many times as their assigned level $\ell(g_x, g_y)$, ensuring that higher-intensity points contribute more prominently to the clustering process, thus improving the detectability of smaller targets. Then, a DBSCAN algorithm is employed to perform clustering. This algorithm specifies a maximum distance ξ_{d} for points to be considered part of the same cluster $\mathcal{C}_n$, as well as a minimum number of points, denoted as N_{d}, required to form a cluster (as described in [68]). Finally, target estimation is conducted by calculating the weighted mean of each cluster based on the amplitude in the aggregated map of the corresponding points. The weighted mean $\hat{\mathbf{z}}_n$ of

cluster n is given by

$$\hat{\mathbf{z}}_n = \frac{\sum_{\ell \in \mathcal{C}_n} A_\ell \mathbf{p}_\ell}{\sum_{\ell \in \mathcal{C}_n} A_\ell} \tag{5.33}$$

where $\mathbf{p}_\ell = (p_{\mathrm{x},\ell}, p_{\mathrm{y},\ell})$ are the positions of the points in cluster $\mathcal{C}_n$ and $A_\ell = [\overline{\mathbf{\Psi}}]_{p_{\mathrm{x},\ell}, p_{\mathrm{y},\ell}}$ are the corresponding amplitudes in the aggregated map. These position estimations are collected in the set $\widehat{\mathcal{Z}} = \{\hat{\mathbf{z}}_1, \hat{\mathbf{z}}_2, \dots\}$, which represents the target detections extracted from the aggregated map.

The set $\widehat{\mathcal{Z}}$ is then passed to tracking as the initial conditions for the tracking phase; the number of targets detected is $\widehat{Q} = |\widehat{\mathcal{Z}}|$.

5.4 Tracking Phase

In addition to the search operating mode, we designed the system to operate also in tracking mode. However, since the study of tracking algorithms is outside the scope of this paper, we assume that the system is operating in the steady-state regime of a generic tracking algorithm, bypassing the transient phase. Specifically, the target's position is assumed to be estimated via tracking with some uncertainty, modeled as a noisy measurement following, e.g., a bivariate normal distribution; details will be provided in the numerical results. Now, the $\widehat{Q}$ estimated targets are each characterized by the tow parameters: $\widehat{\phi}_q$ and $\widehat{\theta}_q$. The misalignment between the estimated and actual target parameters is considered in the factor $|\gamma(\phi_q)|^2$ of (5.8), where the impact of these estimation errors on system performance is evaluated.

5.4.1 Transmitted and Received Signals

In the tracking mode, the first operation at the Tx is to perform precoding using a beamforming vector $\mathbf{w}_\mathrm{T}$, with the goal of generating a multibeam radiation pattern. This approach enables the system to allocate the appropriate fractions of the available power to communication and sensing, allowing the transmitted signals to effectively serve both purposes. The beamforming vector $\mathbf{w}_\mathrm{T}$ is defined as

$$\mathbf{w}_\mathrm{T} = \sqrt{\rho_\mathrm{p}}\, \mathbf{w}_{\mathrm{T,s}} + \sqrt{1 - \rho_\mathrm{p}}\, \mathbf{w}_{\mathrm{T,c}}, \tag{5.34}$$

where $\rho_{\mathrm{p}} \in [0,1]$ determines the portion of power apportioned to sensing. The vectors $\mathbf{w}_{\mathrm{T,s}}$ and $\mathbf{w}_{\mathrm{T,c}}$ represent the beamforming weights for sensing and communication, respectively.

For communication, we start with defining the beam steering vector $\tilde{\mathbf{w}}_{\mathrm{T,c}} = \mathbf{a}^{\mathsf{c}}(\theta_{\mathrm{T,c}})/\|\mathbf{a}^{\mathsf{c}}(\theta_{\mathrm{T,c}})\|_2$, which is designed to maximize gain in the desired communication direction $\theta_{\mathrm{T,c}}$. Subsequently, sidelobe suppression is achieved by element-wise multiplying the communication beamforming vector $\tilde{\mathbf{w}}_{\mathrm{T,c}}$ with the window weight vector $\mathbf{c}$, resulting in the final beamforming vector $\mathbf{w}_{\mathrm{T,c}} = \sqrt{P_{\mathrm{avg}}}\tilde{\mathbf{w}}_{\mathrm{T,c}} \odot \mathbf{c}$, where $\mathbf{c}$ is normalized to ensure $\|\mathbf{w}_{\mathrm{T,c}}\|_2^2 = P_{\mathrm{avg}}$.

For sensing, the beamwidth of the radiation pattern at both Tx and Rx is determined separately for each target in the scenario based on the angular extent of its corresponding square region of interest (RoI), centered on the estimated target position. This ensures that the entire RoI is illuminated, increasing the likelihood of covering the target even in the presence of localization uncertainty. Without this adaptation, the highly directional beam—designed with sidelobe suppression—might fail to illuminate the target. The required beamwidth varies for each target depending on the RoI's proximity to the BS: closer regions require wider beams, while farther ones approach the theoretical limit $\delta\theta$ imposed by beam steering. Since Tx and Rx are not co-located, their different perspectives on both the target and its RoI result in distinct beamwidth adaptations. The size of the RoI is chosen to account for the worst-case target localization accuracy from the search phase, ensuring that the beamforming strategy remains robust to potential estimation errors. Therefore, beamforming for sensing is designed to generate multiple beams, each directed towards a tracked target with DoD $\widehat{\phi}_q$. Following the approach in [77], the transmit beamforming vector is given by $\mathbf{w}_{\mathrm{T,s}} = \sqrt{P_{\mathrm{avg}}/\widehat{Q}}\sum_{q=0}^{\widehat{Q}-1} \tilde{\mathbf{w}}_{\mathrm{T},q}$, where $\tilde{\mathbf{w}}_{\mathrm{T},q}$ represents a unit-norm beamforming vector designed to provide nearly constant gain across the corresponding RoI, ensuring $\|\mathbf{w}_{\mathrm{T,s}}\|_2^2 = P_{\mathrm{avg}}$. To accommodate multiple targets, the transmit power is evenly distributed by scaling the beamforming vector by $\sqrt{\widehat{Q}}$, where $\widehat{Q}$ is the number of beams. Similarly, spatial combining at the Rx i is performed over each DoA $\widehat{\theta}_{q,i}$ by using the receiving beamforming vector $\mathbf{w}_{\mathrm{R},i} = \left(1/\sqrt{\widehat{Q}}\right)\sum_{q=0}^{\widehat{Q}-1} \tilde{\mathbf{w}}_{\mathrm{R},i,q}$, where $\tilde{\mathbf{w}}_{\mathrm{R},i,q}$ is the unit-norm beamforming vector ensuring a consistent gain over the designated RoI, with $\|\mathbf{w}_{\mathrm{R}}\|_2^2 = 1$.

As for the search phase, during tracking a Dolph-Chebyshev window with a 30 dB peak-to-sidelobe ratio is employed, providing effective suppression of sidelobes. An example of the resulting radiation pattern, showing multiple beams during tracking, is illustrated in Fig. 5.2 in green.

It is worth noting that the durations of the search and tracking phases are inherently asymmetric and dynamically scheduled. As previously stated, in the proposed implementation, the search phase time is at least $T_{\text{search}} = MT_{\text{s}} \cdot |\mathcal{S}|$, corresponding to the total time required for each BS to cyclically act as Tx while the others receive, ensuring multi-view bistatic coverage of the scene. Once the initial target locations are estimated, the system enters the tracking phase, which adopts a reduced sensing strategy without multi-view diversity and thus requires only $T_{\text{track}} = MT_{\text{s}}$ of OFDM signal transmission to perform sensing. The system remains in the tracking phase for a configurable amount of time to continuously monitor target evolution with low overhead. When scene changes are expected—such as the appearance of new targets or disappearance of existing ones—the system switches back to the search phase to refresh the situational awareness. The unequal durations of the two phases are intentional and beneficial: they allow the system to operate efficiently by alternating between high-resolution discovery and low-overhead monitoring.

5.4.2 Soft Maps

Here, starting from the periodogram estimation in (5.12), we first compute the mean across the Doppler frequencies to extract the range profile $\mathbf{r}_i = (P_i(1), \ldots, P_i(K_{\text{p},i}))^{\mathsf{T}}$ with

$$P_i(l) = \frac{1}{M_{\text{p}}} \sum_{p=0}^{M_{\text{p}}-1} \mathcal{P}_i(l,p)\,. \tag{5.35}$$

This way, we exploit processing gain via averaging while discarding information about target velocities. Moreover, unlike the search mode, where only the maximum peak of the periodogram is retained, here the mean operation preserves the information of all targets since, in the tracking mode, we illuminate each target with a specific beam rather than scanning the entire environment. The resulting vector obtained at each Rx, $\mathbf{r}_i$, of dimension

$K_{\mathrm{p,i}} \times 1$, is then delivered to the FC without any further in-sensor processing [39, 41].

Exploiting the above soft information, the FC generates a score map $\mathbf{S}$ of the surveillance area through a cell scoring (or *cell voting*) process. Accordingly, the area is divided into $N_{\mathrm{x}} \times N_{\mathrm{y}}$ grid cells, each of size $\Delta\mathrm{x} \times \Delta\mathrm{y}$ represented by indexes $(n_{\mathrm{x}}, n_{\mathrm{y}})$. Each element $P_i(l)$ scores one or multiple grid cells, as follows. We denote by $\tau_i(l)$ the ToA corresponding to the element $P_i(l)$. In a multistatic network, a sample $P_i(l)$ scores all cells that are crossed by an ellipse with equation (5.1) and major axis $c\tau_i(l) = R_{\mathrm{bis},i}(l)$. The "amplitude" of the ellipse associated with the lth element of $\mathbf{r}_i$ is first evaluated as

$$V_i(l) = \frac{P_i(l)}{\frac{1}{K_{\mathrm{p,i}}} \sum_{l=1}^{K_{\mathrm{p,i}}} P_i(l)}, \tag{5.36}$$

thereby obtaining a total of $K_{\mathrm{p,i}}$ ellipses from each sensor. Then, the scoring process is performed, where the score obtained by each of the $N_{\mathrm{x}} \times N_{\mathrm{y}}$ grid cells is defined as

$$S_i(n_{\mathrm{x}}, n_{\mathrm{y}}) = \max_{l=1,\ldots,K_{\mathrm{p,i}}} V_i(l) I(l, n_{\mathrm{x}}, n_{\mathrm{y}}). \tag{5.37}$$

In (5.37), the element $I(l, n_{\mathrm{x}}, n_{\mathrm{y}})$ equals 1 if the lth ellipse passes through the grid cell $(n_{\mathrm{x}}, n_{\mathrm{y}})$, and 0 otherwise. Depending on the bistatic range resolution of the Rx node and on the dimension $\Delta\mathrm{x} \times \Delta\mathrm{y}$ of the grid cells, one cell may, in principle, be scored by several ellipses; in light of this, according to (5.37), only the largest received score by the grid cell is counted as its final score. Finally, one score map $\mathbf{S}_i$ is obtained for each Tx-Rx pair.

The score maps $\mathbf{S}_i$ produced from all Rxs are fused, in a non-coherent manner, to construct an overall score map.

$$\Sigma(n_{\mathrm{x}}, n_{\mathrm{y}}) = \prod_{i=1}^{|\mathcal{S}|} S_i(n_{\mathrm{x}}, n_{\mathrm{y}}). \tag{5.38}$$

In case a point-like target is present in the scenario ($\widehat{Q} = 1$), from the fusion of the soft bi-dimensional maps obtained for each Tx-Rx pair in the surveillance area, the location of the peak in (5.38) returns the estimated position of the

target as

$$\hat{\mathbf{z}} = (\hat{z}_{\mathrm{x}}, \hat{z}_{\mathrm{y}}) = \underset{(i_x, i_y)}{\arg\max} \left\{ [\boldsymbol{\Sigma}]_{i_{\mathrm{x}}, i_{\mathrm{y}}} \right\}. \tag{5.39}$$

5.4.3 Clustering and Estimation of Multiple Targets

When multiple targets are present in the scenario, the estimated positions cannot be obtained using (5.39). Rather, a clustering algorithm is necessary to identify multiple targets from the overall score map $\boldsymbol{\Sigma}$. In the tracking operating mode, since the system has prior knowledge of the number of targets from previous detections, a k-nearest neighbors (k-NN) algorithm with $k = 1$ is employed. This approach leverages the known target positions from earlier time instants to enhance clustering accuracy, unlike in the search mode, where the number of clusters is unknown and needs to be estimated. The clustering process uses a gating parameter ξ_{NN} to group points that are likely associated with the previously detected targets into a set of clusters [93]. Once clustering is performed, each cluster's centroid, representing an estimated target position, is calculated. To accurately estimate the positions of the targets, we compute the weighted mean of the points within each cluster. The weighted mean $\hat{\mathbf{z}}_n$ of the nth cluster $\mathcal{C}_n$ is calculated using the amplitudes of the points within the cluster, which are derived from the fused map, as

$$\hat{\mathbf{z}}_n = \frac{\sum_{\ell \in \mathcal{C}_n} A_\ell \mathbf{p}_\ell}{\sum_{\ell \in \mathcal{C}_n} A_\ell}. \tag{5.40}$$

Here, $\mathbf{p}_\ell = (p_{\mathrm{x},\ell}, p_{\mathrm{y},\ell})$ represents the position of the point within cluster $\mathcal{C}_n$, and $A_\ell = [\boldsymbol{\Sigma}]_{p_{\mathrm{x},\ell}, p_{\mathrm{y},\ell}}$ denotes the corresponding amplitude in the overall score map $\boldsymbol{\Sigma}$.

This weighted mean approach ensures that points with higher amplitudes have a greater influence on the estimated target position, thus yielding a more accurate location estimate. These position estimates are then stored in the set $\widehat{\mathcal{Z}}$ of target position estimates. It is worth highlighting that, unlike during the search phase, the number of clusters in this operational mode is predetermined based on the number of targets identified during the search phase.

5.5 Numerical Results

5.5.1 System and Scenario Parameters

Numerical simulations are conducted to evaluate the performance of the proposed multistatic JSC system. The system's main parameters, shared by all BSs are summarized in Table 5.1. For the angular coverage, the scanning angle at the BS is set to $\theta_0 = 58.8°$, ensuring an angular aperture of 120° with a beamwidth of $\delta\theta = 2.4°$. At each Rx, $M = 336$ OFDM symbols, modulated with a QPSK alphabet, are collected. Additionally, the target RCS is modeled following a Swerling I distribution with average value $\bar{\sigma}_{\text{rcs}}$. The noise PSD is calculated as $N_0 = k_{\text{B}} T_0 F$, where $T_0 = 290\,\text{K}$ is the reference temperature, $F = 13\,\text{dB}$ is the receiver noise figure, and $k_{\text{B}} = 1.38 \times 10^{-23}\,\text{JK}^{-1}$ is the Boltzmann constant. A square surveillance area of $120\,\text{m} \times 120\,\text{m}$ is monitored by the multistatic MIMO system with $|\mathcal{S}| = 5$ BSs, located at $(0\,\text{m}, 60\,\text{m})$,$(-60\,\text{m}, 0\,\text{m})$, $(-30\,\text{m}, -52\,\text{m})$, $(30\,\text{m}, -52\,\text{m})$, and $(60\,\text{m}, 0\,\text{m})$, respectively. Targets are randomly generated, at each Monte Carlo iteration, with a uniform distribution within a square area of $70\,\text{m} \times 70\,\text{m}$, centered at the origin of the surveillance area, ensuring that they remain within the field of view of all BSs. To ensure a more realistic simulation, the spatial distribution of targets is considered. A minimum separation of 1 meter is enforced to prevent overlap. Each target moves with velocity $\mathbf{v} = (v_{\text{x}}, v_{\text{y}})$, where each component of the velocity is drawn from a uniform distribution ranging from $-20\,\text{m/s}$ to $20\,\text{m/s}$. Additionally, we account for clutter in the surveillance area by generating $\mathcal{L} = 25$ clutter points, uniformly distributed within the same area of interest as the targets. Unlike the targets, all clutter points are static, representing ground clutter, and therefore have zero velocity. Furthermore, the clutter points remain fixed across all Monte Carlo iterations. The performance of the multistatic JSC system is evaluated in both the search and tracking modes, as follows.

Search Mode: In this mode, the BSs scan the environment to detect new targets and eliminate those that are no longer present. Each BS takes turns acting as the Tx until the completion of all scan cycles. The resampled maps $\mathbf{\Pi}$ generated by each BS in receiving mode during each scan cycle cover the

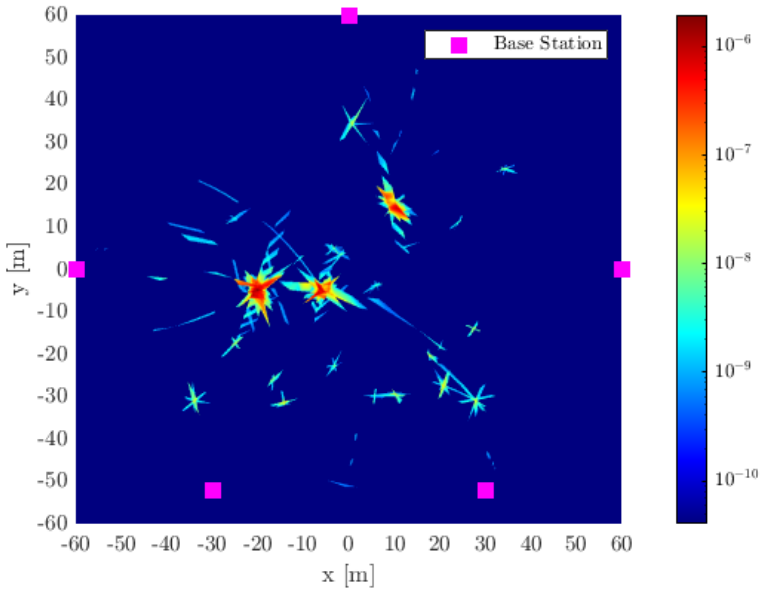

Figure 5.4: Example of aggregated map computed according to (5.30). Each BS acts as Tx once in a round-robin fashion.

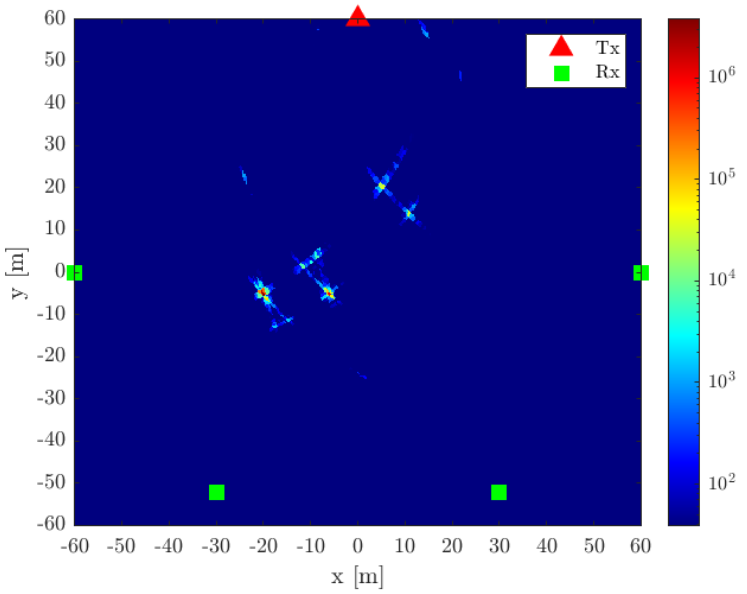

Figure 5.5: Example of overall score map computed according to (5.38).

entire surveillance area, with $R_{\mathrm{x}} = R_{\mathrm{y}} = 701$ grid points and a resolution of $\delta\mathrm{x} = \delta\mathrm{y} = 0.1\,\mathrm{m}$. An example of an aggregated map, generated using the metric in (5.30), is shown in Fig. 5.4, assuming three targets at positions $(-20\,\mathrm{m}, -5\,\mathrm{m})$, $(-6\,\mathrm{m}, -5\,\mathrm{m})$, and $(10\,\mathrm{m}, 15\,\mathrm{m})$, with velocities $(17, 19)$ [m/s], $(19, 13)$ [m/s], $(3, 2)$ [m/s], respectively.

Tracking Mode: In this mode, one BS is designated as the Tx, specifically the BS at $(0\,\mathrm{m}, 60\,\mathrm{m})$, while the others function as Rxs until the search mode is reactivated. Under the assumption that the number of targets and their positions at previous time instants are known, a characteristic feature of common tracking algorithms, the sensors in the system use prior estimates of the targets' DoD and DoA to align the sensing beams with the targets. This alignment ensures that the sensing beams directly illuminate the targets. However, since implementing a tracking algorithm was beyond the scope of this work, we simulated the effect of tracking errors in the clustering algorithm. Instead of using the exact previous positions, we introduced Gaussian noise to these estimates. The noise was modeled as $\mathcal{N}(0, \sigma^2)$ with $\sigma^2 = 1\,\mathrm{m}^2$, simulating the uncertainty in the target positions. Finally, in this tracking mode, the soft maps generated by each sensor cover the entire surveillance area with $N_{\mathrm{x}} = N_{\mathrm{y}} = 401$ grid points and a resolution of $\Delta\mathrm{x} = \Delta\mathrm{y} = 0.3\,\mathrm{m}$. Unless otherwise specified, the fraction of power allocated to the sensing beam is $\rho_{\mathrm{p}} = 0.1$, meaning that 90% of the power is allocated to the communication beam. Using the same scenario as in Fig. 5.4, an example of a score map generated using the metric in (5.38) is shown in Fig. 5.5.

5.5.2 Performance Metrics

Given the complex scenario involving multiple point-like targets, the GOSPA metric is one of the metrics employed to assess the sensing performance of the network. The GOSPA metric is commonly used to evaluate tracking performance in multi-target or multi-scatterer environments because it integrates both localization accuracy and detection capability into a single metric, while accounting for false alarms and missed detections [71]. The p-order GOSPA metric, computed for each Monte Carlo iteration, follows (2.23). When the order parameter $p = 2$, the first term in (2.23), which represents the lo-

Table 5.1: System parameters

Base Station		
f_c	Center frequency	28 GHz
Δf	Subcarrier spacing	120 kHz
K	Active subcarriers	3168
M	Number of OFDM symbols	336
N_T	Number of transmitting antennas	50
N_R	Number of receiving antennas	50
$\lvert\mathcal{S}\rvert$	Number of base stations	5
T_{scan}	Scan duration	3 ms
T_{search}	Search mode duration	15 ms
$\delta\theta$	Beamwidth	2.4°
θ_0	Starting scan angle	58.8°
N_{dir}	Search scan directions	50
ρ_p	Fraction of power for sensing during tracking	0.1
ROI	Region of interest	9 m^2
Simulation Parameters		
$\delta x, \delta y$	Resampling grid resolution	0.1 m
$\Delta x, \Delta y$	Score map resolution	0.3 m
N_{MC}	Monte Carlo iterations	1000
γ_{res}	Area threshold	5 m^2
FAR	False Alarm Rate	10^{-2}
Clustering		
ξ_{NN}	Gate k-NN	3 m
γ_d	DBSCAN percentage threshold	5%
ξ_d	Gate DBSCAN	2 m
N_d	Minimum number of points DBSCAN	50
GOSPA Metric		
p	GOSPA order	2
ξ_g	GOSPA gate	5

calization error, can be interpreted as the mean squared error between the estimated and true target positions. By computing the average squared error over effectively assigned targets, the corresponding RMSE metric is obtained, defined as

$$\mathrm{RMSE} = \sqrt{\frac{1}{|\zeta_g|} \sum_{q=0}^{|\zeta_g|-1} (\zeta_{g,q} - \zeta^*_{g,q})^2} \tag{5.41}$$

where $\zeta_g \subseteq \mathcal{Z}$ is the subset of actual targets that are optimally assigned, and $\zeta^*_g \subseteq \hat{\mathcal{Z}}$ is the subset of estimated target that are optimally assigned.

The second term in (2.23) can be decomposed into

$$\frac{\xi_{\mathrm{g}}^{p}}{2}(|\mathcal{Z}| - |\zeta_{\mathrm{g}}^{*}|) + \frac{\xi_{\mathrm{g}}^{p}}{2}(|\hat{\mathcal{Z}}| - |\zeta_{\mathrm{g}}^{*}|)\,.$$

where the first component is proportional to the missed detection rate, R_{MD}, and hence the detection rate, R_{D}, while the second component corresponds to the false detection rate, R_{FD}. These rates are defined as

$$R_{\mathrm{D}} = \frac{|\zeta_{\mathrm{g}}^{*}|}{|\mathcal{Z}|}, \quad R_{\mathrm{FA}} = \frac{|\hat{\mathcal{Z}}| - |\zeta_{\mathrm{g}}^{*}|}{|\hat{\mathcal{Z}}|}, \quad R_{\mathrm{MD}} = 1 - R_{\mathrm{D}}.$$

In the tracking mode, where the number of estimated targets matches the number of actual targets (i.e., $|\mathcal{Z}| = |\zeta_{\mathrm{g}}^{*}|$) the GOSPA metric does not account for cardinality errors—arising from a mismatch in the number of estimated and true targets—but only for localization errors. Consequently, under these conditions, the GOSPA metric is functionally equivalent to the RMSE, as both measure localization accuracy without penalizing cardinality mismatches.

Note that in numerical simulations, all the metrics introduced above, including GOSPA and RMSE, have been averaged over the number of Monte Carlo iterations to ensure statistical reliability.

5.5.3 Search Phase Results

In Fig. 5.6 and Fig. 5.7, the system performance is shown as a function of the number of targets in the surveilled area during the search phase. Specifically, the GOSPA results show that as the transmitted power increases, the GOSPA error also increases, while the cardinality error remains consistent across the different cases. For this reason, to further investigate the system performance during the search phase, the results are presented in terms of RMSE. While GOSPA was introduced earlier and noted to coincide with RMSE when cardinality is correct, the number of targets is unknown during the search phase. Therefore, the RMSE in (5.41) is used here to provide a clearer measure of localization accuracy, offering a direct measure of localization performance. An unexpected trend is observed: performance degrades

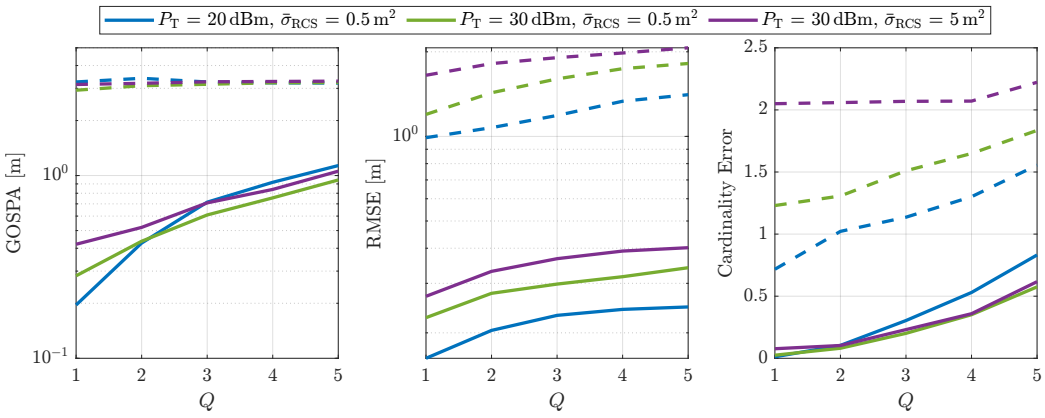

Figure 5.6: Results in the search phase showing the GOSPA, RMSE, and cardinality error as a function of the number of targets present in the surveilled area, obtained by averaging over the Monte Carlo iterations. Dashed lines represent performance results when reliability maps $\mathbf{M}$ are not applied.

as the transmitted power increases. This counterintuitive behavior can be attributed to the nature of the aggregated map in (5.30). At higher power levels, the map becomes more cluttered due to the accumulation of spurious detections and elongated target representations. This is caused by a misalignment between the actual direction of the target and the scanning directions, along with the presence of clutter. Targets near the baseline are particularly affected, as consecutive scanning directions tend to overlap, causing the targets to appear elongated in the aggregated map. To mitigate this issue, reliability maps are employed, as shown in Fig. 5.3. As clearly exemplified in Fig. 5.6, application of these maps helps reducing the impact of spurious detections substantially, improving overall performance. Nonetheless, higher transmitted power can still exacerbate map contamination, leading to a deterioration in performance. Additionally, results show a significant degradation in GOSPA performance for $P_T = 20$ dBm, primarily due to an increase in cardinality errors. This degradation arises from two factors: the noise threshold η used to filter each range-angle map and the DBSCAN clustering parameters. A high noise threshold may result in smaller clusters that the clustering algorithm fails to identify as targets, instead classifying them as outliers. Fig. 5.7 also illustrates that this degradation is linked to a lower acquisition rate, indicating that missed acquisitions, rather than false

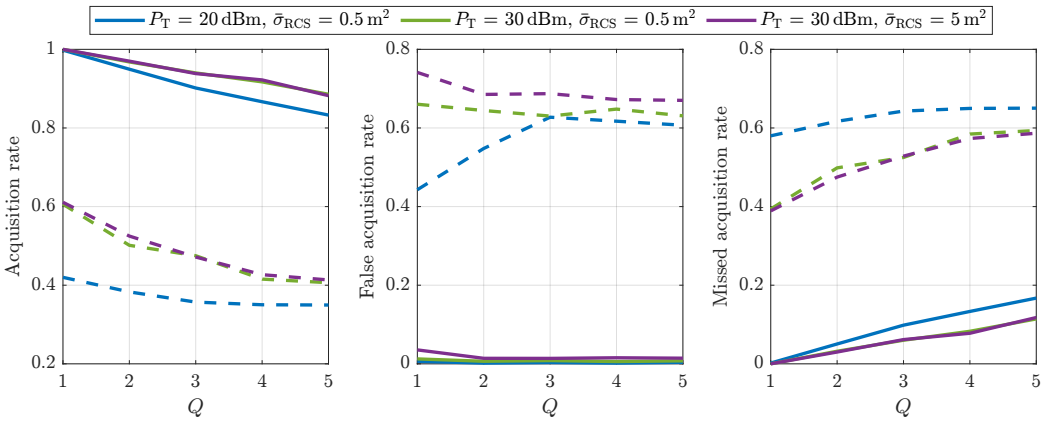

Figure 5.7: Results in the search phase showing the acquisition rate, false acquisition rate and missed detection rate as a function of the number of targets present in the surveilled area, obtained by averaging over the Monte Carlo iterations. Dashed lines represent performance results when reliability maps $\mathbf{M}$ are not applied.

alarms, are the primary cause. Again, it can be seen how application of the proposed reliability maps provides tangible performance benefits.

5.5.4 Tracking Phase Results

The performance of the multistatic system during the tracking phase is illustrated in Fig. 5.8. For this analysis, various configurations of P_T and average RCS $\bar{\sigma}_{rcs}$ have been considered. In this phase, knowledge of the number of targets and their approximate positions enables the multistatic system to localize the clusters more accurately within the map, thereby facilitating continuous tracking of the targets' locations. The spatial diversity achieved through beamforming in both transmission and reception plays a crucial role, allowing direct illumination of the targets. This leads to sub-meter level accuracy, representing a significant improvement over the search phase. Moreover, the spatial diversity provided by beamforming not only enhances localization accuracy but also reduces clutter effects, thereby improving overall system performance. This benefit becomes particularly evident under challenging conditions, such as those with high noise or clutter. This results in further performance gains, as demonstrated in Fig. 5.8, where the system's performance is analyzed under varying tracking algorithm accuracy. The analysis

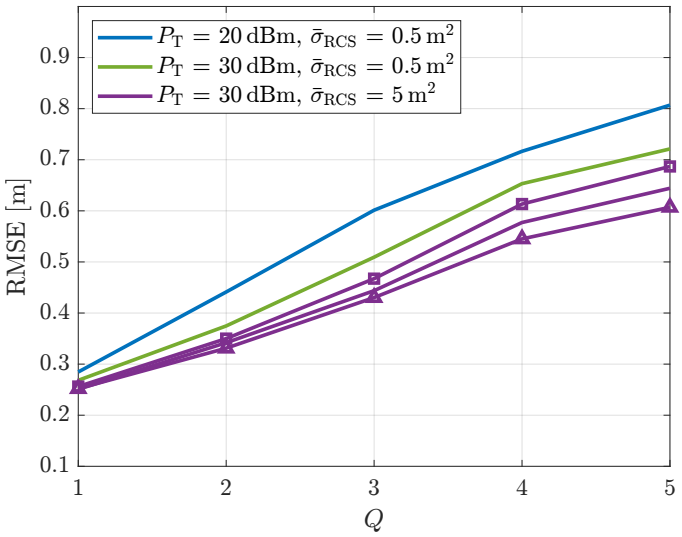

Figure 5.8: Sensing performance of the multistatic JSC system during the tracking phase as a function of the number of targets Q present in the scenario, considering a tracking algorithm error variance of $\sigma = 1\text{m}^2$. The curve with triangle markers corresponds to $\sigma = 0.5\text{m}^2$, while the curve with square markers corresponds to $\sigma = 1.5\text{m}^2$.

shows that the system achieves better performance as the accuracy of the tracking algorithm improves. Specifically, reducing the variance of the noise introduced in the simulated tracking algorithm leads to more accurate target localization and enhanced overall performance.

5.6 Conclusion

In this Chapter, we investigated a multistatic system based on OFDM signals, designed to operate in two distinct modes: search and tracking. In the search phase, the system leveraged the cooperation among multiple BS and employed range-angle maps to detect and localize targets. The performance analysis, presented through the GOSPA and RMSE metrics, revealed that the system's performance was influenced by the transmitted power and RCS. Interestingly, an increase in transmitted power resulted in increased GOSPA errors, primarily due to map contamination caused by clutter, spurious detections, and target elongation. However, the use of reliability maps effectively mitigated these spurious effects. Furthermore, cardinality errors

observed at lower power settings highlighted the importance of noise thresholding and DBSCAN clustering parameters, which impacted the acquisition rate. In the tracking phase, the system benefited from prior knowledge of target positions, enabling more precise localization. Spatial diversity, achieved through beamforming at both transmission and reception, played a critical role in improving localization accuracy and reducing clutter effects. This phase demonstrated sub-meter level accuracy and showed better performance under challenging conditions, such as high noise or clutter. The performance improvement was particularly significant when the tracking algorithm's accuracy was enhanced by reducing the noise variance.

Conclusion and Future Directions

This thesis has presented a comprehensive exploration of JSC systems within the framework of 5G and beyond, leveraging monostatic, bistatic, and multistatic configurations for cooperative target detection and localization. The findings highlight the significant potential of integrating sensing capabilities into mobile communication networks, with particular emphasis on system performance under various configurations and operational scenarios. In the monostatic case, the proposed framework demonstrated the ability to seamlessly integrate OFDM-based communication systems with cooperative sensing across multiple BSs. By fusing soft range-angle maps at a FC and employing resource management strategies, sub-2-meter localization accuracy was achieved for both extended and point-like targets. Notably, these results were obtained while maintaining a downlink communication capacity exceeding 1.3 Gbit/s, emphasizing the feasibility of JSC for dual-purpose networks. In the bistatic configuration, the adaptability of 5G NR waveforms for sensing applications was confirmed. Under LOS conditions, high localization accuracy was obtained; however, DoA estimation emerged as the primary limitation, with performance influenced also by blind zones and narrow-bandwidth numerologies. Despite these challenges, the system maintained coverage exceeding 70% for baselines up to 100 m. For multistatic systems, bothMISO and MIMO architectures were examined. In MISO setups, soft map fusion was shown to outperform LS localization, particularly when sensing resources were constrained. This approach also addressed the blind zone issues inherent in bistatic setups, resulting in improved coverage and reliability. MIMO systems further advanced the sensing capabilities by

employing dual modes of operation—search and tracking. The search phase leveraged cooperative detection using range-angle maps, while the tracking phase capitalized on spatial diversity and beamforming to achieve sub-meter localization accuracy, even under challenging conditions such as high clutter or noise. Across all configurations, the interplay between sensing resource allocation, noise thresholding, and clustering parameters was pivotal in balancing communication and sensing performance. The use of reliability maps and clustering techniques like DBSCAN emerged as essential tools to mitigate the effects of clutter, spurious detections, and target elongation, particularly in high-power scenarios. Importantly, results were directly compared with a monostatic baseline, demonstrating that bistatic configurations can enhance sensing coverage relative to the monostatic case.

In conclusion, this thesis underscores the transformative potential of integrating JSC into 5G networks, showcasing solutions for overcoming key challenges such as blind zones, clutter, and resource constraints. The results provide a solid foundation for future advancements in JSC technologies, paving the way for enhanced situational awareness in applications ranging from autonomous systems to smart city infrastructures. In particular, moving beyond fixed power allocation, future studies should develop adaptive schemes that leverage real-time channel and traffic conditions. Reinforcement learning or optimization algorithms could dynamically reassign transmit power, particularly for BSs idle in either communication or sensing tasks, to optimize the trade-off between sensing accuracy and communication quality. In scenarios where Tx and Rx are not fixed—such as vehicle-to-everything (V2X), V2V, or UE sensing—adaptive beamforming and beam tracking techniques can mitigate alignment errors and signal fluctuations, improving coverage and robustness in dynamic environments. As sensors become mobile, synchronization errors and time-varying multipath correlations present significant challenges. Future work should investigate joint synchronization-refinement algorithms and multipath-aware fusion methods to ensure coherent processing across distributed, moving nodes. Finally, beyond classical map fusion and DBSCAN, advanced machine learning models—such as graph neural networks or deep multi-sensor tracking frameworks—could adaptively learn complex target and clutter dynamics, enhancing tracking fidelity in non-

stationary environments.

By pursuing these avenues, future JSC systems are poised to further bridge the gap between communication and sensing functionalities, enabling fully integrated networks with heightened situational awareness for applications spanning autonomous platforms, smart-city deployments, and beyond.

List of Figures

Bibliography

[1] S. Bartoletti, Z. Liu, M. Z. Win, and A. Conti, "Device-free localization of multiple targets in cluttered environments," *IEEE Trans. Aerosp. Electron. Syst.*, vol. 58, pp. 3906–3923, Oct. 2022.

[2] F. Liu, Y. Cui, C. Masouros, J. Xu, T. X. Han, Y. C. Eldar, and S. Buzzi, "Integrated sensing and communications: Towards dual-functional wireless networks for 6G and beyond," *preprint, arXiv:2108.07165*, 2021.

[3] R. Li, Z. Xiao, and Y. Zeng, "Toward seamless sensing coverage for cellular multi-static integrated sensing and communication," *IEEE Trans. Wireless Commun.*, vol. 23, pp. 5363–5376, June 2024.

[4] R. Thomä, T. Dallmann, S. Jovanoska, P. Knott, and A. Schmeink, "Joint communication and radar sensing: An overview," in *Europ. Conf. on Ant. and Prop. (EuCAP)*, (Dusseldorf, Germany), pp. 1–5, Mar. 2021.

[5] S. Schieler, C. Schneider, C. Andrich, M. Döbereiner, J. Luo, A. Schwind, R. S. Thomä, and G. Del Galdo, "OFDM waveform for distributed radar sensing in automotive scenarios," *Int. J. of Microw. and Wireless Tech.*, vol. 12, p. 716–722, Oct. 2020.

[6] F. Liu, C. Masouros, A. P. Petropulu, H. Griffiths, and L. Hanzo, "Joint radar and communication design: Applications, state-of-the-art, and the road ahead," *IEEE Trans. Commun.*, vol. 68, pp. 3834–3862, Feb. 2020.

[7] S. D. Liyanaarachchi, C. Baquero B., T. Riihonen, M. Heino, and M. Valkama, "Joint multi-user communication and MIMO radar

through full-duplex hybrid beamforming," in *Proc. IEEE Int. Symp. on Joint Comm. & Sensing (JCS)*, (online), pp. 1–5, Feb. 2021.

[8] F. Liu, Y. Cui, C. Masouros, J. Xu, T. X. Han, Y. C. Eldar, and S. Buzzi, "Integrated sensing and communications: Toward dual-functional wireless networks for 6G and beyond," *IEEE J. Sel. Areas Commun.*, vol. 40, pp. 1728–1767, June 2022.

[9] G. Kwon, Z. Liu, A. Conti, H. Park, and M. Z. Win, "Integrated localization and communication for efficient millimeter wave networks," *IEEE J. Sel. Areas Commun.*, vol. 41, Dec. 2023.

[10] T. Wild, V. Braun, and H. Viswanathan, "Joint design of communication and sensing for beyond 5G and 6G systems," *IEEE Access*, vol. 9, pp. 30845–30857, Feb. 2021.

[11] X. Liu, T. Huang, Y. Liu, and J. Zhou, "Joint transmit beamforming for multiuser mimo communication and mimo radar," in *Proc. IEEE International Conference on Signal, Information and Data Processing (ICSIDP)*, pp. 1–6, 2019.

[12] J. A. Zhang, F. Liu, C. Masouros, R. W. Heath, Z. Feng, L. Zheng, and A. Petropulu, "An overview of signal processing techniques for joint communication and radar sensing," *IEEE J. Sel. Topics Signal Process.*, vol. 15, pp. 1295–1315, Nov. 2021.

[13] Z. Xiao and Y. Zeng, "Waveform design and performance analysis for full-duplex integrated sensing and communication," *IEEE J. Sel. Areas Commun.*, vol. 40, pp. 1823–1837, June 2022.

[14] N. C. Luong, X. Lu, D. T. Hoang, D. Niyato, and D. I. Kim, "Radio resource management in joint radar and communication: A comprehensive survey," *IEEE Commun. Surveys Tuts.*, vol. 23, pp. 780–814, 2nd quarter 2021.

[15] J. A. Zhang, F. Liu, C. Masouros, R. W. Heath, Z. Feng, L. Zheng, and A. Petropulu, "An overview of signal processing techniques for joint

communication and radar sensing," *IEEE J. Sel. Topics Signal Process.*, vol. 15, pp. 1295–1315, Nov. 2021.

[16] F. Liu, Y. Cui, C. Masouros, J. Xu, T. X. Han, Y. C. Eldar, and S. Buzzi, "Integrated sensing and communications: Toward dual-functional wireless networks for 6G and beyond," *IEEE J. Sel. Areas Commun.*, vol. 40, no. 6, pp. 1728–1767, 2022.

[17] L. Zheng, M. Lops, Y. C. Eldar, and X. Wang, "Radar and communication coexistence: An overview: A review of recent methods," *IEEE Signal Processing Magazine*, vol. 36, no. 5, pp. 85–99, 2019.

[18] M. Braun, *OFDM radar algorithms in mobile communication networks*. PhD thesis, Karlsruhe Institute of Technology, 2014.

[19] C. Sturm and W. Wiesbeck, "Waveform design and signal processing aspects for fusion of wireless communications and radar sensing," *Proc. IEEE*, vol. 99, pp. 1236–1259, July 2011.

[20] C. B. Barneto, T. Riihonen, M. Turunen, L. Anttila, M. Fleischer, K. Stadius, J. Ryynänen, and M. Valkama, "Full-duplex OFDM radar with LTE and 5G NR waveforms: challenges, solutions, and measurements," *IEEE Trans. Microw. Theory Techn.*, vol. 67, pp. 4042–4054, Oct. 2019.

[21] K. V. Mishra, M. Bhavani Shankar, V. Koivunen, B. Ottersten, and S. A. Vorobyov, "Toward millimeter-wave joint radar communications: A signal processing perspective," *IEEE Signal Process. Mag.*, vol. 36, no. 5, pp. 100–114, 2019.

[22] J. A. Zhang, X. Huang, Y. J. Guo, J. Yuan, and R. W. Heath, "Multibeam for joint communication and radar sensing using steerable analog antenna arrays," *IEEE Trans. Veh. Technol.*, vol. 68, pp. 671–685, Jan. 2019.

[23] J. A. Zhang, A. Cantoni, X. Huang, Y. J. Guo, and R. W. Heath, "Joint communications and sensing using two steerable analog antenna arrays,"

in *2017 IEEE 85th Vehicular Technology Conference (VTC Spring)*, (Sydney, NSW, Australia), pp. 1–5, June 2017.

[24] C. B. Barneto, S. D. Liyanaarachchi, T. Riihonen, L. Anttila, and M. Valkama, "Multibeam design for joint communication and sensing in 5G New Radio networks," in *Proc. IEEE Int. Conf. on Comm. (ICC)*, (online), pp. 1–6, June 2020.

[25] S. Noh, M. D. Zoltowski, and D. J. Love, "Multi-resolution codebook and adaptive beamforming sequence design for millimeter wave beam alignment," *IEEE Trans. Wireless Commun.*, vol. 16, pp. 5689–5701, Sept. 2017.

[26] R. K. Patra and C. K. Nayak, "A comparison between different adaptive beamforming techniques," in *Proc. 2019 International Conference on Range Technology*, (Balasore, India), Feb. 2019.

[27] J. Johnston, L. Venturino, E. Grossi, M. Lops, and X. Wang, "MIMO OFDM dual-function radar-communication under error rate and beampattern constraints," *IEEE J. Sel. Areas Commun.*, vol. 40, pp. 1951–1964, June 2022.

[28] R. Zhang, L. Cheng, S. Wang, Y. Lou, Y. Gao, W. Wu, and D. W. K. Ng, "Integrated sensing and communication with massive mimo: A unified tensor approach for channel and target parameter estimation," *IEEE Trans. Wireless Commun.*, vol. 23, pp. 8571–8587, Jan. 2024.

[29] R. Zhang, X. Wu, Y. Lou, F.-G. Yan, Z. Zhou, W. Wu, and C. Yuen, "Channel training-aided target sensing for terahertz integrated sensing and massive MIMO communications," *IEEE Internet Things J.*, Aug. 2024.

[30] F. Liu, P. Zhao, and Z. Wang, "EKF-based beam tracking for mmWave MIMO systems," *IEEE Commun. Lett.*, vol. 23, pp. 2390–2393, Dec. 2019.

[31] Z. Du, F. Liu, and Z. Zhang, "Sensing-assisted beam tracking in V2I networks: Extended target case," in *Proc. IEEE Int. Conf. on Acoustics,*

Speech and Signal Process. (ICASSP), (Singapore), pp. 8727–8731, May 2022.

[32] F. Morselli, S. M. Razavi, M. Z. Win, and A. Conti, "Soft information based localization for 5G networks and beyond," *IEEE Trans. Wireless Commun.*, vol. 22, pp. 9923–9938, May 2023.

[33] Z. Feng, Z. Wei, X. Chen, H. Yang, Q. Zhang, and P. Zhang, "Joint communication, sensing, and computation enabled 6G intelligent machine system," *IEEE Netw.*, vol. 35, pp. 34–42, Jan. 2022.

[34] Y. Cui, F. Liu, X. Jing, and J. Mu, "Integrating sensing and communications for ubiquitous IoT: Applications, trends, and challenges," *IEEE Netw.*, vol. 35, pp. 158–167, Nov. 2021.

[35] O. Kanhere, S. Goyal, M. Beluri, and T. S. Rappaport, "Target localization using bistatic and multistatic radar with 5G NR waveform," in *Proc. IEEE Veh. Tech. Conf. (VTC2021)*, (online), pp. 1–7, Apr. 2021.

[36] S. H. Dokhanchi, B. S. Mysore, K. V. Mishra, and B. Ottersten, "A mmWave automotive joint radar-communications system," *IEEE Trans. Aerosp. Electron. Syst.*, vol. 55, pp. 1241–1260, June 2019.

[37] M. Chiani, A. Giorgetti, and E. Paolini, "Sensor radar for object tracking," *Proc. IEEE*, vol. 106, pp. 1022–1041, June 2018.

[38] B. K. Habtemariam, R. Tharmarasa, T. Kirubarajan, D. Grimmett, and C. Wakayama, "Multiple detection probabilistic data association filter for multistatic target tracking," in *Proc. 14th International Conference on Information Fusion*, pp. 1–6, July 2011.

[39] B. Yan, A. Giorgetti, and E. Paolini, "A track-before-detect algorithm for UWB radar sensor networks," *Signal Process.*, vol. 189, pp. 1–19, Dec. 2021.

[40] H. Godrich, A. M. Haimovich, and R. S. Blum, "Target localization accuracy gain in MIMO radar-based systems," *IEEE Trans. Inf. Theory*, vol. 56, pp. 2783–2803, June 2010.

[41] E. Matricardi, L. Pucci, E. Paolini, W. Xu, and A. Giorgetti, "Performance analysis of a multistatic joint sensing and communication system," in *Proc. IEEE Int. Symp. Pers. Indoor Mob. Radio Commun. (PIMRC)*, (Toronto, ON, Canada), Sept. 2023.

[42] X. Wang, Z. Han, J. Jin, R. Xi, Y. Wang, L. Han, L. Ma, M. Lou, X. Gui, Q. Wang, and G. Liu, "Multistatic integrated sensing and communication system based on macro–micro cooperation," *Sensors*, vol. 24, no. 8, 2024.

[43] E. Favarelli, E. Matricardi, L. Pucci, E. Paolini, W. Xu, and A. Giorgetti, "Map fusion and heterogeneous objects tracking in joint sensing and communication networks," in *Proc. European Radar Conf. (EuRAD)*, (Berlin, Germany), pp. 391–394, Sep. 2023.

[44] E. Favarelli, E. Matricardi, L. Pucci, E. Paolini, W. Xu, and A. Giorgetti, "Sensor fusion and extended multi-target tracking in joint sensing and communication networks," in *Proc. IEEE Int. Conf. on Commun. (ICC)*, (Rome, Italy), pp. 5737–5742, May 2023.

[45] E. Favarelli, E. Matricardi, L. Pucci, E. Paolini, W. Xu, and A. Giorgetti, "Multi-base station cooperative sensing with AI-aided tracking," in *arXiv*, Oct. 2023.

[46] L. Pucci, E. Paolini, and A. Giorgetti, "System-level analysis of joint sensing and communication based on 5G New Radio," *IEEE J. Sel. Areas Commun.*, vol. 40, pp. 2043–2055, July 2022.

[47] H. Asplund, D. Astely, P. von Butovitsch, T. Chapman, M. Frenne, F. Ghasemzadeh, M. Hagström, B. Hogan, G. Jöngren, J. Karlsson, *et al.*, *Advanced Antenna Systems for 5G Network Deployments: Bridging the Gap Between Theory and Practice*. Academic Press, 2020.

[48] E. Favarelli, E. Matricardi, L. Pucci, E. Paolini, W. Xu, and A. Giorgetti, "Tracking and data fusion in joint sensing and communication networks," in *Proc. IEEE Globecom Workshops*, (Rio de Janeiro, Brasil), pp. 341–346, Dec. 2022.

[49] J. A. Zhang, X. Huang, Y. J. Guo, J. Yuan, and R. W. Heath, "Multi-beam for joint communication and radar sensing using steerable analog antenna arrays," *IEEE Trans. Veh. Technol.*, vol. 68, pp. 671–685, Jan. 2019.

[50] 3GPP TR 38.901, *Study on channel model for frequencies from 0.5 to 100 GHz*, 2019. version 16.1.0.

[51] S. Mura, D. Tagliaferri, M. Mizmizi, U. Spagnolini, and A. Petropulu, "Waveform design for OFDM-based ISAC systems under resource occupancy constraint," in *Proc. IEEE Radar Conference (RadarConf24)*, (Denver, Colorado), May 2024.

[52] A. Tang, S. Li, and X. Wang, "Self-interference-resistant IEEE 802.11ad-based joint communication and automotive radar design," *IEEE J. Sel. Topics Commun.*, vol. 15, pp. 1484–1499, Nov. 2021.

[53] H. L. V. Trees, *Optimum Array Processing: Part IV of Detection, Estimation, and Modulation Theory*. John Wiley & Sons, Inc., 2002.

[54] M. A. Richards, *Fundamentals of radar signal processing*. McGraw-Hill, 2005.

[55] M. F. Keskin, V. Koivunen, and H. Wymeersch, "Limited feedforward waveform design for OFDM dual-functional radar-communications," *IEEE Trans. Signal Process.*, vol. 69, pp. 2955–2970, Apr. 2021.

[56] M. F. Keskin, H. Wymeersch, and V. Koivunen, "MIMO-OFDM joint radar-communications: Is ICI friend or foe?," *IEEE J. Sel. Topics in Signal Process.*, vol. 15, pp. 1393–1408, Nov. 2021.

[57] M. Alhassoun and G. D. Durgin, "A theoretical channel model for spatial fading in retrodirective backscatter channels," *IEEE Trans. Wireless Commun.*, vol. 18, pp. 5845–5854, Sept. 2019.

[58] S. D. Blunt, J. G. Metcalf, C. R. Biggs, and E. Perrins, "Performance characteristics and metrics for intra-pulse radar-embedded communication," *IEEE J. Sel. Areas Commun.*, vol. 29, pp. 2057–2066, Nov. 2011.

[59] M. I. Skolnik, *Radar handbook*. McGraw-Hill Education, 2008.

[60] M. Bühren and B. Yang, "Automotive radar target list simulation based on reflection center representation of objects," in *Proc. Int. Work. on Intelligent Transp. (WIT)*, (Hamburg, Germany), pp. 161–166, Mar. 2006.

[61] M. Bühren and B. Yang, "Simulation of automotive radar target lists using a novel approach of object representation," in *Proc. IEEE Intelligent Veh. Symp.*, (Meguro-Ku, Japan), pp. 314–319, June 2006.

[62] J. T. Rodriguez, G. P. Blasone, F. Colone, and P. Lombardo, "Exploiting the properties of reciprocal filter in low-complexity OFDM radar signal processing architectures," *IEEE Trans. Aerosp. Electron. Syst.*, vol. 59, pp. 6907–6922, June 2023.

[63] M. Henninger, S. Mandelli, M. Arnold, and S. Ten Brink, "A computationally efficient 2D MUSIC approach for 5G and 6G sensing networks," in *Proc. IEEE Wireless Comm. and Netw. Conf. (WCNC)*, (Austin, TX, USA), pp. 210–215, Apr. 2022.

[64] Y. Xiong, F. Liu, Y. Cui, W. Yuan, T. X. Han, and G. Caire, "On the fundamental tradeoff of integrated sensing and communications under Gaussian channels," *IEEE Trans. Inf. Theory*, vol. 69, pp. 5723–5751, Sept. 2023.

[65] M. F. Keskin, M. M. Mojahedian, C. Marcus, O. Eriksson, A. Giorgetti, J. Widmer, and H. Wymeersch, "Fundamental trade-offs in monostatic ISAC: A holistic investigation towards 6G," 2024.

[66] E. Telatar, "Capacity of multi-antenna Gaussian channels," *Europ. Trans. on Telecomm.*, vol. 10, pp. 585–595, Nov. 1999.

[67] C. Ouyang, S. Wu, and H. Yang, "Mutual information approximation," *arXiv*, June 2019.

[68] M. Ester, H.-P. Kriegel, J. Sander, and X. Xu, "A density-based algorithm for discovering clusters in large spatial databases with noise," in

Proc. Int. Conf. on Know. Disc. in Data Mining, (Portland, Oregon), pp. 226–231, Aug. 1996.

[69] D. Schuhmacher, B.-T. Vo, and B.-N. Vo, "A consistent metric for performance evaluation of multi-object filters," *IEEE Trans. Signal Process.*, vol. 56, pp. 3447–3457, Aug. 2008.

[70] M. Beard, B. T. Vo, and B.-N. Vo, "OSPA(2): Using the OSPA metric to evaluate multi-target tracking performance," in *Proc. Int. Conf. on Control, Autom. and Inf. Sci. (ICCAIS)*, (Chiang Mai, Thailand), pp. 86–91, Oct. 2017.

[71] A. S. Rahmathullah, A. F. García-Fernández, and L. Svensson, "Generalized optimal sub-pattern assignment metric," in *Proc. Int. Conf. on Inf. Fusion (FUSION)*, (Xi'an, China), July 2017.

[72] S. Jaeckel, L. Raschkowski, K. Börner, and L. Thiele, "Quadriga: A 3-D multi-cell channel model with time evolution for enabling virtual field trials," *IEEE Trans. Antennas Propag.*, vol. 62, pp. 3242–3256, June 2014.

[73] E. Favarelli, E. Matricardi, L. Pucci, W. Xu, E. Paolini, and A. Giorgetti, "Sensor fusion and resource management in mimo-ofdm joint sensing and communication," submitted for publication to the Transaction on Vehicular Technology, 2023.

[74] J. A. Zhang, M. L. Rahman, K. Wu, X. Huang, Y. J. Guo, S. Chen, and J. Yuan, "Enabling joint communication and radar sensing in mobile networks -a survey," *IEEE Commun. Surveys Tuts.*, pp. 1–41, 2021.

[75] L. Pucci, E. Matricardi, E. Paolini, W. Xu, and A. Giorgetti, "Performance analysis of joint sensing and communication based on 5G New Radio," in *IEEE Work. on Adv. in Netw. Loc. and Nav. (ANLN), Globecom 2021*, (Madrid, Spain), Dec. 2021.

[76] N. J. Willis, *Bistatic radar*. SciTech Publishing, 2 ed., 2005.

[77] B. Friedlander, "On transmit beamforming for mimo radar," *IEEE Trans. Aerosp. Electron. Syst.*, vol. 48, pp. 3376–3388, Oct. 2012.

[78] M. Braun, C. Sturm, and F. K. Jondral, "Maximum likelihood speed and distance estimation for OFDM radar," in *Proc. IEEE Radar Conf.*, (Arlington, VA, USA), pp. 256–261, May 2010.

[79] M. Wax and T. Kailath, "Detection of signals by information theoretic criteria," *IEEE Trans. Acoust., Speech, Signal Process.*, vol. 33, pp. 387–392, Apr. 1985.

[80] A. Mariani, A. Giorgetti, and M. Chiani, "Model order selection based on information theoretic criteria: Design of the penalty," *IEEE Trans. Signal Process.*, vol. 63, pp. 2779–2789, June 2015.

[81] R. O. Schmidt, "Multiple emitter location and signal parameter estimation," *IEEE Trans. Antennas Propag.*, vol. 34, pp. 276–280, Mar. 1986.

[82] R. Roy and T. Kailath, "ESPRIT-estimation of signal parameters via rotational invariance techniques," *IEEE Trans. Acoust., Speech, Signal Process.*, vol. 37, pp. 984–995, July 1989.

[83] P. Stoica and R. L. Moses, *Spectral analysis of signals*. Pearson Prentice Hall Upper Saddle River, NJ, 2005.

[84] L. Pucci, E. Matricardi, E. Paolini, W. Xu, and A. Giorgetti, "Performance analysis of a bistatic joint sensing and communication system," in *Proc. IEEE Int. Conf. Commun. Works.*, (Seoul, Korea), pp. 73–78, July 2022.

[85] R. S. Thomä *et al.*, "Characterization of multi-link propagation and bistatic target reflectivity for distributed multi-sensor isac," 2023.

[86] E. Fishler, A. Haimovich, R. Blum, L. Cimini, D. Chizhik, and R. Valenzuela, "Spatial diversity in radars—models and detection performance," *IEEE Trans. Signal Process.*, vol. 54, pp. 823–838, Mar. 2006.

[87] S. K. Dehkordi, L. Pucci, P. Jung, A. Giorgetti, E. Paolini, and G. Caire, "Multistatic parameter estimation in the near/far field for integrated sensing and communication," *IEEE Trans. Wireless Commun.*, vol. 23, pp. 17929–17944, Dec. 2024.

[88] J. T. Rodriguez, F. Colone, and P. Lombardo, "Supervised reciprocal filter for ofdm radar signal processing," *IEEE Trans. Aerosp. Electron. Syst.*, vol. 59, pp. 3871–3889, Aug. 2023.

[89] M. Golzadeh *et al.*, "Downlink sensing in 5G-advanced and 6G:SIB1-assisted SSB approach," in *Proc. IEEE 97th Vehicular Technology Conference (VTC2023-Spring)*, pp. 1–7, June 2023.

[90] B. Sobhani, E. Paolini, A. Giorgetti, M. Mazzotti, and M. Chiani, "Target tracking for UWB multistatic radar sensor networks," *IEEE Trans. Signal Process.*, vol. 8, no. 1, pp. 125–136, 2014.

[91] T. Bacchielli, L. Pucci, E. Paolini, and A. Giorgetti, "A low-complexity detector for OTFS-based sensing," *IEEE Trans. Wireless Commun.*, Mar. 2025.

[92] D. Tagliaferri, M. Manzoni, M. Mizmizi, S. Tebaldini, A. V. Monti-Guarnieri, C. M. Prati, and U. Spagnolini, "Cooperative coherent multistatic imaging and phase synchronization in networked sensing," *IEEE J. Sel. Areas Commun.*, vol. 42, pp. 2905–2921, June 2024.

[93] J. Watt, R. Borhani, and A. K. Katsaggelos, *Machine Learning Refined*. Cambridge University Press, 2016.